

AD-A064 708

PENNSYLVANIA STATE UNIV UNIVERSITY PARK APPLIED RESE--ETC F/G 20/4
SECONDARY-FLOW-RELATED VORTEX CAVITATION.(U)
JUL 78 M L BILLET

N00024-79-C-6043

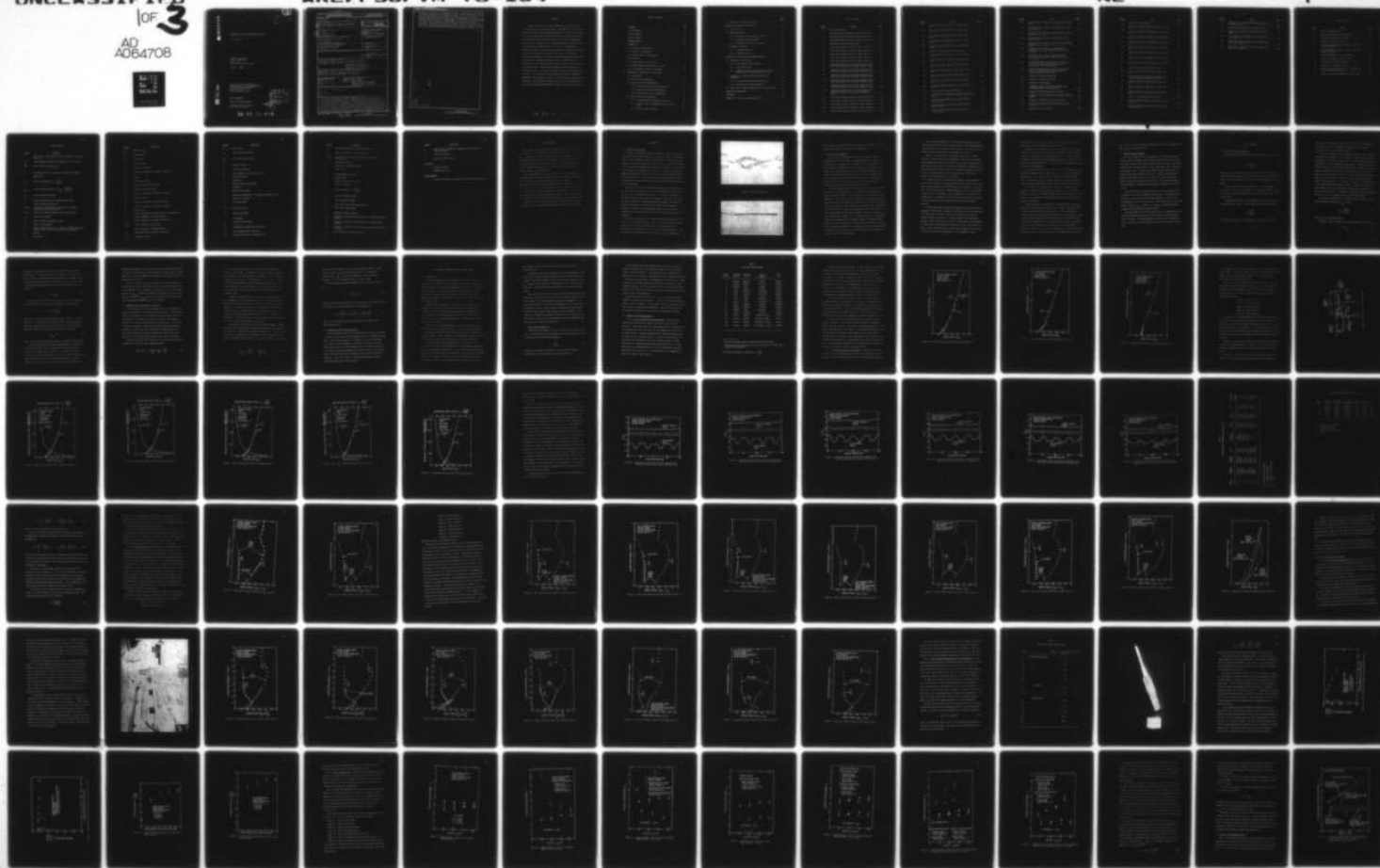
UNCLASSIFIED

OF 3

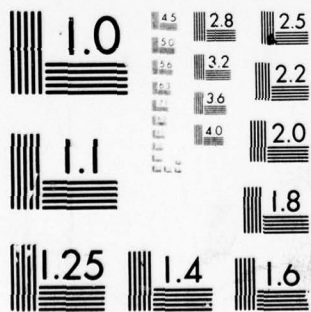
AD
A064708

ARL/PSU/TM-78-189

NL



64708



MICROCOPY RESOLUTION TEST CHART
NATIONAL BUREAU OF STANDARDS-1963-A

A064708

12

LEVEL II

SECONDARY-FLOW-RELATED VORTEX CAVITATION

M. L. Billet

Technical Memorandum
File No. TM 78-189
July 5, 1978
Contract No. N00024-79-C-6043

Copy No. 35

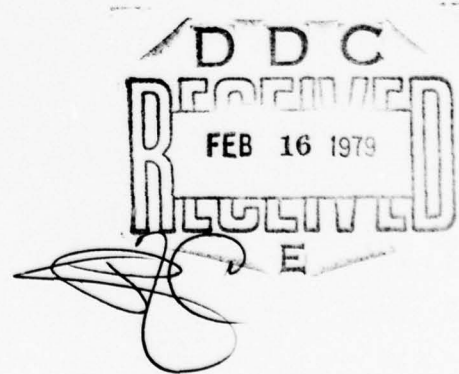
DDC FILE COPY

The Pennsylvania State University
Institute for Science and Engineering
APPLIED RESEARCH LABORATORY
Post Office Box 30
State College, PA 16801

NAVY DEPARTMENT

NAVAL SEA SYSTEMS COMMAND

Approved for Public Release
Distribution Unlimited



79 02 12 010

UNCLASSIFIED

SECURITY CLASSIFICATION OF THIS PAGE (When Data Entered)

REPORT DOCUMENTATION PAGE		READ INSTRUCTIONS BEFORE COMPLETING FORM
1. REPORT NUMBER TM 78-189	2. GOVT ACCESSION NO.	3. RECIPIENT'S CATALOG NUMBER
4. TITLE (and Subtitle) ④ <u>SECONDARY-FLOW-RELATED VORTEX CAVITATION.</u>		5. TYPE OF REPORT & PERIOD COVERED ⑨ Technical memorandum
7. AUTHOR(S) ⑩ M. L. Billet		6. PERFORMING ORG. REPORT NUMBER
9. PERFORMING ORGANIZATION NAME AND ADDRESS Applied Research Laboratory P. O. Box 30 State College, PA 16801 391 007		8. CONTRACT OR GRANT NUMBER(S) ⑮ N00024-79-C-6043
11. CONTROLLING OFFICE NAME AND ADDRESS Naval Sea Systems Command Washington, Dc 20362		10. PROGRAM ELEMENT, PROJECT, TASK AREA & WORK UNIT NUMBERS
14. MONITORING AGENCY NAME & ADDRESS (if different from Controlling Office)		12. REPORT DATE July 5, 1978
		13. NUMBER OF PAGES 260
		15. SECURITY CLASS. (of this report) UNCLASSIFIED
		15a. DECLASSIFICATION/DOWNGRADING SCHEDULE
16. DISTRIBUTION STATEMENT (of this Report) Approved for Public Release. Distribution Unlimited. Per NAVSEA - August 18, 1978 ⑪ 5 Jul 78		
17. DISTRIBUTION STATEMENT (of the abstract entered in Block 20, if different from Report) ⑭ ARL/PSU/TM-78-189		
18. SUPPLEMENTARY NOTES ⑬ 202 P. ⑯ SR02301 ⑰ SR0230101		
19. KEY WORDS (Continue on reverse side if necessary and identify by block number) vorticity secondary flow cavitation boundary layer rotor		
20. ABSTRACT (Continue on reverse side if necessary and identify by block number) A study is presented of a vortex formed near the inner wall of a rotor operating within a boundary layer. Experimental critical cavitation data and Laser Doppler Anemometer measurements obtained downstream of the rotor plane are given for many flow configurations. In addition, rotor inlet and outlet velocity profiles were measured. Experimental results show an influence of inlet velocity gradient near the inner wall on the critical cavitation number of the vortex. Secondary flow vorticity equations are developed and employed to calculate the vorticity in the blade passage near the inner wall of a rotor.		

DD FORM 1 JAN 73 1473

EDITION OF 1 NOV 65 IS OBSOLETE

UNCLASSIFIED

SECURITY CLASSIFICATION OF THIS PAGE (When Data Entered)

391 007

UNCLASSIFIED

SECURITY CLASSIFICATION OF THIS PAGE(When Data Entered)

20. In order to calculate the streamwise vorticity, an approximate method was developed to calculate the streamlines through a rotor. Cavitation data are correlated with the calculated exit passage streamwise vorticity using a simple vortex model. Results show the importance of the additional secondary vorticity on the exit streamwise vorticity near the inner wall of a rotor. The secondary vorticity induces an additional component of tangential velocity which was found to increase the flow turning near the inner wall. This increased tangential velocity profile compared favorably with the measured vortex profile outside of the vortex core region.

NTIS	Full Text	<input checked="checked" type="checkbox"/>
DDI	Full Text	<input type="checkbox"/>
UNCLASSIFIED		<input type="checkbox"/>
JUSTIFICATION		
BY		
DATE		
DIAL		
A		

UNCLASSIFIED

SECURITY CLASSIFICATION OF THIS PAGE(When Data Entered)

ABSTRACT

A study is presented of a vortex formed near the inner wall of a rotor operating within a boundary layer. Experimental critical cavitation data and Laser Doppler Anemometer measurements obtained downstream of the rotor plane are given for many flow configurations. In addition, rotor inlet and outlet velocity profiles were measured. Experimental results show an influence of inlet velocity gradient near the inner wall on the critical cavitation number of the vortex. Secondary flow vorticity equations are developed and employed to calculate the vorticity in the blade passage near the inner wall of a rotor. In order to calculate the streamwise vorticity, an approximate method was developed to calculate the streamlines through a rotor. Cavitation data are correlated with the calculated exit passage streamwise vorticity using a simple vortex model. Results show the importance of the additional secondary vorticity on the exit streamwise vorticity near the inner wall of a rotor. The secondary vorticity induces an additional component of tangential velocity which was found to increase the flow turning near the inner wall. This increased tangential velocity profile compared favorably with the measured vortex profile outside of the vortex core region.

79 02 12 010

TABLE OF CONTENTS

	<u>Page</u>
ABSTRACT	iii
LIST OF FIGURES	vi
LIST OF TABLES	xi
LIST OF SYMBOLS	xii
ACKNOWLEDGMENTS	xvii
1. INTRODUCTION	1
1.1 Origin of Investigation	1
1.2 Previous Investigations	3
1.3 General Scope of Investigation	6
2. BASIC CONCEPTS	7
2.1 Various Regimes of Cavitation	7
2.2 Minimum Pressure Coefficient of a Vortex	10
2.3 Characteristics of Vortex Cavitation	12
3. EXPERIMENTAL INVESTIGATION OF FLOW FIELD	13
3.1. Introduction	13
3.2 Basic Flow Configurations	14
3.3 Primary Flow Field Measurements	15
3.3.1 Surface Velocity Profile Measurements	15
3.3.2 Rotor Inlet Velocity Measurements	17
3.3.3 Rotor Outlet Velocity Measurements	38
3.4 Vortex Flow Field Measurements	50
3.4.1 Vortex Profile Measurements on Rotor Cap	50
3.4.2 Surface Pressure Measurements Near the Rotor Plane	60
3.4.3 Vortex Cavitation Results	68

	<u>Page</u>
3.5 Summary of Experimental Results	77
4. THEORETICAL ANALYSIS OF FLOW FIELD	84
4.1 Introduction	84
4.2 Primary Flow Field	87
4.2.1 Discussion of Calculation Procedure	87
4.2.2 Streamline Curvature Method	90
4.2.3 Estimation of Rotor Outlet Angles	92
4.3 Secondary Flow Field	97
4.3.1 Secondary Vorticity	97
4.3.2 Secondary Velocities	107
5. CALCULATION OF FLOW FIELD AND VORTEX PARAMETERS	117
5.1 Calculation of Flow Field	117
5.1.1 Flow Field for Basic Flow No. 1	117
5.1.2 Other Basic Flows	118
5.1.3 Comparisons Between Calculated and Measured Flow Fields at the End of the Rotor Cap	141
5.2 Calculation of Secondary Vorticity and Vortex Parameters	145
5.2.1 Secondary Vorticity for Basic Flow No. 1	145
5.2.2 Calculation of Vortex Parameters	155
5.3 Correlation of Vortex Parameters with Cavitation Data . .	157
6. SUMMARY AND CONCLUSIONS	170
REFERENCES	176
APPENDIX A: Analysis of Experimental Error	180

LIST OF FIGURES

<u>Number</u>	<u>Title</u>	<u>Page</u>
1	Cavitating Vortices	2
2	Meridional Velocity Profile for Basic Flow No. 11 . . .	18
3	Meridional Velocity Profile for Basic Flow No. 12 . . .	19
4	Meridional Velocity Profile for Basic Flow No. 13 . . .	20
5	Schematic of the Flow Measurements	22
6	Rotor Inlet Velocity Profile for Basic Flow No. 1 . . .	23
7	Rotor Inlet Velocity Profile for Basic Flow No. 2 . . .	24
8	Rotor Inlet Velocity Profile for Basic Flow No. 3 . . .	25
9	Rotor Inlet Velocity Profile for Basic Flow No. 4 . . .	26
10	Rotor Inlet Velocity Profile for Basic Flow No. 7 . . .	27
11	Comparison of Rotor Inlet Velocity Measured 0.062 Inch from Surface with and without Upstream Struts . .	29
12	Comparison of Rotor Inlet Velocity Measured 0.187 Inch from Surface with and without Upstream Struts . .	30
13	Comparison of Rotor Inlet Velocity Measured 0.312 Inch from Surface with and without Upstream Struts . .	31
14	Comparison of Rotor Inlet Velocity Measured 0.439 Inch from Surface with and without Upstream Struts . .	32
15	Comparison of Rotor Inlet Velocity Measured 0.647 Inch from Surface with and without Upstream Struts . .	33
16	Comparison of Rotor Inlet Velocity Measured 1.231 Inches from Surface with and without Upstream Struts	34
17	Rotor Outlet Velocity Profiles for Basic Flow No. 1 . .	39
18	Rotor Outlet Velocity Profiles for Basic Flow No. 2 . .	40
19	Rotor Outlet Velocity Profiles for Basic Flow No. 3 . .	42
20	Rotor Outlet Velocity Profiles for Basic Flow No. 4 . .	43
21	Rotor Outlet Velocity Profiles for Basic Flow No. 5 . .	44

<u>Number</u>	<u>Title</u>	<u>Page</u>
22	Rotor Outlet Velocity Profiles for Basic Flow No. 6	45
23	Rotor Outlet Velocity Profiles for Basic Flow No. 7	46
24	Rotor Outlet Velocity Profiles for Basic Flow No. 8	47
25	Rotor Outlet Velocity Profiles for Basic Flow No. 9	48
26	Comparison of Velocity Profiles for Basic Flow No. 1	49
27	Picture of LDA for 48-Inch Water Tunnel	52
28	Velocity Profiles on Rotor Cap for Basic Flow No. 1	53
29	Velocity Profiles on Rotor Cap for Basic Flow No. 2	54
30	Velocity Profiles on Rotor Cap for Basic Flow No. 3	55
31	Velocity Profiles on Rotor Cap for Basic Flow No. 4	56
32	Velocity Profiles on Rotor Cap for Basic Flow No. 5	57
33	Velocity Profiles on Rotor Cap for Basic Flow No. 6	58
34	Velocity Profiles on Rotor Cap for Basic Flow No. 9	59
35	Picture of the Rotating Scani-Valve	62
36	Static Pressure Coefficients Along Surface without Rotor	64
37	Static Pressure Coefficients Along Surface for Basic Flow No. 1	65
38	Static Pressure Coefficients on Rotor Cap for Basic Flow No. 1	66
39	Static Pressure Coefficients on Rotor Cap for Basic Flow No. 4	67

<u>Number</u>	<u>Title</u>	<u>Page</u>
40	Cavitation Data - Effect of Air Content (Basic Flow No. 4)	69
41	Cavitation Data - Effect of Cap Design (Basic Flow Nos. 4 and 10)	70
42	Cavitation Data - Effect of Flow Coefficient (Basic Flow Nos. 4, 5, and 6)	71
43	Cavitation Data - Effect of Struts (Basic Flow Nos. 1 and 4)	72
44	Cavitation Data - Effect of Struts and Screen (Basic Flow Nos. 1, 3, 4, and 7)	73
45	Cavitation Data - Effect of Screen and Flow Coefficient with Struts (Basic Flows Nos. 4, 6, 7, and 8)	74
46	Cavitation Data - Effect of Screen and Flow Coefficient without Struts (Basic Flows Nos. 1, 2, 3, and 9)	75
47	Comparison Between Static Pressure Coefficients at End of Rotor Cap with Cavitation Data for Several Basic Flows without Struts	78
48	Comparison Between Static Pressure Coefficients at End of Rotor Cap with Cavitation Data for Several Basic Flows with Struts	79
49	Schematic of Boundary Conditions	86
50	Outline of Calculation Procedure	88
51	Definition of Blade Angles	93
52	Schematic of Rotor Inner Wall Secondary Flows (Lakshminarayana and Horlock / 18 /)	100
53	Notation for Rotating Coordinate Systems	102
54	Schematic of Flow Parameters in Rotating Coordinate System	108
55	Schematic of Secondary Velocity Flow Field	111
56	Calculated Meridional Velocity Profile for Basic Flow No. 11	118
57	Design Circulation of Rotor	119

<u>Number</u>	<u>Title</u>	<u>Page</u>
58	Geometry of Blade Sections	120
59	Rotor Inlet Velocity Comparison for Basic Flow No. 1	127
60	Rotor Outlet Velocity Comparison for Basic Flow No. 1	129
61	Rotor Inlet Velocity Comparison for Basic Flow No. 2	134
62	Rotor Outlet Velocity Comparison for Basic Flow No. 2	135
63	Rotor Inlet Velocity Comparison for Basic Flow No. 3	136
64	Rotor Outlet Velocity Comparison for Basic Flow No. 3	137
65	Rotor Inlet Velocity Comparison for Basic Flow No. 4	138
66	Rotor Outlet Velocity Comparison for Basic Flow No. 4	139
67	Normalized Torque Coefficient for Rotor	140
68	Rotor Cap Velocity Comparison for Basic Flow No. 1	142
69	Rotor Cap Velocity Comparison Including Axial Velocity Variation for Basic Flow No. 1	143
70	Rotor Cap Velocity Comparison for Basic Flow No. 2	147
71	Rotor Cap Velocity Comparison for Basic Flow No. 3	148
72	Rotor Cap Velocity Comparison for Basic Flow No. 4	149
73	Outline of Secondary Flow Calculations	150
74	Relative Normal Component of Vorticity for Basic Flow No. 1	152
75	Relative Streamwise Component of Vorticity for Basic Flow No. 1	153

<u>Number</u>	<u>Title</u>	<u>Page</u>
76	Components of the Relative Streamwise Vorticity for Basic Flow No. 1	154
77	Secondary Passage Vorticity for Basic Flow No. 1 . . .	156
78	Axial Velocity Profiles for Different Reynolds Numbers	161
79	Correlation with Cavitation Data for Basic Flow Nos. 1 and 4	163
80	Correlation with Cavitation Data for Basic Flow Nos. 1, 3, 4, and 5	165
81	Correlation with Cavitation Data for Basic Flow Nos. 4, 6, 7, and 8	166

LIST OF TABLES

<u>Number</u>	<u>Title</u>	<u>Page</u>
1	Basic Flow Configurations	16
2	Two-Dimensional Boundary Layer Analysis	35
3	Axisymmetric Boundary Layer Analysis	36
4	Location of Surface Pressure Taps	61
5	Outlet Angles Using Howell's Correlation (Step 4) for Basic Flow No. 1	122
6	Outlet Angles Using NASA's Correlation (Step 5) for Basic Flow No. 1	124
7	Final Outlet Angles for Basic Flow No. 1	126
8	Final Outlet Angles for Basic Flow No. 2	130
9	Final Results for Basic Flow No. 3	131
10	Final Results for Basic Flow No. 4	133
11	Vortex Circulation and Core Size Calculated from Flow Vorticity Calculations	158
12	Comparison of Vortex Parameters at End of Cone	169

LIST OF SYMBOLS

<u>Symbol</u>	<u>Definition</u>
a	distance from leading edge to point of maximum camber along chord line
$a_{b'}$	distance between neighboring streamlines in b' direction
AVR	axial velocity ratio (V_{x_2}/V_{x_1})
b'	bi-normal direction of relative streamline ($\vec{b}' = \vec{s}' \times \vec{n}'$)
c	blade chord
C_p	pressure coefficient ($C_p = \frac{P - P_\infty}{1/2 \rho V_\infty^2}$)
$C_{p_{min}}$	minimum pressure coefficient ($C_{p_{min}} = \frac{P_{min} - P_\infty}{1/2 \rho V_\infty^2}$)
C_{p_s}	static pressure coefficient
G	distance from chord line to maximum camber point
k	cascade influence coefficient
$(K_\delta)_{sh}$	correction for blade shape with different thickness distribution than 65-series blade
$(K_\delta)_t$	correction for blade thickness other than 10 percent
L_c	vortex core parameter
m	slope of deviation angle with camber
N	number of rotor blades
n'	principle normal direction of relative streamline defined as positive toward center of curvature of the streamline
P	pressure
P_G	gas pressure

<u>Symbol</u>	<u>Definition</u>
P_{\min}	minimum pressure
P_v	vapor pressure
P_T	tap pressure
P_o	total pressure
P_{∞}	pressure of infinity
$P_{\infty l}$	pressure at infinity for limited cavitation
r	radius
r_c	vortex core radius
r_T	radius of pressure tap location
R_i	radius of rotor inner wall
R_m	radius of curvature of meridional streamline
R_R	radius of rotor
R'	distance from surface in radial direction
R^*	radius of curvature of relative streamline
s	blade spacing
s'	relative streamwise direction (relative flow direction)
u	radial component of secondary velocity
u_o	radial component of secondary velocity at $\theta = 0$
U_{TIP}	blade tip velocity ($U_{TIP} = \Omega R_R$)
v	theta component of secondary velocity
V_c	tangential velocity at vortex core radius
V_m	meridional velocity

<u>Symbol</u>	<u>Definition</u>
V_x	axial velocity
V_{x_1}	rotor inlet axial velocity
V_{x_2}	rotor outlet axial velocity
V_θ	tangential velocity
V_∞	velocity at infinity
w	axial component of secondary velocity
W	relative velocity
y	coordinate
Y	normal distance from surface
z	coordinate
α	dissolved gas content
α^*	difference between inlet flow angle and stagger angle
β	Henry's law constant
β_1	flow inlet angle
β_2^*	flow outlet angle
β_2	blade outlet angle
Γ	circulation
δ_o	camber deviation angle
δ^*	axisymmetric boundary layer thickness
$\frac{\delta^*}{\delta}$	planar boundary layer thickness
$\Delta\delta_s$	deviation angle due to secondary flows

<u>Symbol</u>	<u>Definition</u>
$\Delta\delta'$	deviation angle due to axial acceleration
$\Delta\delta^*$	deviation angle due to blade thickness
$(\delta_o^o)_{10}$	variation for 10 percent thick 65-series thickness distribution
ξ	relative vorticity
θ	axisymmetric momentum thickness
θ_c	camber angle
$\bar{\theta}$	planar momentum thickness
λ	stagger angle
ν	kinematic viscosity of fluid
ρ	density of fluid
σ	cavitation number ($\sigma = \frac{P_\infty - P_v}{1/2 \rho V_\infty^2}$)
σ_d	desinent cavitation number
σ_ℓ	limited cavitation number
τ	radius of torsion of relative streamline
χ_2	blade outlet camber angle
ψ	secondary stream of function
$\omega_{b'}$	component of absolute vorticity vector in relative bi-normal direction
$\omega_{n'}$	component of absolute vorticity vector in relative normal direction
$\omega_{s'}$	component of absolute vorticity vector in relative streamwise direction
ω_x	axial component of absolute vorticity

<u>Symbol</u>	<u>Definition</u>
$\bar{\omega}_n$	nondimensional component of absolute vorticity vector in normal direction
$\bar{\omega}$	rotational velocity
$\bar{\Omega}$	rotation vector of rotor

Subscripts

1	upstream of rotor
2	downstream of rotor

Primed Symbols

'	signify that terms are expressed in relative coordinate system
---	--

ACKNOWLEDGMENTS

With sincere appreciation, the author acknowledges the guidance and counseling of Dr. J. William Holl. The author would also like to thank Dr. B. Lakshminarayana for his assistance in the development of the secondary flow theory, Dr. Blaine R. Parkin for his support of the program, Professors R. E. Henderson and W. S. Gearhart for their many helpful suggestions, and Dr. R. E. A. Arndt for his assistance in the initial phases of the investigation.

This investigation was sponsored in part by the Naval Sea Systems Command General Hydromechanics Research Program, Subproject SR 023 01 01, and by the Naval Sea Systems Command, Code 03. The General Hydromechanics Research Program is administered by the David W. Taylor Naval Ship Research and Development Center, Contract N00017-73-C-1418.

Appreciation is offered collectively to many members of the Applied Research Laboratory who contributed in many ways. Special appreciation is offered to Mr. Mark McBride, whose streamline curvature program served as a basis for the direct problem solution and to Mr. Michael Pierzga, who did the necessary computer program modifications and calculations.

1. INTRODUCTION

1.1 Origin of Investigation

Secondary flows generate additional streamwise vorticity near the inner wall when a boundary layer flow is turned by a rotor. The apparent effect of this additional vorticity is evidenced by the high cavitation numbers of the vortex formed along the inner wall of a rotor. One example of the cavitation associated with a vortex can be found in the draft tube of a Francis turbine operating in the part load range. The cavitation number is proportional to the square of the streamwise vorticity associated with the vortex. In most cases, critical cavitation numbers typical of this vortex are often higher than those associated with any other type of rotor cavitation.

This vortex is formed in the complicated flow along the inner wall. The net vorticity in the vortex core is a combination of the primary flow vorticity and the secondary flow vorticity. The primary vorticity is related to the gradient of circulation along the blade span. This vorticity can be calculated by applying standard axisymmetric flow theories. However, the secondary vorticity is due to blade to blade pressure gradients and turning of the flow with entering vorticity and can be calculated from a set of vorticity transport equations applied along a streamline.

Experience has shown that a cavitation inception prediction of this vortex is a very difficult problem. All rotors operating with a boundary layer have a vortex along the inner wall. The appearance of this cavitating vortex varies from rotor to rotor, as shown in Figure 1. The critical cavitation number can vary as much as an order to magnitude.

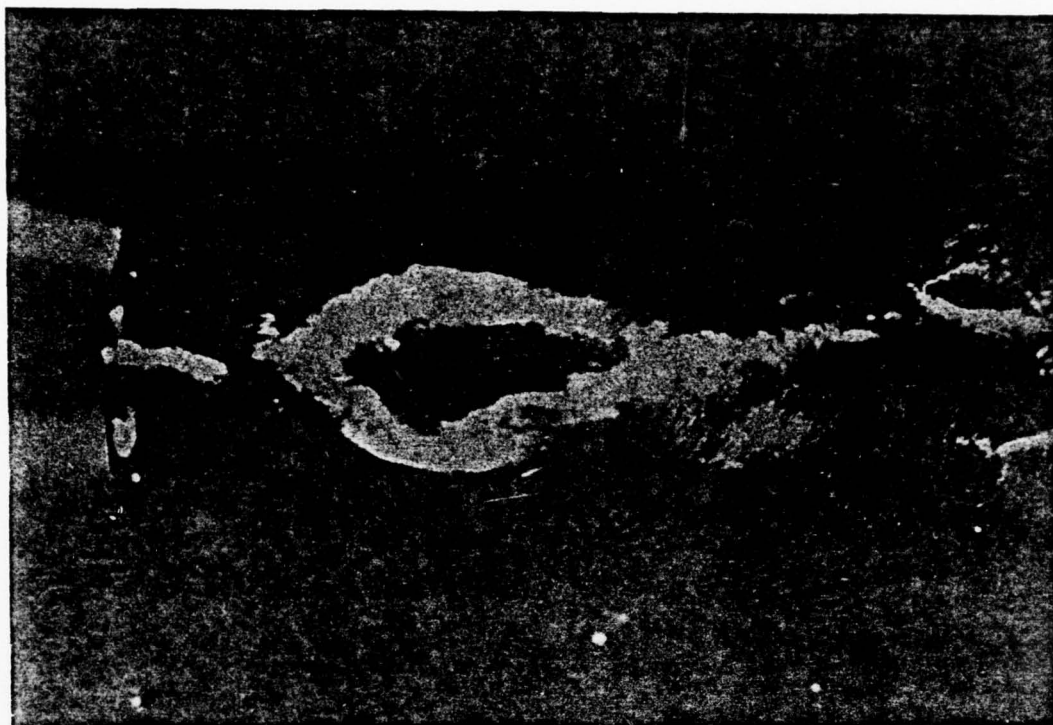
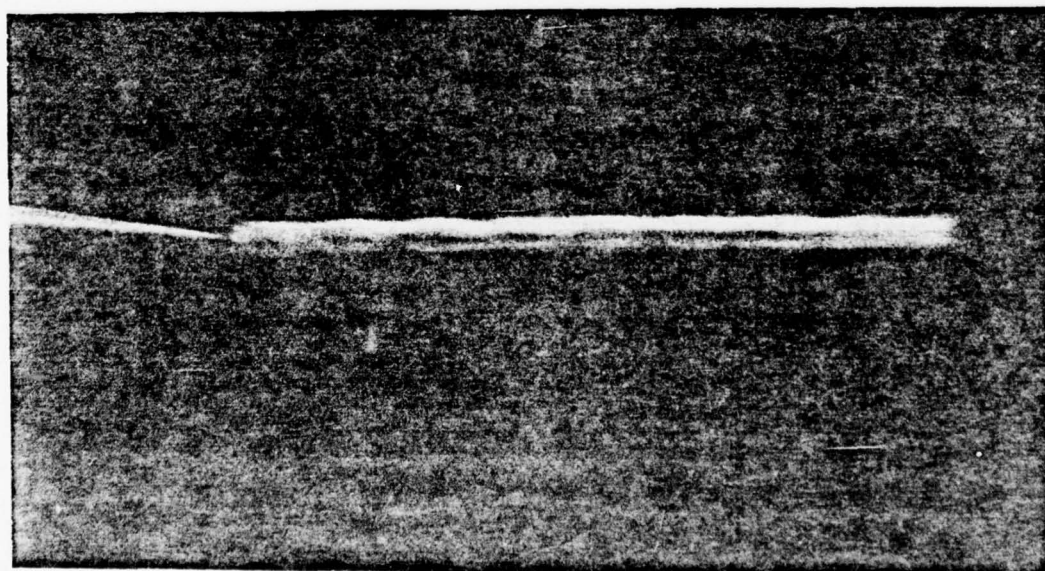


Figure 1. Cavitating Vortices



Small variations in the inlet velocity gradient to the rotor can cause a significant change in the critical cavitation number.

1.2 Previous Investigations

There has been no systematic work on the critical cavitation characteristics of the secondary flow generated vortex. Gearhart [1] investigated the secondary flow generated along the inner wall of a rotor; however, no attempt was made to correlate calculations with the structure of the vortex or with the critical cavitation number of the vortex. Nevertheless, Gearhart was one of the first to show the importance of secondary flows in a rotor operating within a boundary layer. Work has been published on the subjects of vortex cavitation, the structure of a vortex, and secondary flows in a rotor.

The most extensive previous work on the subject of vortex cavitation was conducted by McCormick [2] at the Applied Research Laboratory employing various families of finite hydrofoils which produced tip vortex cavitation. It was found that the critical cavitation number depended upon the boundary layer thickness on the pressure surface of the wing tip and that the thickness of the vortex core is apparently not determined by the induced drag of the wing. For a given wing shape, the critical cavitation number increased with Reynolds number and angle of attack and was nearly independent of aspect ratio. Although McCormick's investigation indicated the importance of the boundary layer, the minimum pressure coefficient and the structure of the vortex were not measured. Furthermore, although some exploratory investigations of the apparent nonvaporous cavitation were conducted, the observed cavitation was not related to measured values of free gas content.

More recently, Hashimoto [3] has investigated developed vortex cavitation produced by a set of stationary vanes. This investigation was devoted primarily to the study of the oscillatory nature of the cavity surface and a theory was developed to predict this behavior.

There is a large volume of literature on the subject of vortex structure. Vortices have been investigated in wakes, over the leading edge of highly-swept wings, in the wake of any wing of finite span, in pipe flows, and in nature as hurricanes and tornadoes. A major result is that these vortices are all similar to the Rankine combined vortex model having a rotational region, which is assumed to be of finite size, outside of which the motion is irrotational.

No general method for calculating the complete vortex structure exists, partly because the conditions in which they occur are varied and because the governing differential equations are nonlinear. On the other hand, all vortices possess a roughly axisymmetric core and the structure of such cores can be analyzed. Most investigators, such as Hall [4], Gartshore [5], and Bossel [6] deal with the development of a vortex core using boundary layer type equations given the initial vortex structure.

A considerable amount of vortex information has been obtained from experimental observations. Sarpkaya [7], Harvey [8], and Kirkpatrick [9] have found that under certain flow conditions the vortex can abruptly change its structure. In studying swept wings, Peckham and Atkinson [10] observed that the core of a leading edge vortex expanded at some distance downstream from the apex of the wing. Other investigators, such as McCormick [11], observed this expansion of the vortex core in the vortex of a straight wing. This phenomenon of vortex

breakdown results in an abrupt change in the vorticity distribution of the vortex and a sudden expansion of the vortex core.

Breakdown has been observed in various forms under quite different conditions. There are several factors which influence vortex breakdown. The important factors are (1) swirl angle defined as the angle between the axial velocity vector and the maximum tangential velocity vector and (2) an adverse pressure gradient. In 1972, Hall [12] published a survey article on this phenomenon.

The importance of the secondary flows in a rotor have been discussed by many investigators, such as Hawthorne [13], the staff of NASA Lewis Research Center [14], Smith [15], and Lakshminarayana and Horlock [16]. Experimental results show that the secondary flow created in the blade passage can significantly effect the outlet angle of the blade row.

A secondary flow is formed when a flow with a spanwise velocity gradient or boundary layer is turned by a blade row. It is simply the cross-flow component of the skewed boundary layer which forms in the blade passage. This resultant cross-flow contains vorticity aligned in the streamwise direction.

There are no simple techniques that accurately predict these inner wall velocity gradient effects for rotational flows. Theoretical understanding of secondary flows through a rotor is aided by approximate solutions of the fluid flow equations that govern the flow process. There are many different approaches to the derivation of secondary flow equations; however, Horlock [17], in a discussion of a paper on secondary vorticity in axial compressor blade rows, shows that the different approaches all lead to essentially the same result. A review of secondary flow theories can be found in the papers of Lakshminarayana and Horlock

[16, 18], the staff of NASA Lewis Research Center [14], Hawthorne and Novak [19], and Salvage [20].

1.3 General Scope of Problem

The vortex formed near the inner wall of a rotor operating within a boundary layer is studied to determine the major factors which influence the minimum pressure coefficient associated with the vortex. This vortex exists in the low pressure region near the inner wall of the complicated flow behind a rotor. In this region, there are many factors which can influence the minimum pressure coefficient. However, previous experimental results indicate that the vorticity that exists in the blade passage controls the behavior of the vortex. This distributed passage vorticity appears to organize the surrounding low momentum fluid into a vortex.

This investigation of vortex cavitation is both experimental and theoretical. An inviscid secondary flow analysis is developed which is employed to assess the effect of passage streamwise vorticity on the circulation and core size of the vortex. This analysis does not give the absolute value of $C_{p_{min}}$. However, a correlation is made between the passage vorticity and vortex cavitation data.

The experimental part of this investigation is presented before the theoretical development because a picture defines the vortex problem better than words. An understanding of the flow field is necessary in order to follow many of the assumptions used in the theoretical development.

2. BASIC CONCEPTS

2.1 Various Regimes of Cavitation

Cavitation flows are delineated by the cavitation number, σ , defined as

$$\sigma \equiv \frac{P_{\infty} - P_v}{1/2 \rho V_{\infty}^2}, \quad (1)$$

where P_{∞} , V_{∞} , P_v , and ρ are the pressure at infinity, the velocity at infinity, the vapor pressure, and the mass density of the liquid, respectively. The fluid properties correspond to the bulk temperature of the liquid.

The flow regime of particular concern is limited cavitation, i.e., the extent of cavitation is minimized. The problem of limited cavitation has been reviewed in recent years by Holl [21] and Holl, Arndt, and Billet [22].

The particular value of σ corresponding to limited cavitation is the limited cavitation number, σ_{ℓ} , or critical cavitation number given by

$$\sigma_{\ell} = \frac{P_{\infty} - P_v}{1/2 \rho V_{\infty}^2}. \quad (2)$$

In this investigation, σ_{ℓ} is determined by a desinence test so that

$$\sigma_{\ell} = \sigma_d, \quad (3)$$

where σ_d is the desinent cavitation number $\overline{[23]}$. The limited cavitation number can also be determined by an inception test, provided hysteresis effects are not involved $\overline{[24]}$.

There are two general types of limited cavitation, namely, vaporous and nonvaporous cavitation. To visualize the various types of limited cavitation, it is useful to imagine that one is observing the growth of a single bubble as the pressure is suddenly reduced. Vaporous cavitation occurs at pressures less than vapor pressures and is characterized by the explosive growth of a bubble due to the rapid conversion of liquid to vapor at the bubble wall. There are two types of nonvaporous cavitation, namely, pseudo and gaseous cavitation. Pseudo cavitation occurs when a bubble merely expands due to a reduction in pressure with the mass of gas in the bubble essentially remaining constant. Gaseous cavitation occurs when a bubble grows in an oversaturated liquid due to the transport of gas across the interface. In contrast to vaporous cavitation, nonvaporous cavitation can occur at pressures greater than vapor pressure.

Of particular importance in the study of limited cavitation is the minimum pressure coefficient, $C_{p_{\min}}$, given by

$$C_{p_{\min}} \equiv \frac{P_{\min} - P_{\infty}}{1/2 \rho V_{\infty}^2}, \quad (4)$$

where P_{\min} is the minimum pressure.

In general, results indicate for vaporous limited cavitation that

$$\sigma_d \leq -C_{p_{\min}}. \quad (5)$$

In principle, nonvaporous cavitation can occur below or above vapor pressure \bar{p}_{21} . However, from a practical point of view, it is the latter type which is the most interesting because of the large values of cavitation numbers which are often typical of these cases \bar{p}_{21} . Thus, for nonvaporous limited cavitation occurring at pressures above vapor pressure,

$$\sigma_{\ell} > -C_{p_{\min}} \quad (6)$$

In 1960, Holl \bar{p}_{23} employing an equilibrium theory which ignored surface tension effects predicted for nonvaporous cavitation that

$$\sigma_{\ell} = -C_p + \frac{P_G}{1/2\rho V_{\infty}^2} \quad (7)$$

where C_p is a characteristic pressure coefficient and P_G is a pressure typical of the noncondensable gas in the bubbles. Holl indicated that there was an upper limit to the gas pressure, namely, the equilibrium value given by Henry's Law which may be expressed in the form

$$P_{G_{\max}} = \alpha\beta \quad (8)$$

where α is the dissolved gas content and β is the Henry's Law constant.

Several general implications come from Equation (7). Firstly, the equation predicts that σ_{ℓ} is a monotonically decreasing function of velocity for constant values of P_G and C_p . Secondly, the equation predicts excessively large values of σ_{ℓ} at low velocities. These results suggest that if one is to avoid confusing nonvaporous for vaporous cavitation, it is advisable to conduct tests at high velocities. The

aforementioned tendency for σ_L to decrease with velocity for nonvaporous cavitation is characteristic of data reported by several authors, namely, Hammitt et al. [25], Lindgren and Johnson [26], McCormick [11], and Ripken and Killen [27].

Thus, it is very important to understand the differences between vaporous and nonvaporous cavitation in order to interpret test data. It is also apparent in view of Equations (5) and (6) that it is very important to know $C_{P_{min}}$ in order to differentiate between various flow states. However, in many flows $C_{P_{min}}$ data are not available so that other means for differentiating between flow states are needed.

2.2 Minimum Pressure Coefficient of a Vortex

It is appropriate to find a simple description of a vortex before making a calculation of its minimum pressure coefficient. Unfortunately, vortices are composed of a finite number of vortex filaments and a difficulty arises in specifying this number. The effect of streamwise filaments is to induce a swirl velocity distribution (V_θ). As a result of this swirl velocity, a radial static pressure gradient develops. Therefore, the direct method for obtaining the minimum pressure is to numerically integrate the velocity distribution from infinity to the vortex axis. The minimum pressure occurs at the center of a vortex.

The equation used in the calculation of the pressure in a vortex for axisymmetric flow is the radial momentum equation,

$$\frac{1}{\rho} \frac{\partial P}{\partial r} = \frac{V_\theta^2}{r} + V_m^2 \left(\frac{\cos \phi}{R_m} - \frac{\sin \phi}{V_m} \cdot \frac{\partial V_m}{\partial m} \right) \quad (9)$$

For this equation, the pressure is a function of the components of velocity in two planes. The component of velocity which is tangent to the streamline and is projected onto the meridional plane is called the meridional velocity (V_m). This component of total velocity is related to the axial component by the cosine of the streamline angle (ϕ). The second component of velocity is known as the tangential velocity (V_θ). It is located in the circumferential direction perpendicular to the meridional plane.

As shown in Equation (9), there are three contributing factors in the development of a pressure gradient in a vortex. The first term is directly related to the centrifugal force which a rotating fluid element experiences. The second term is due to a moving fluid element being subjected to the streamline curvature in the meridional plane. The magnitude of this term depends greatly on the radius of curvature of the streamline. The third term is due to the convective acceleration as the area of the vortex either converges or diverges.

If the Rankine combined vortex model is employed, namely, a simple rotational core combined with an irrotational outer flow, the pressure in the center can be calculated by integrating Equation (9). For this case, the vortex is axisymmetric with an infinite radius of curvature in the meridional plane and a small gradient of meridional velocity. The result is

$$C_{p_{min}} = \frac{p_c - p_\infty}{1/2 \rho V_\infty^2} = -2 \left\{ \frac{\Gamma}{2\pi r_c V_\infty} \right\}^2, \quad (10)$$

where, in the rotational core ($r \leq r_c$), the tangential velocity is given by $V_\theta = \hat{\omega} r$ and, in the irrotational region ($r > r_c$), the tangential velocity is $V_\theta = \frac{\Gamma}{2\pi r}$. In these relationships, $\hat{\omega}$ is the rotational velocity, Γ is the circulation, and r_c is the core radius.

The circulation can also be related to the vorticity in the vortex as

$$\Gamma = 2\pi \int_0^r \omega_x r \, dr \quad , \quad (11)$$

where ω_x is now the vorticity in the direction of the axis of the vortex.

The vorticity in the axial direction can be expressed as

$$\omega_x = \frac{1}{r} \left[\frac{\partial(rV_\theta)}{\partial r} - \sin^2\phi \frac{\partial V_m}{\partial \theta} - V_m^2 \frac{(\cos\phi)}{V_m} \frac{\partial \phi}{\partial \theta} \right] \quad , \quad (12)$$

where, for axisymmetric flow, the derivatives with respect to the θ -direction are zero.

2.3 Characteristics of Vortex Cavitation

Vortex cavitation is one of the least understood forms of cavitation. It is felt that this lack of understanding is due to an inadequate knowledge of the flow field and due to a confusion on types of cavitation, i.e., vaporous versus nonvaporous cavitation. The flow field can be drastically altered by vortex breakdown and, thus, influence the cavitation number describing the observed state of cavitation. Vortex flows tend to be good collectors of gas bubbles which can cause nonvaporous cavitation. This often leads to confusing nonvaporous for vaporous cavitation giving high cavitation numbers.

3. EXPERIMENTAL INVESTIGATION OF THE FLOW FIELD

3.1 Introduction

Previous experimental results indicate that small changes in the inlet velocity gradient near the inner wall of the rotor created rather large differences in the cavitation number of the vortex. In addition, only small changes in the thrust or torque of the rotor were found for most changes in inlet velocity gradient. These experimental results showing a dependence on inlet velocity gradient led to this investigation of secondary flows.

Secondary flows generated in a rotor for incompressible flow are primarily a function of the inlet velocity gradient. In order to maximize the scale of the inlet velocity gradient for measurement, a surface having an unfavorable pressure gradient in front of the rotor plane was used in the experimental program. The rotor was located near the end of this surface.

Thus, the inlet velocity gradient to the rotor was due in a large part to the boundary layer on a surface. This boundary layer thickness in the rotor plane without the rotor was the same order of magnitude as the rotor radius. Also, the boundary layer thickness near the end of this surface was the same order of magnitude as the surface curvature.

The experimental program used several flow facilities in the Garfield Thomas Water Tunnel Building of the Applied Research Laboratory at The Pennsylvania State University. In all, there were four different test series which were needed to establish the character of the flow field near the rotor plane. Three of the test series were conducted in the 48-inch water tunnel. An additional test was conducted in the 48-inch

wind tunnel. A description of these flow facilities is given in Reference [28].

To minimize any effects produced by tunnel wall interference, liners were used in the water tunnel test section and in the wind tunnel test section. The resulting inner contour in the test section was determined by a potential flow solution for an expanded surface. Therefore, the liner was a stream surface where the surface is in a flow to infinite extent.

Each test series will not be discussed individually because in most cases parts of several tests were needed to establish one data curve. An error analysis of the experimental data is given in Appendix A. The experimental results of the flow field measurements were divided into two main groups. The first group consists of measurements of the primary flow field, such as rotor inlet and outlet velocity profiles. Data obtained to establish the character of the vortex are the second group. This includes vortex velocity measurements, pressure measurements along the surface, and vortex cavitation data.

3.2 Basic Flow Configurations

There were several ways to vary the inlet velocity gradient to the rotor. The easiest one was to change the free stream velocity (V_∞) for a specified rotor flow coefficient defined as

$$\phi = \frac{V_\infty}{U_{TIP}} \quad , \quad (13)$$

where U_{TIP} is the rotor tip velocity. This gives the influence of Reynolds number on the secondary flow generated vortex.

More important than the aforementioned cases are inlet velocity gradient variations for the same Reynolds number based on free stream velocity and rotor diameter. These variations were accomplished by adding a screen to the surface upstream of the rotor, operating the rotor at different flow coefficients, and adding struts to the surface. Adding a screen to the surface increased the thickness of the boundary layer entering the rotor. The upstream struts consisted of four struts placed at the 0° , 90° , 180° , and 270° points on the surface which made the inlet velocity profile nonaxisymmetric.

Each variation in inlet velocity gradient at a constant Reynolds number was a basic flow configuration. A list of the basic flow configurations is given in Table 1. In many cases, the free stream velocity was also varied for a basic flow configuration. These thirteen basic flow configurations formed the test matrix for the experimental program.

3.3 Primary Flow Field Measurements

3.3.1 Surface Velocity Profile Measurements. Several velocity profiles were measured in the plane of the rotor without the rotor installed. In the wind tunnel at a Reynolds number of 3.0×10^5 based on rotor diameter and free stream velocity, measurements were obtained for (1) Basic Flow No. 11 (without upstream struts, without upstream screen, and without rotor), (2) Basic Flow No. 12 (without upstream struts, with upstream screen, and without rotor), and (3) Basic Flow No. 13 (with upstream struts, without upstream screen, and without rotor). In the water tunnel at a Reynolds number of 8.8×10^5 , measurements were again obtained for Basic Flow No. 11. Only Basic Flow No. 11 is amenable to theoretical boundary layer analysis.

TABLE 1
BASIC FLOW CONFIGURATIONS

Basic Flow Nos.	Upstream Struts**	Upstream Screen	Flow Coefficient ϕ ***	Rotor Cap
1	Without	Without	Design	Conical
2	Without	Without	0.9 Design	Conical
3	Without	With	Design	Conical
4	With	Without	Design	Conical
5	With	Without	1.1 Design	Conical
6	With	Without	0.9 Design	Conical
7	With	With	Design	Conical
8	With	With	0.9 Design	Conical
9	Without	With	0.9 Design	Conical
10	With	Without	Design	Truncated
11	Without	Without	No Rotor	Conical
12	Without	With	No Rotor	Conical
13	With	Without	No Rotor	Conical
14*	Without	Without	Design at Re_{ref}	Conical
15*	Without	Without	Design at $3 Re_{ref}$	Conical
16*	Without	Without	0.9 Design at Re_{ref}	Conical
17*	Without	Without	0.9 Design at $3 Re_{ref}$	Conical

*These are special cases for theoretical calculations only.

**The upstream struts consisted of four struts placed at 0° , 90° , 180° , and 270° on the surface.

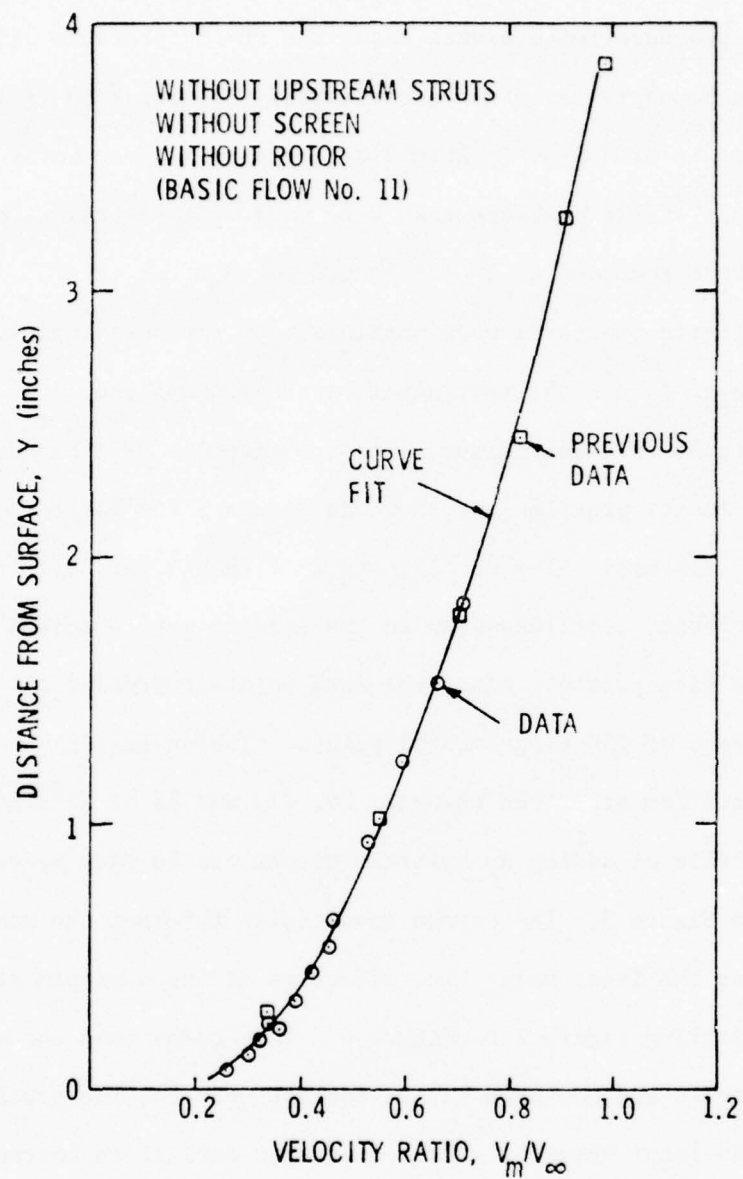
***The flow coefficient is defined as $\phi = \frac{V_\infty}{U_{TIP}}$.

For the wind tunnel measurements, the local velocity was calculated from total pressure measurements after the static pressure distribution through the boundary layer was established. The accuracy of these measurements is discussed in Appendix A. In all, three total pressure rakes and one static pressure rake were used. As the rakes were rotated, pressures were recorded at 2° increments for a total of 360° . In addition, static pressures were obtained from pressure taps located on the surface to insure the true static pressure near the inner wall. Further details of these measurements are given in Reference [29].

The velocity profiles are shown in Figure 2 for Basic Flow No. 11, in Figure 3 for Basic Flow No. 12, and in Figure 4 for Basic Flow No. 13. The mean velocity profiles shown in the figures were obtained by curve fitting the data points. Also, the data points represent the circumferential average of 180 experimental points. Tables listing the mean velocity profiles are given on pages 26, 27, and 28 of Reference [29].

The effect of adding an upstream screen can be seen by comparing Figure 2 to Figure 3. The screen essentially thickens the momentum deficit near the inner wall. The effect of adding upstream struts can be seen by comparing Figure 2 to Figure 4. This comparison shows that the upstream struts add momentum to the deficit near the inner wall and increase the local velocity. This resulting deficit is controlled by the secondary flows created at the intersection of the struts and the inner wall. A more detailed description of the circumferential velocity variation due to the struts is given in the next section.

3.3.2 Rotor Inlet Velocity Measurements. Several inlet velocity profiles were measured approximately one-half chord length in front of the rotor. These measurements were done in the 48-inch wind tunnel at a



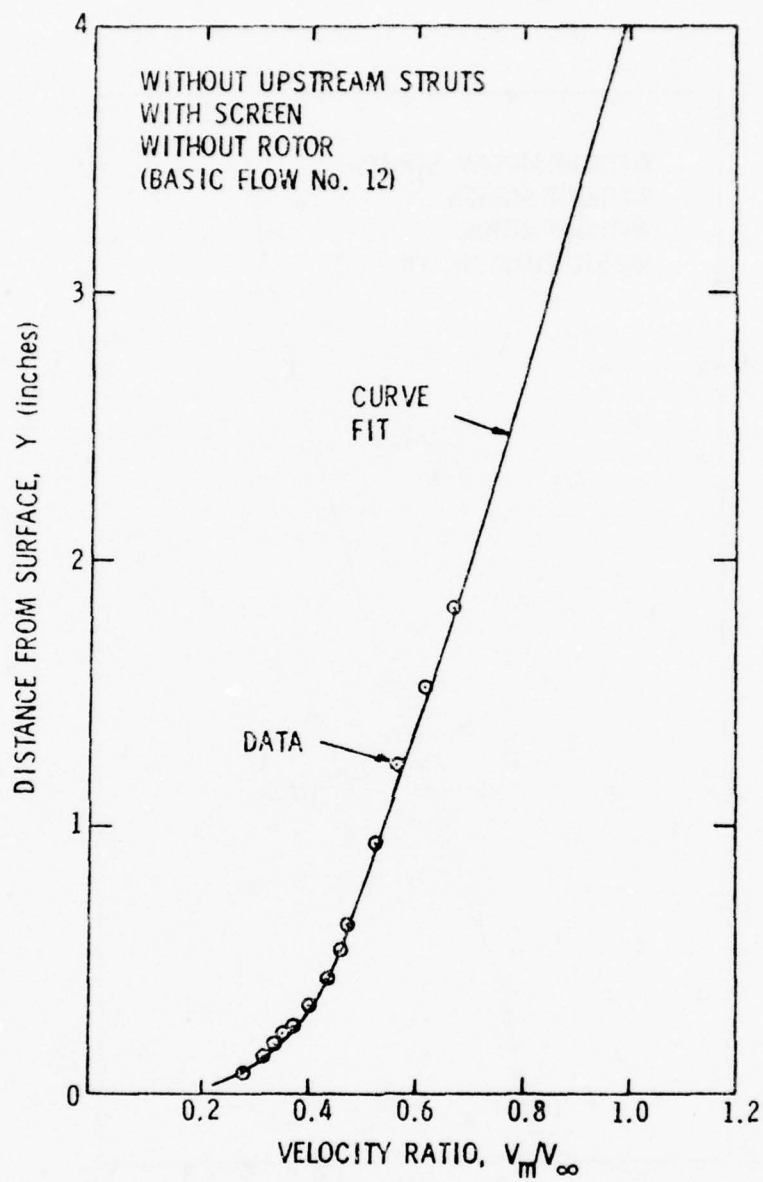


Figure 3. Meridional Velocity Profile for Basic Flow No. 12

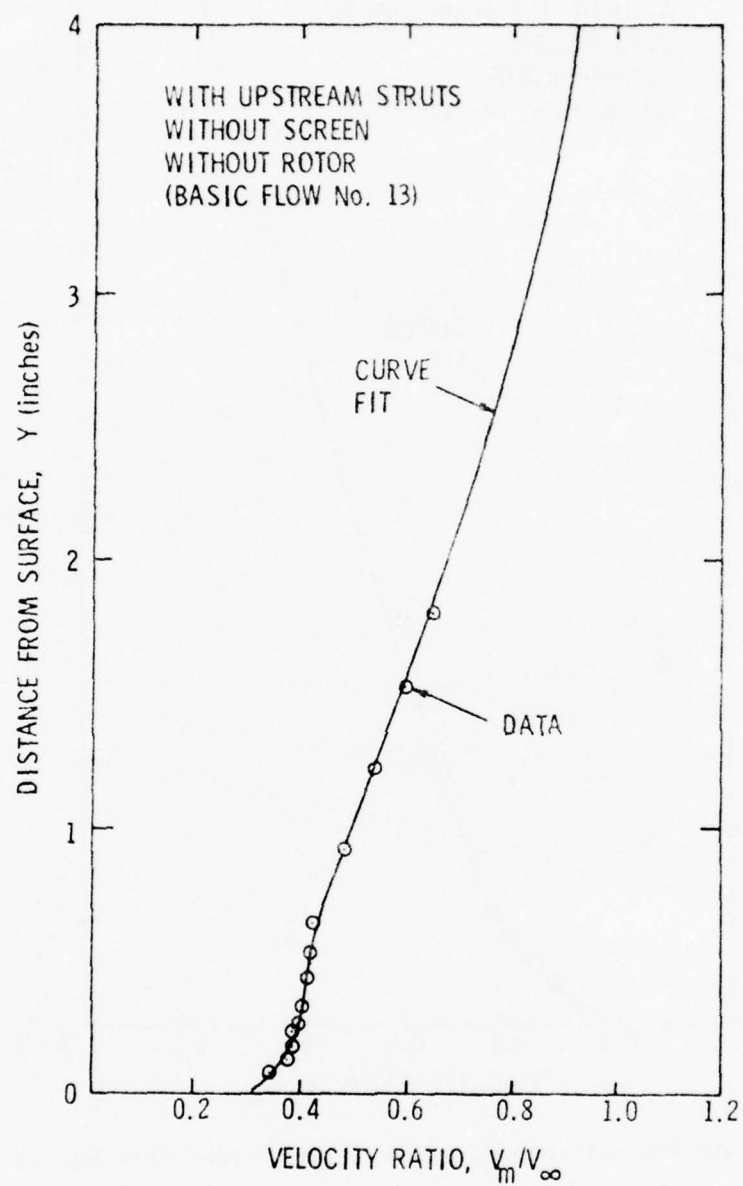


Figure 4. Meridional Velocity Profile for Basic Flow No. 13

Reynolds number of 3.0×10^5 using several pressure rakes and one static pressure rake. A schematic showing the plane of the measurements and the location of the rotor is shown in Figure 5. The accuracy of these measurements is discussed in Appendix A.

The mean incoming velocity profiles obtained by curve fitting the data points are shown in Figures 6 through 10. Also, each data point represents the circumferential average of 180 experimental points. The following is the list of flow configurations for which the inlet velocity profiles were obtained:

Figure 6 - Basic Flow No. 1

Figure 7 - Basic Flow No. 2

Figure 8 - Basic Flow No. 3

Figure 9 - Basic Flow No. 4

Figure 10 - Basic Flow No. 7

A comparison of the circumferentially averaged velocity measurements obtained with the rotor (Figure 6) and without the rotor (Figure 2) shows that the mean velocities are higher for the case with the rotor. This is particularly true near the inner wall. It is probable that the higher mean velocities found with the rotor are caused by streamline convergence. This effect is produced by the favorable pressure gradient generated by the rotor.

The effect of an upstream screen on the rotor inlet velocity profile can be seen by comparing Figure 6 to Figure 8. The screen essentially thickens the momentum deficit near the inner wall of the rotor inflow region.

The effect of upstream struts can be seen by comparing Figure 6 to Figure 7. The results are similar to those previously discussed for

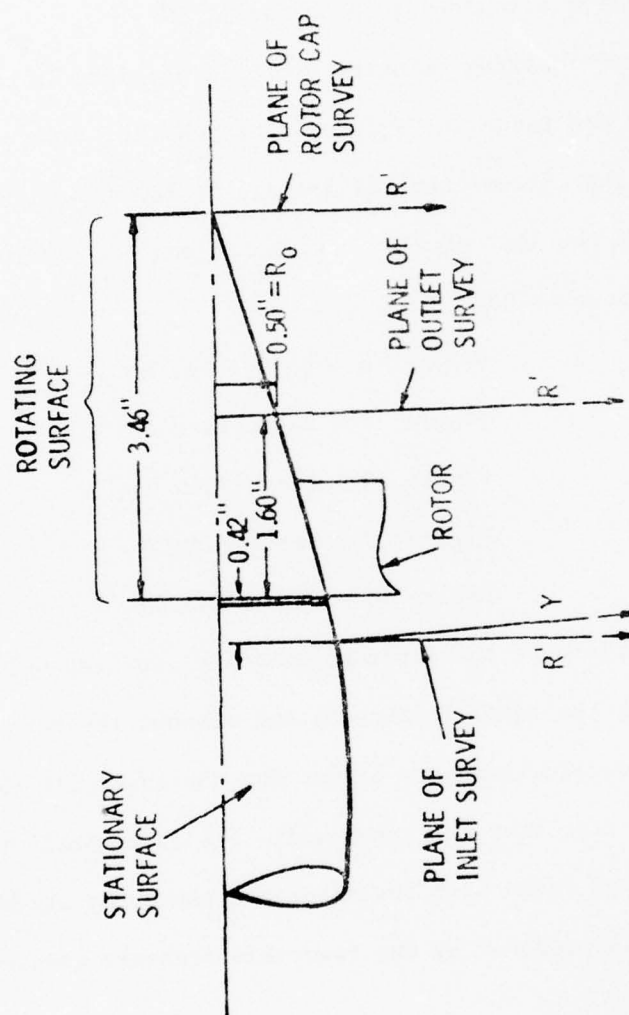


Figure 5. Schematic of the Flow Measurements

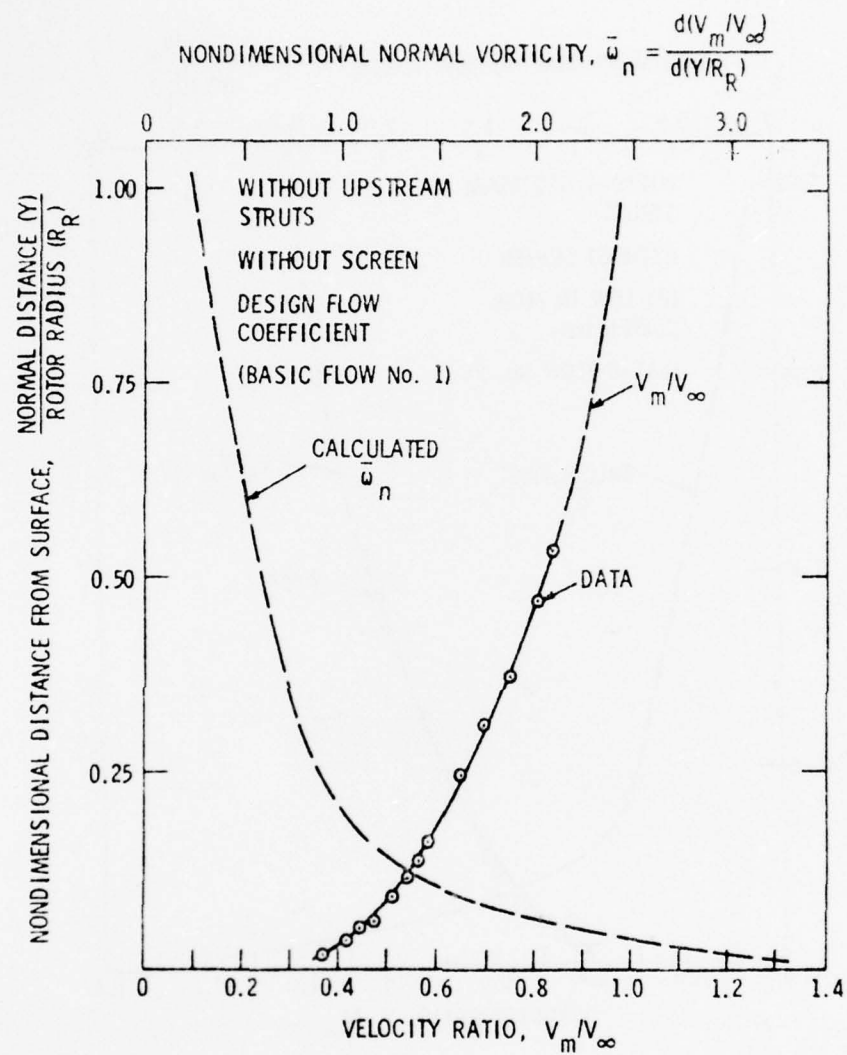


Figure 6. Rotor Inlet Velocity Profile for Basic Flow No. 1

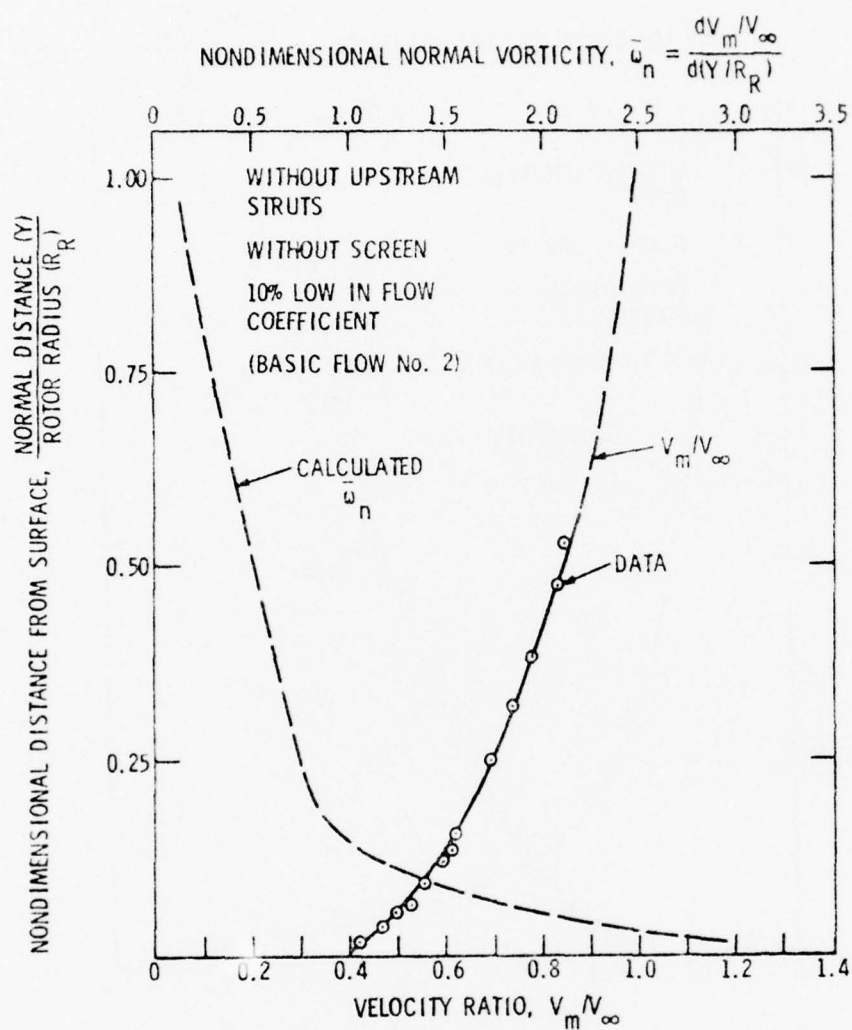


Figure 7. Rotor Inlet Velocity Profile for Basic Flow No. 2

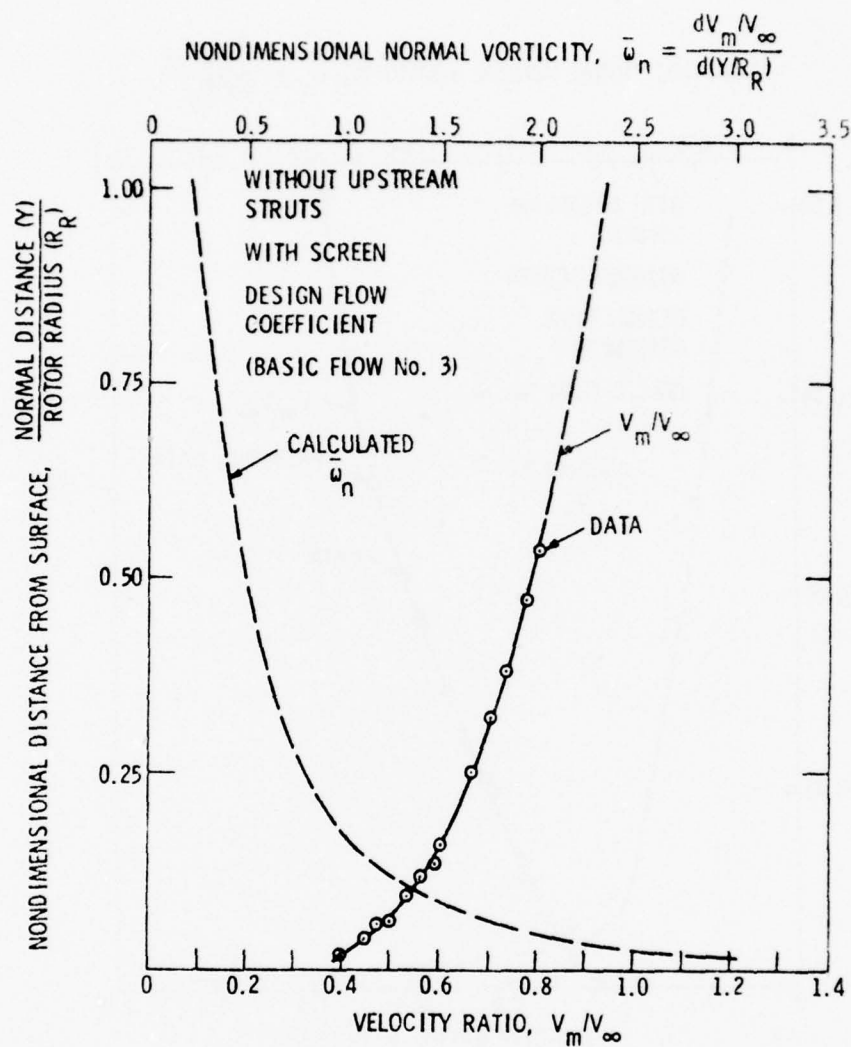


Figure 8. Rotor Inlet Velocity Profile for Basic Flow No. 3

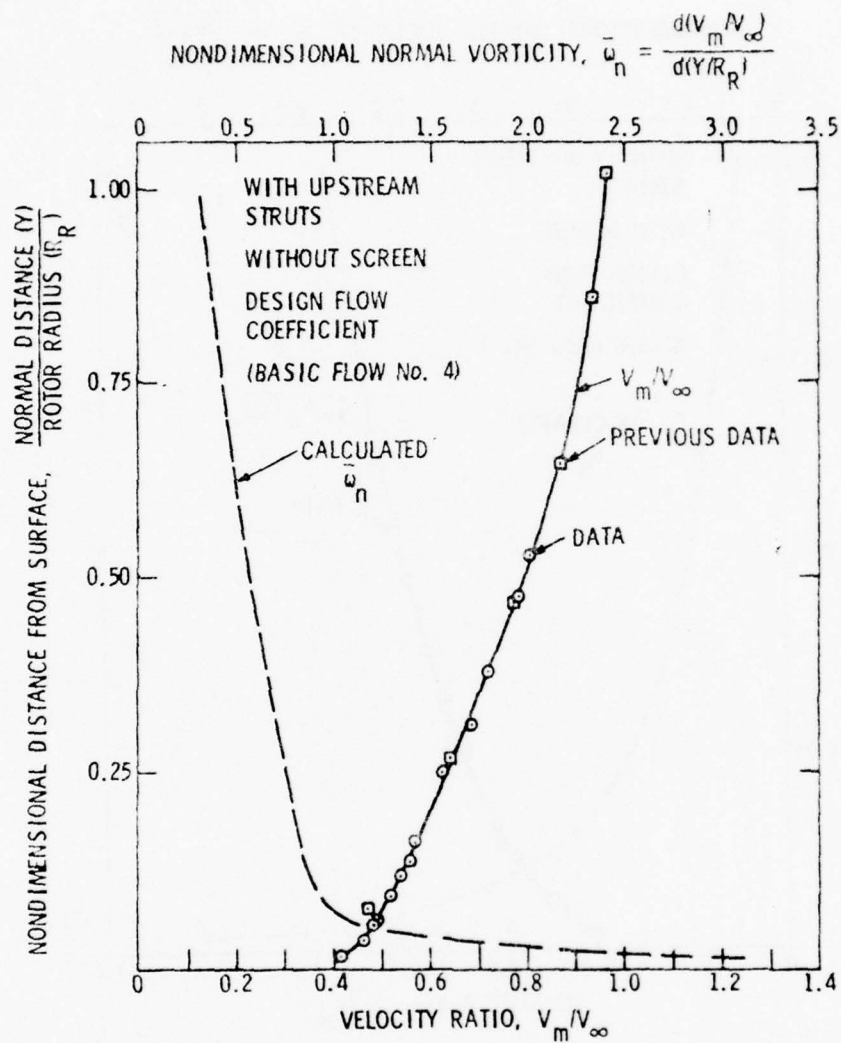


Figure 9. Rotor Inlet Velocity Profile for Basic Flow No. 4

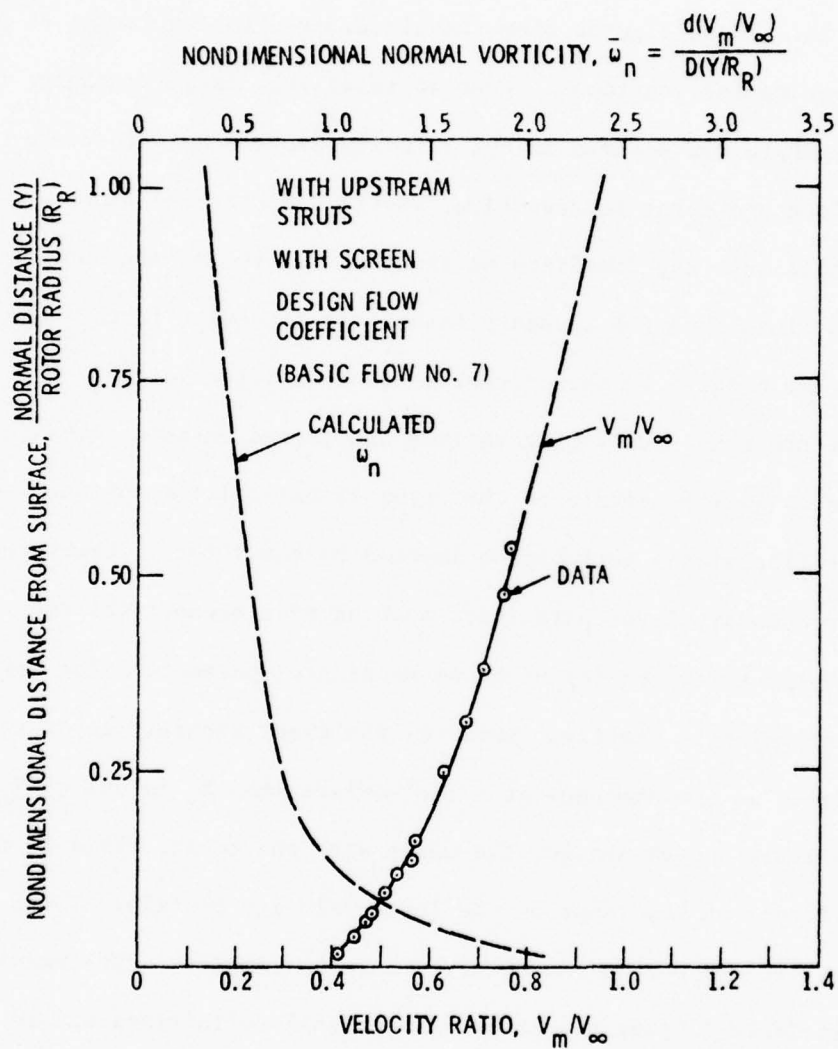


Figure 10. Rotor Inlet Velocity Profile for Basic Flow No. 7

velocity measurements obtained without the rotor and with/without upstream struts. However, the mean velocities are higher for the cases with the rotor.

More details of the effect of the struts are shown in Figures 11 through 16. These figures show the circumferential variation of velocity at various radial positions. Even at relatively large distances from the surface, sharp depressions in the velocity profile are produced. Near the surface and strut intersection, vortices are formed which entrain fresh fluid into the immediate neighborhood of the surface and displace sluggish fluid from the boundary layer. As a result, large peaks and valleys are created in the circumferential variation of velocity.

For the many flow configurations considered in this investigation, the inlet velocity profile to the rotor is basically a surface boundary layer profile with a perturbation imposed by the rotor. Therefore, standard boundary layer parameters such as displacement thickness (δ^*) and momentum thickness (θ) might be meaningful parameters for describing the inlet velocity profile. However, the exact boundary layer thickness (δ) defined as the distance from the surface when V_x is 99% of V_∞ cannot be accurately determined for the cases with the rotor. This is due to the influence of the rotor on the inlet velocity profile. Thus, the data were analyzed to obtain the boundary layer parameters. The results are shown in Table 2 using planar two-dimensional definitions and in Table 3 using axisymmetric definitions.

The two-dimensional results (Table 2) were obtained by integrating the following relationships

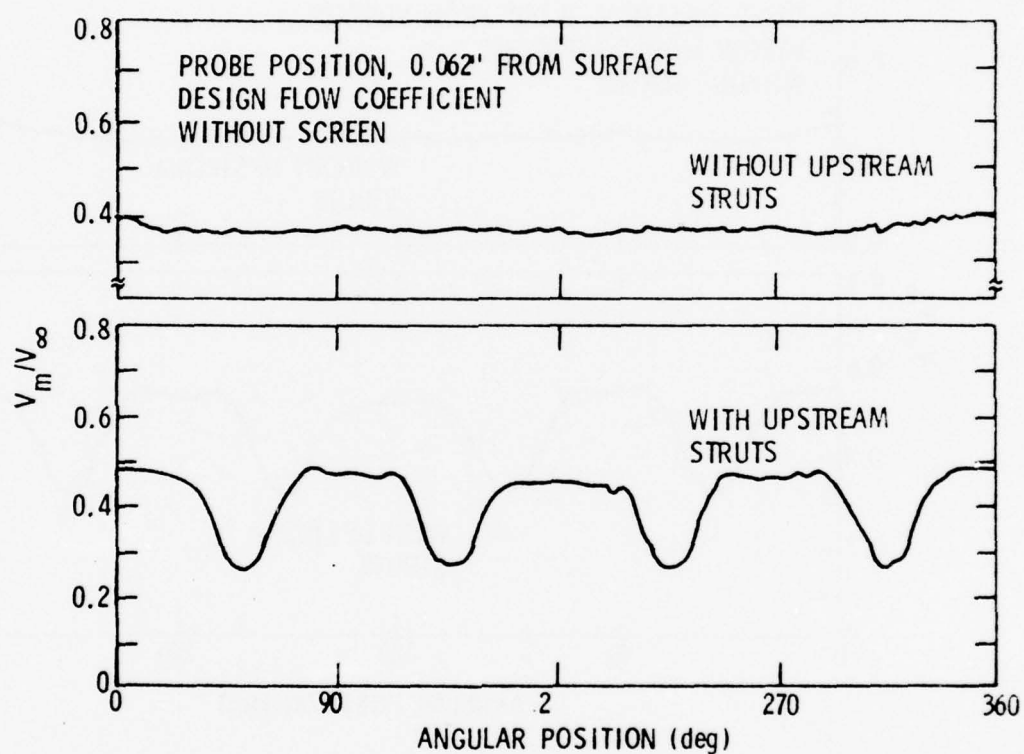


Figure 11. Comparison of Rotor Inlet Velocity Measured 0.062 Inch from Surface with and without Upstream Struts

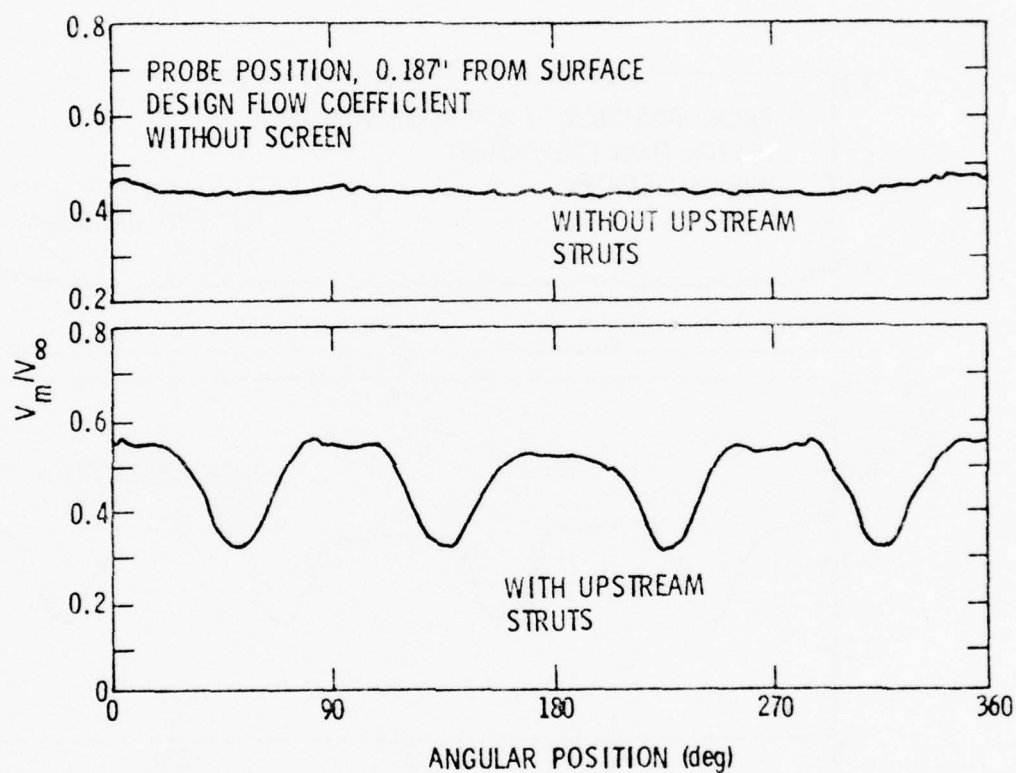


Figure 12. Comparison of Rotor Inlet Velocity Measured 0.187 Inch from Surface with and without Upstream Struts

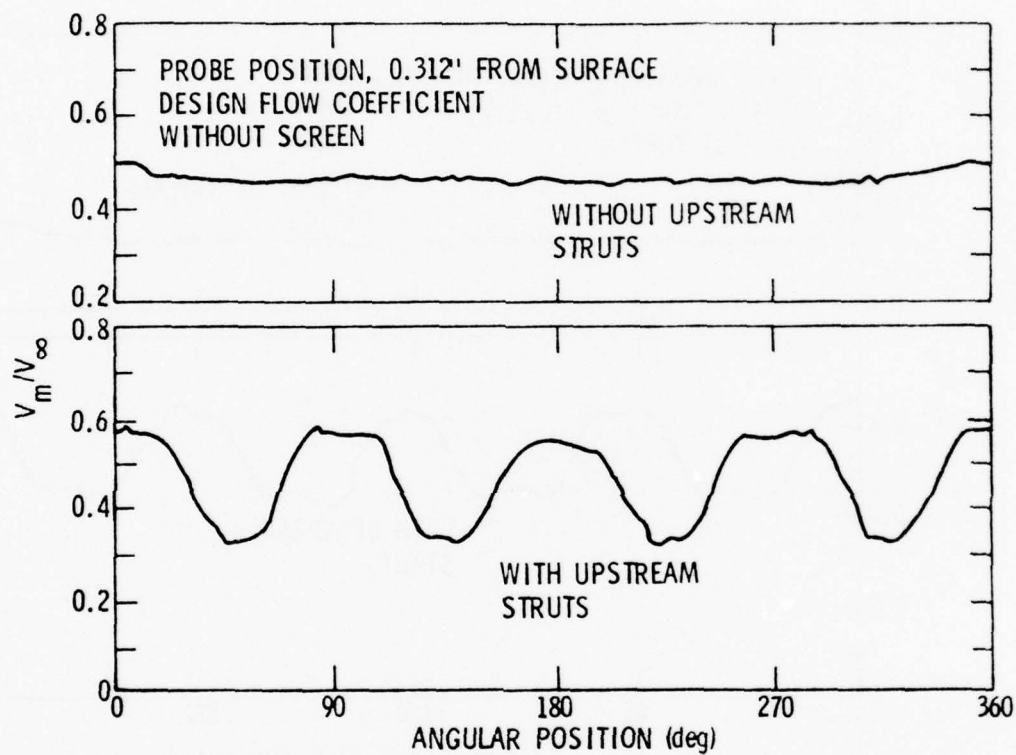


Figure 13. Comparison of Rotor Inlet Velocity Measured 0.312 Inch from Surface with and without Upstream Struts

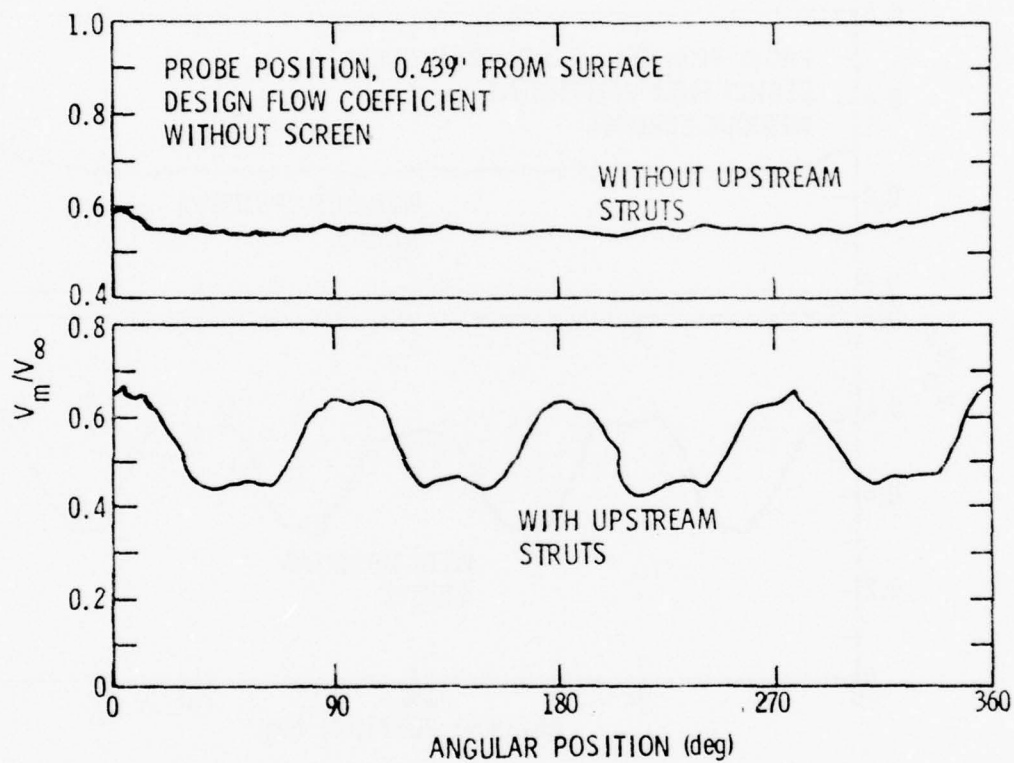


Figure 14. Comparison of Rotor Inlet Velocity Measured 0.439 Inch from Surface with and without Upstream Struts

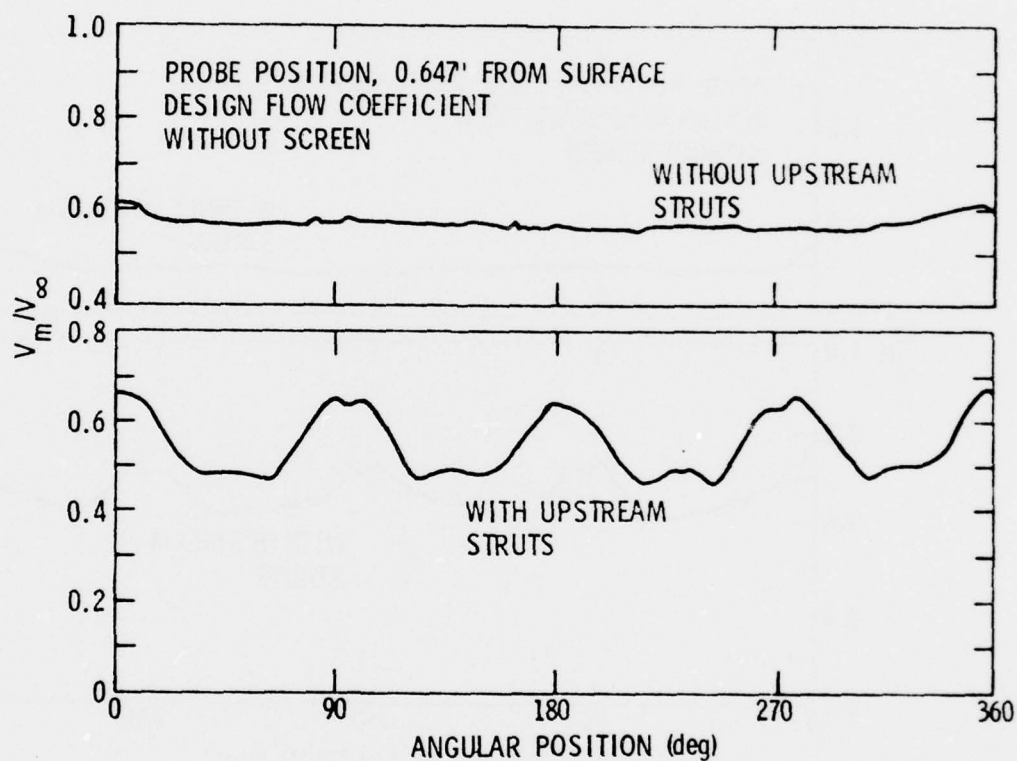


Figure 15. Comparison of Rotor Inlet Velocity Measured 0.647 Inch from Surface with and without Upstream Struts

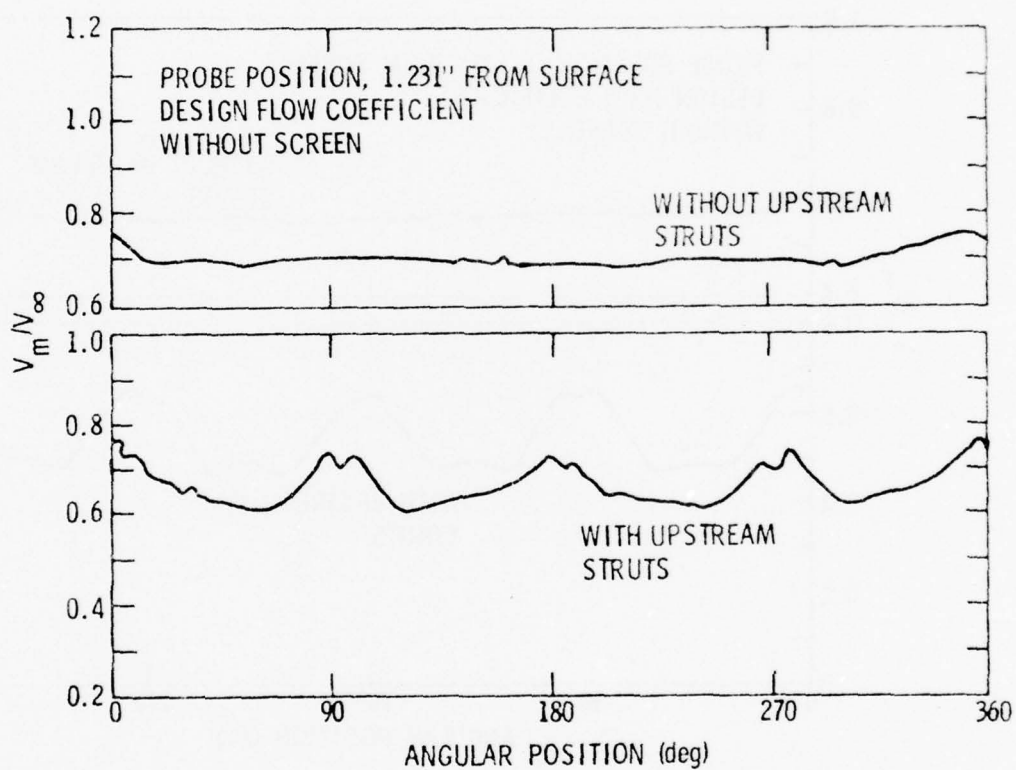


Figure 16. Comparison of Rotor Inlet Velocity Measured 1.231 Inches from Surface with and without Upstream Struts

TABLE 2
TWO-DIMENSIONAL BOUNDARY LAYER ANALYSIS

Basic Flow No.	Upstream Struts	Upstream Screen	Rotor	Flow Coefficient	$\frac{\delta^*}{\delta}$ Inches	$\bar{\theta}$ Inches	\bar{H}	Estimated $\frac{\delta}{\bar{\theta}}$ Inches
1	Without	Without	With	Design	0.830	0.539	1.54	----
2	Without	Without	With	0.9 Design	0.723	0.495	1.46	----
3	Without	With	With	Design	0.917	0.621	1.48	----
4	With	Without	With	Design	0.880	0.580	1.52	----
7	With	With	With	Design	0.972	0.645	1.51	----
11	Without	Without	Without	-----	1.148	0.645	1.78	4.09
12	Without	With	Without	-----	1.259	0.703	1.79	4.44
13	With	Without	Without	-----	-----	-----	----	----

$\frac{\delta^*}{\delta}$ - displacement thickness

$\bar{\theta}$ - momentum thickness

$\bar{\delta}$ - boundary layer thickness

$\bar{H} = \frac{\delta^*}{\bar{\theta}}$

TABLE 3
 AXISYMMETRIC BOUNDARY LAYER ANALYSIS

Basic Flow No.	Upstream Struts	Upstream Screen	Flow Coefficient	δ^* Inches	θ Inches	H
1	Without	Without	Design	0.644	1.179	1.39
2	Without	Without	0.9 Design	1.414	1.057	1.34
3	Without	With	Design	2.003	1.495	1.34
4	With	Without	Design	1.825	1.328	1.37
7	With	With	Design	2.140	1.574	1.36

δ^* - displacement thickness

θ - momentum thickness

δ - boundary layer thickness

H - $= \delta^* / \theta$

$$\overline{\delta^*} = \int_0^{\infty} \left(1 - \frac{V_m}{V_{\infty}}\right) dY \quad , \quad \overline{\theta} = \int_0^{\infty} \frac{V_m}{V_{\infty}} \left(1 - \frac{V_m}{V_{\infty}}\right) dY \quad , \quad (14)$$

where Y is the normal distance from the inner wall.

On the other hand, the incoming velocity gradient is axisymmetric so the appropriate axisymmetric definitions for displacement and momentum thickness are

$$\delta^* = \int_0^{\infty} \left(1 - \frac{V_m}{V_{\infty}}\right) \frac{r}{R_i} dY \quad , \quad \theta = \int_0^{\infty} \frac{V_m}{V_{\infty}} \left(1 - \frac{V_m}{V_{\infty}}\right) \frac{r}{R_i} dY \quad . \quad (15)$$

Patel [30] has shown that there is a relationship between planar definitions and the axisymmetric definitions so that the calculation of only one set of parameters is necessary. The calculations were done using the two-dimensional relationships.

The results of using boundary layer definitions parallel the conclusions from the figures, i.e., (1) the screen increases the momentum thickness, (2) the average effect of the upstream struts increases the momentum thickness, and (3) operating the rotor at less than design flow coefficient decreases the momentum thickness. In all configurations, the rotor operated within the estimated inlet boundary layer.

The slope of the inlet velocity profile to the rotor determines the amount of vorticity entering the rotor for the axisymmetric case. The nondimensional normal vorticity is defined as

$$\overline{\omega}_n = \frac{d(V_m/V_{\infty})}{d(Y/R_i)} \quad , \quad (16)$$

where V_m/V_∞ is a nondimensional meridional velocity profile, Y is the normal distance from the inner wall, and R_R is the radius of the rotor. The radius of the rotor was chosen as the normalizing parameter because of the uncertainty of the boundary layer thickness.

The normal vorticity data obtained from the velocity profiles are shown in Figures 6 through 10 and are listed in Tables 4 through 8 in Reference [29]. The important conclusion is that for the average inlet profile to the rotor the upstream struts reduce the amount of normal vorticity entering the rotor as compared to the no strut cases.

3.3.3 Rotor Outlet Velocity Measurements. The velocity profiles behind the rotor were measured for several rotor operating flow coefficients and several upstream surface configurations. The location of these measurements was approximately one-half chord length downstream of the rotor exit plane as shown in Figure 5. The results were obtained at a Reynolds number of 8.8×10^5 based on rotor diameter in the ARL 48-inch diameter water tunnel. Most of the velocity component data were obtained by using a 5-hole prism probe (see Reference [31]); however, a Laser Doppler Anemometer was used to verify some of the rotor outlet 5-hole probe measurements. The calibration of the 5-hole prism probe used in the measurements and a more detailed description of the experimental program is given in Reference [32]. In addition, the accuracy of these measurements is discussed in Appendix A.

The mean velocity profiles are shown in Figures 17 through 25 and are listed in Tables 2 through 10 in Reference [32]. The following is the list of flow configurations for which profiles were obtained:

Figure 17 - Basic Flow No. 1

Figure 18 - Basic Flow No. 2

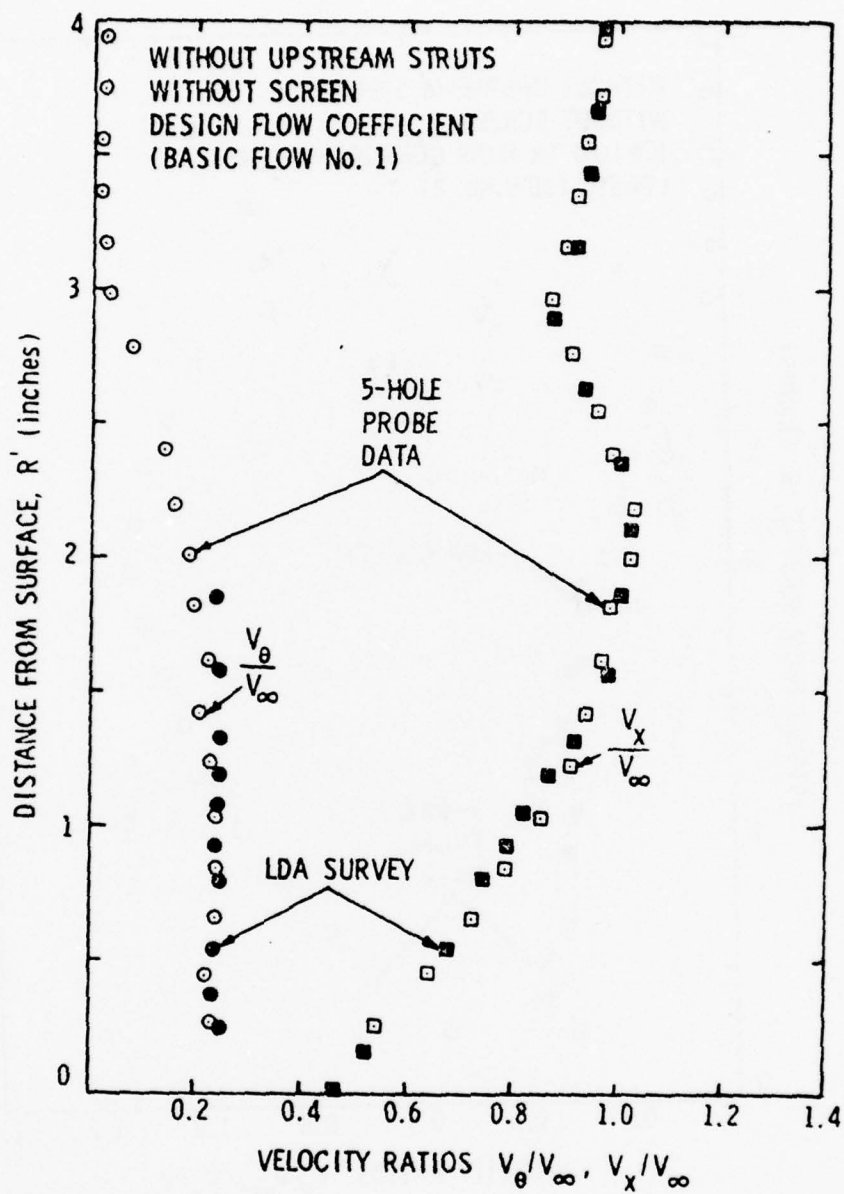


Figure 17. Rotor Outlet Velocity Profiles for Basic Flow No. 1

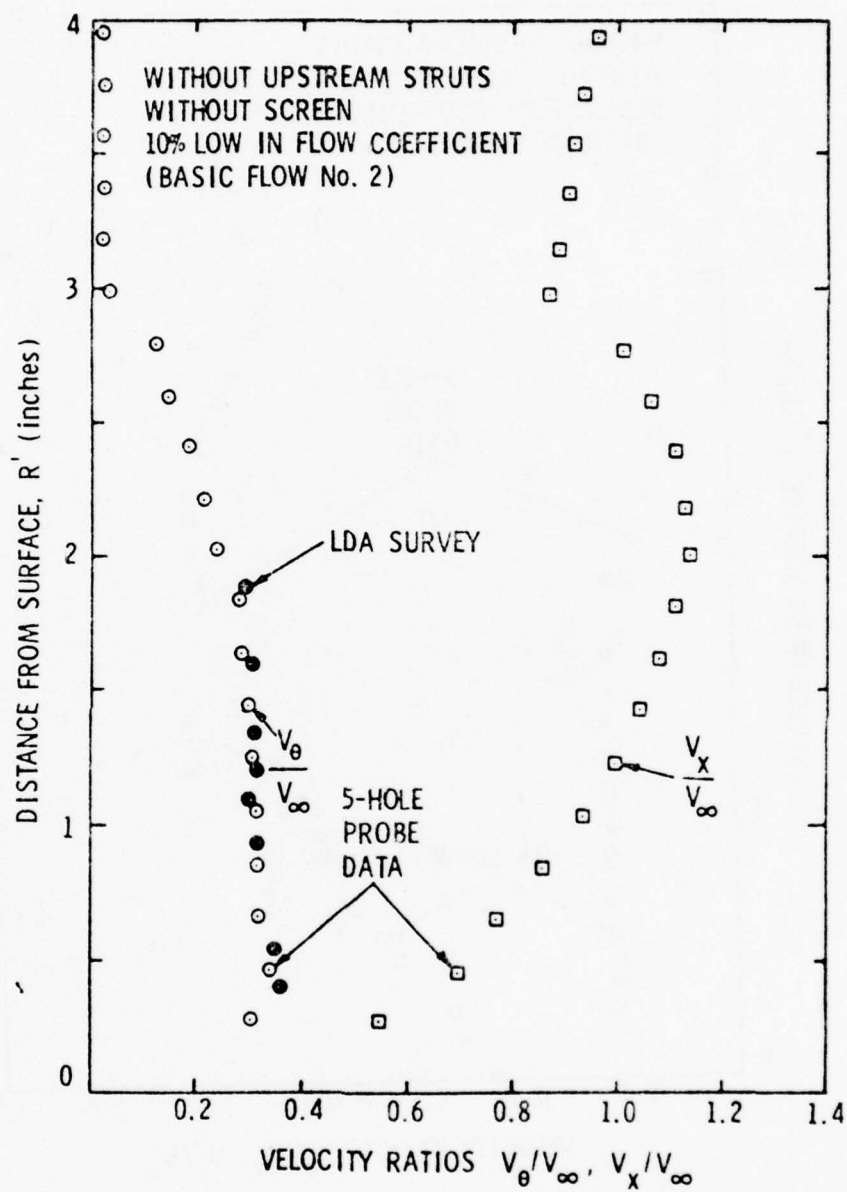


Figure 18. Rotor Outlet Velocity Profiles for Basic Flow No. 2

Figure 19 - Basic Flow No. 3

Figure 20 - Basic Flow No. 4

Figure 21 - Basic Flow No. 5

Figure 22 - Basic Flow No. 6

Figure 23 - Basic Flow No. 7

Figure 24 - Basic Flow No. 8

Figure 25 - Basic Flow No. 9

The Basic Flow Nos. are defined in Table 1.

These figures show both data obtained using a 5-hole prism probe and a LDA. The LDA was used primarily to determine how close measurements of the tangential velocity (V_θ) could be made to the rotating surface before measuring the effect of rotation on the flow. Measurements were made without the rotor but with the rotating cap. The tangential velocity ratio (V_θ/V_∞) was found to increase dramatically to a value of 0.61 for design flow coefficient within a distance of 0.20 inch from the surface. Measurements of the tangential velocity profile with the rotor were not made within a distance of 0.20 inch from the surface. The tangential velocity profile near the inner wall is a result of the secondary flows and rotor loading. In all cases, the normalized axial velocity ratio (V_x/V_∞) has a parabolic profile downstream of the rotor as a result of the loading of the rotor. This outlet axial profile is compared to the profile that would exist without the rotor and the inlet velocity profile to the rotor in Figure 26 for Basic Flow No. 1. In this figure, the velocity profile without the rotor and the inlet velocity profile were corrected from the meridional velocity to the axial velocity. The change in velocity was small because the streamline angles were less than 8 degrees.

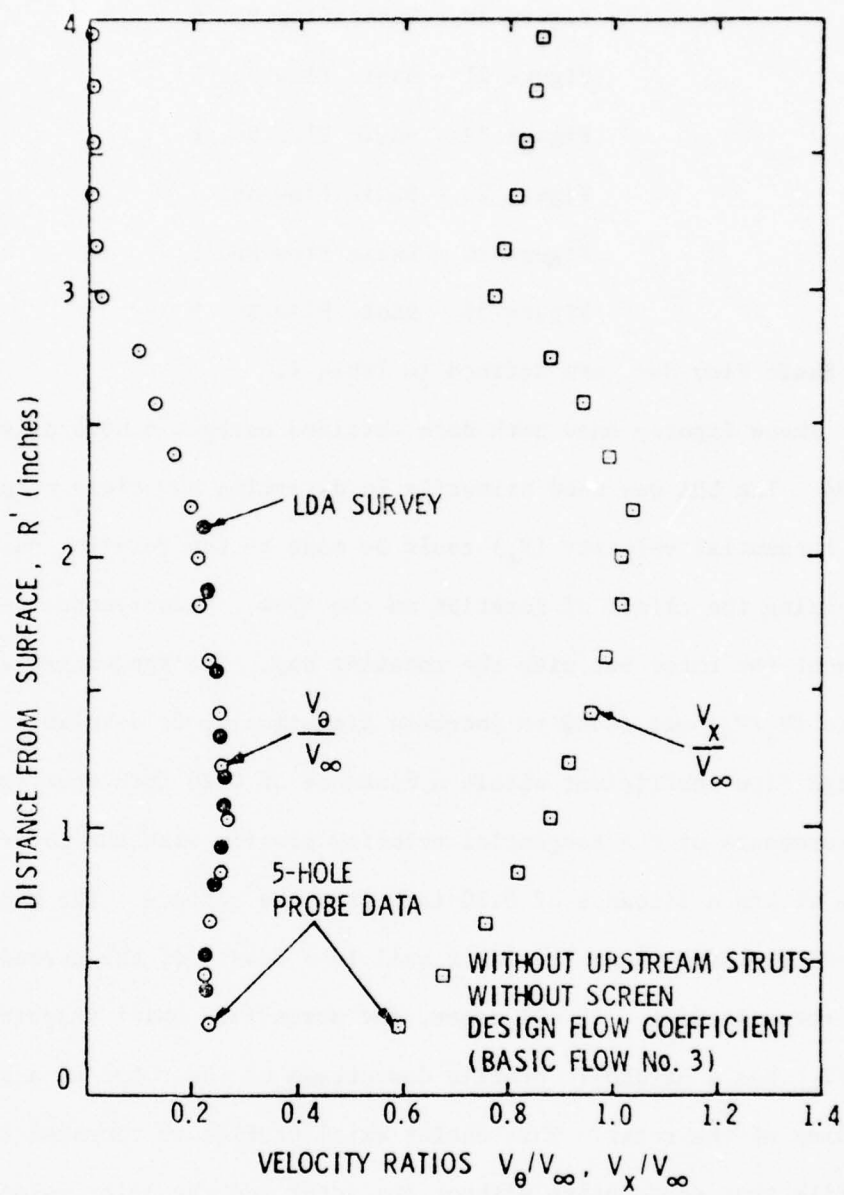


Figure 19. Rotor Outlet Velocity Profiles for Basic Flow No. 3

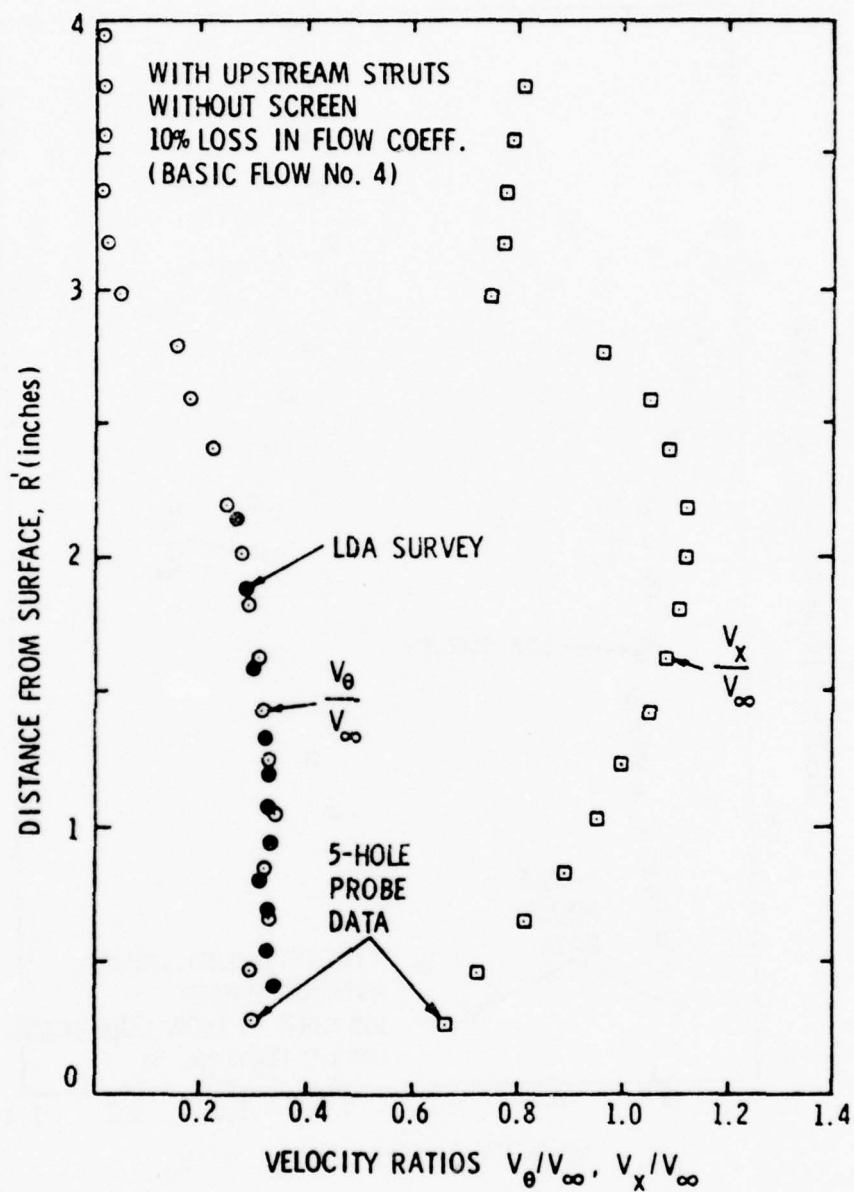


Figure 20. Rotor Outlet Velocity Profiles for Basic Flow No. 4

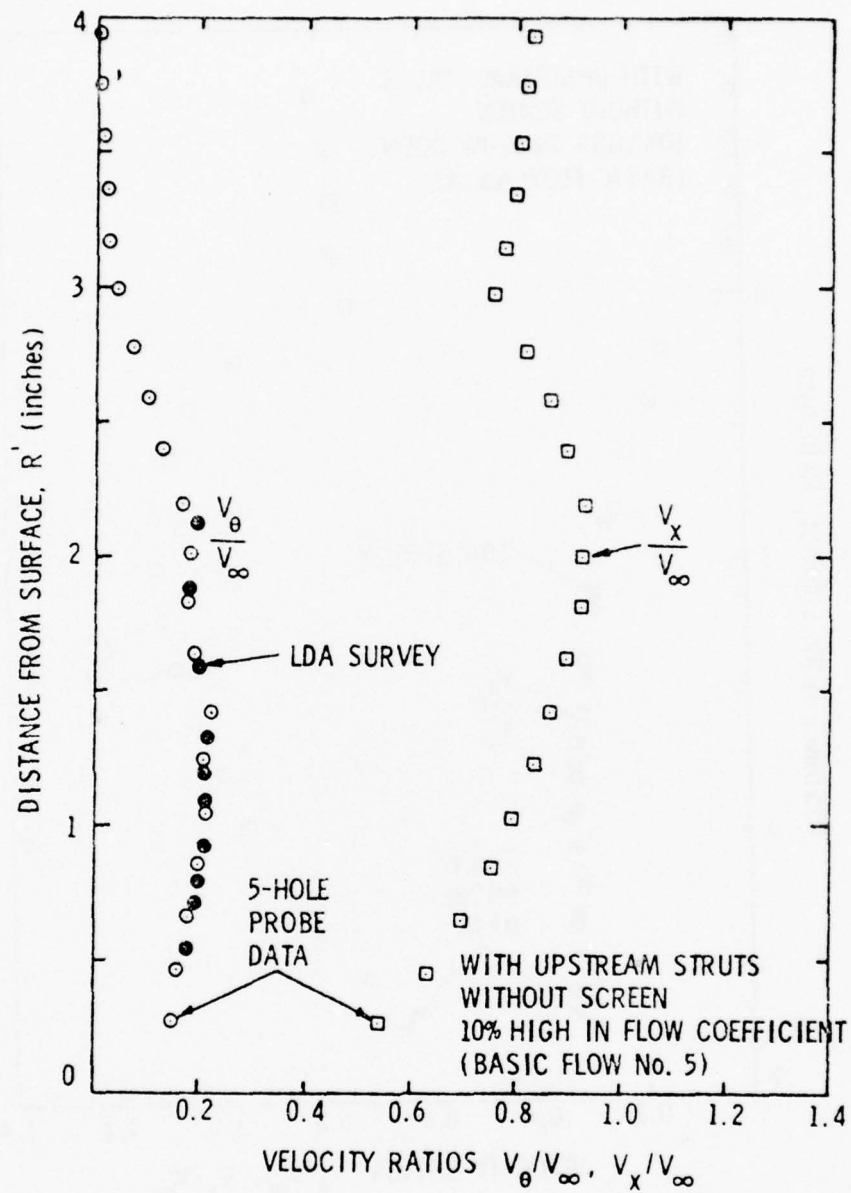


Figure 21. Rotor Outlet Velocity Profiles for Basic Flow No. 5

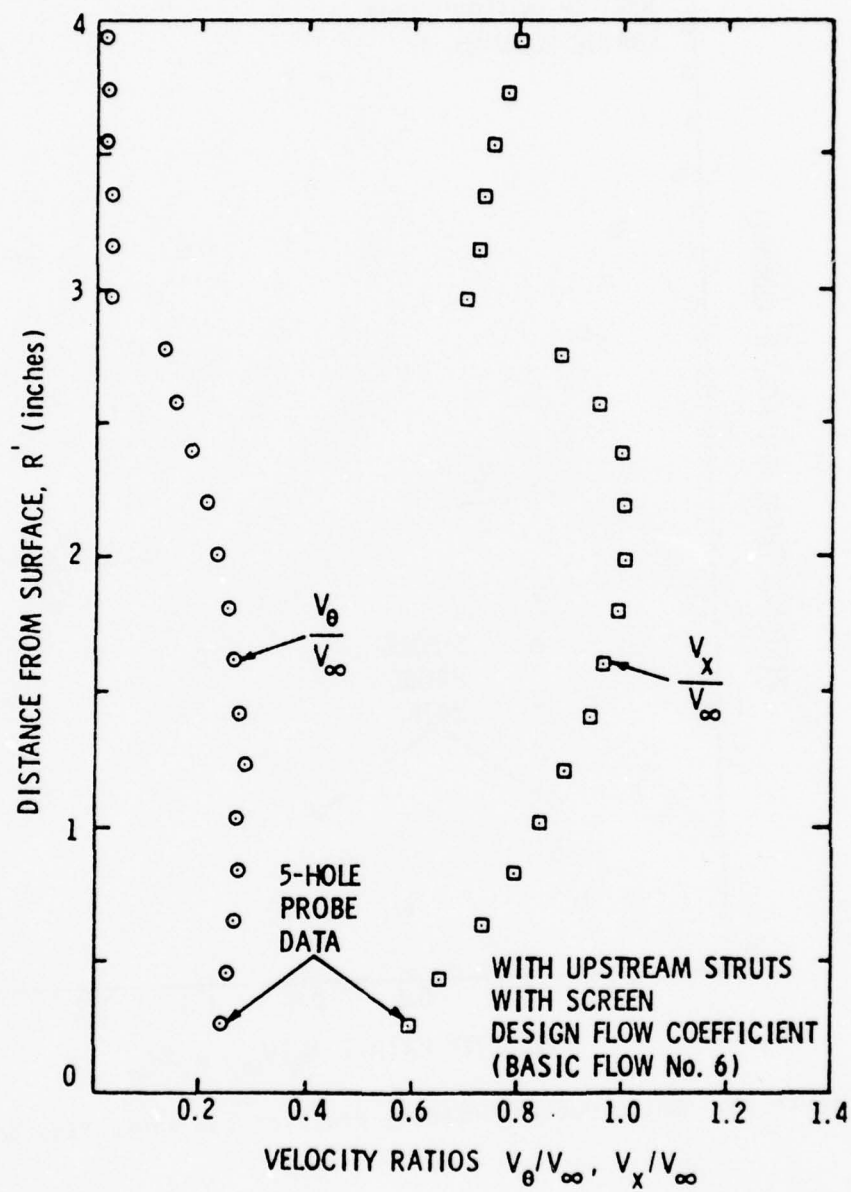


Figure 22. Rotor Outlet Velocity Profiles for Basic Flow No. 6

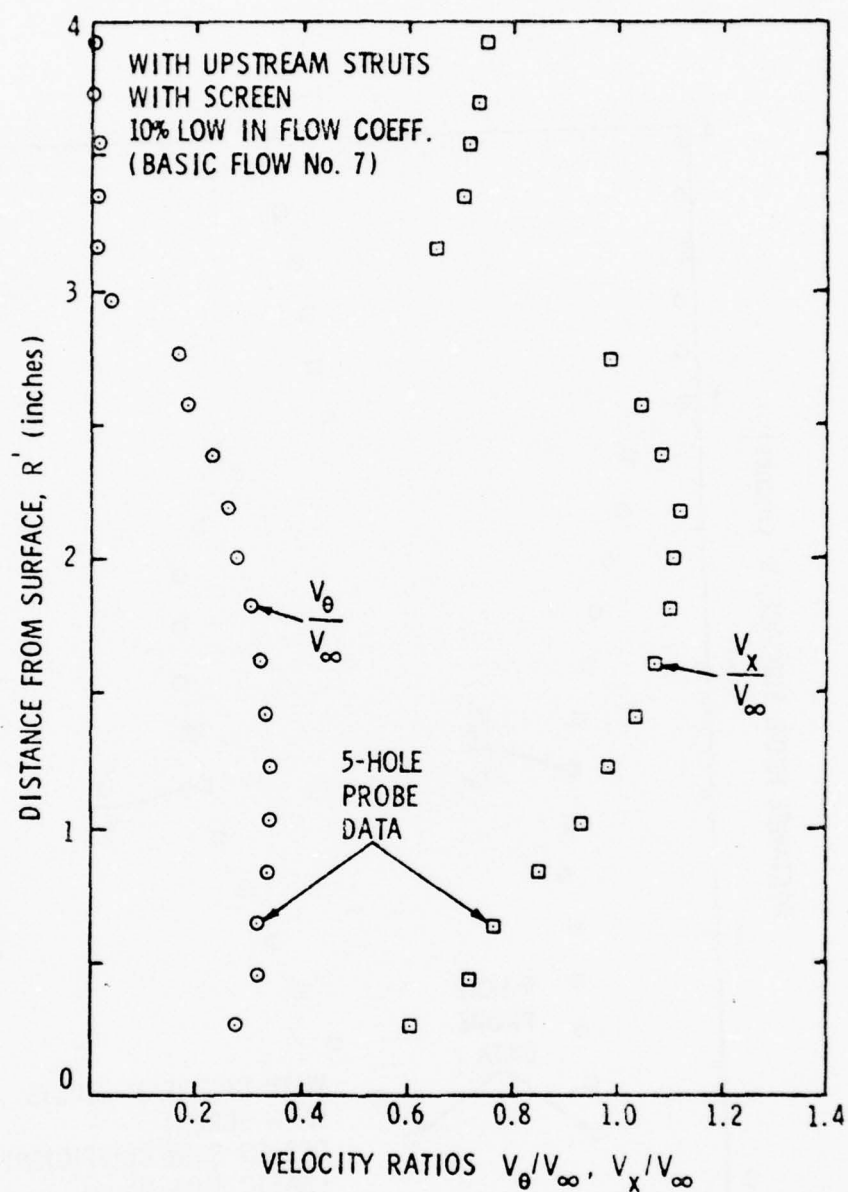


Figure 23. Rotor Outlet Velocity Profiles for Basic Flow No. 7

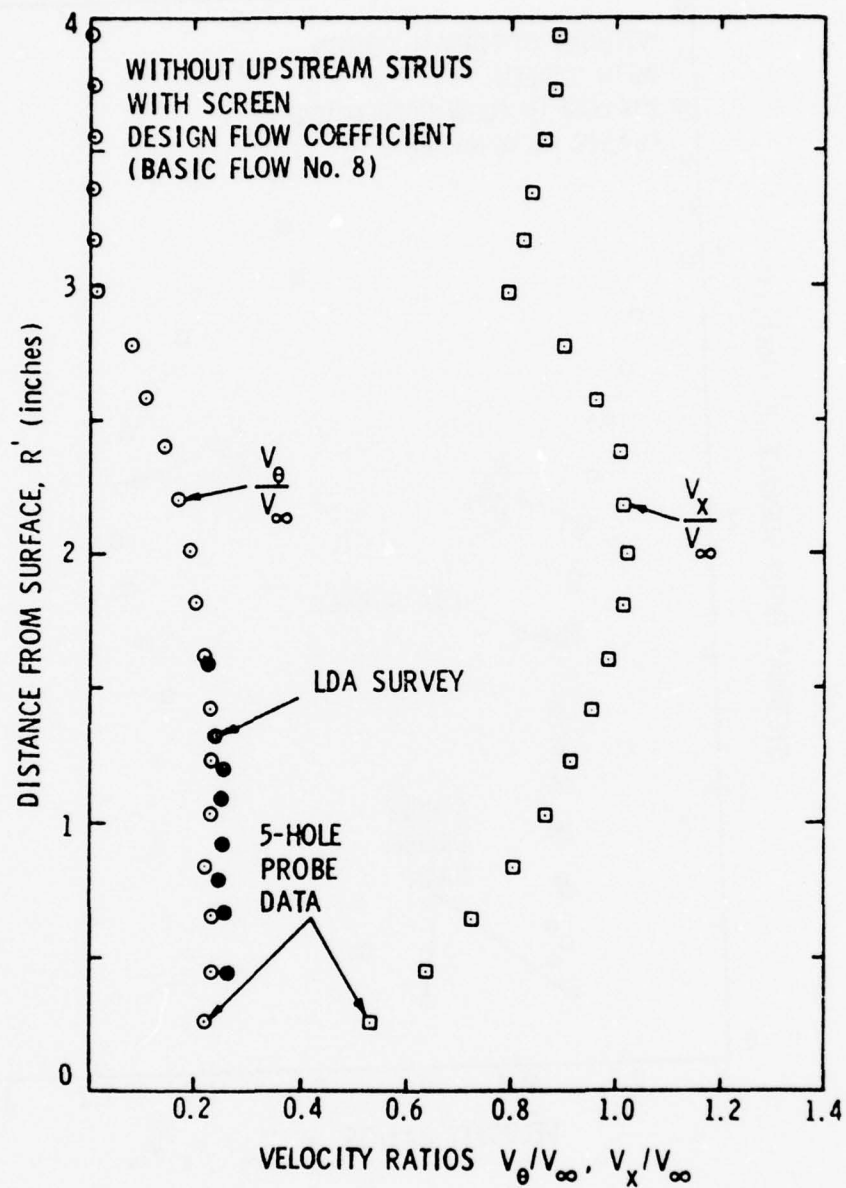


Figure 24. Rotor Outlet Velocity Profiles for Basic Flow No. 8

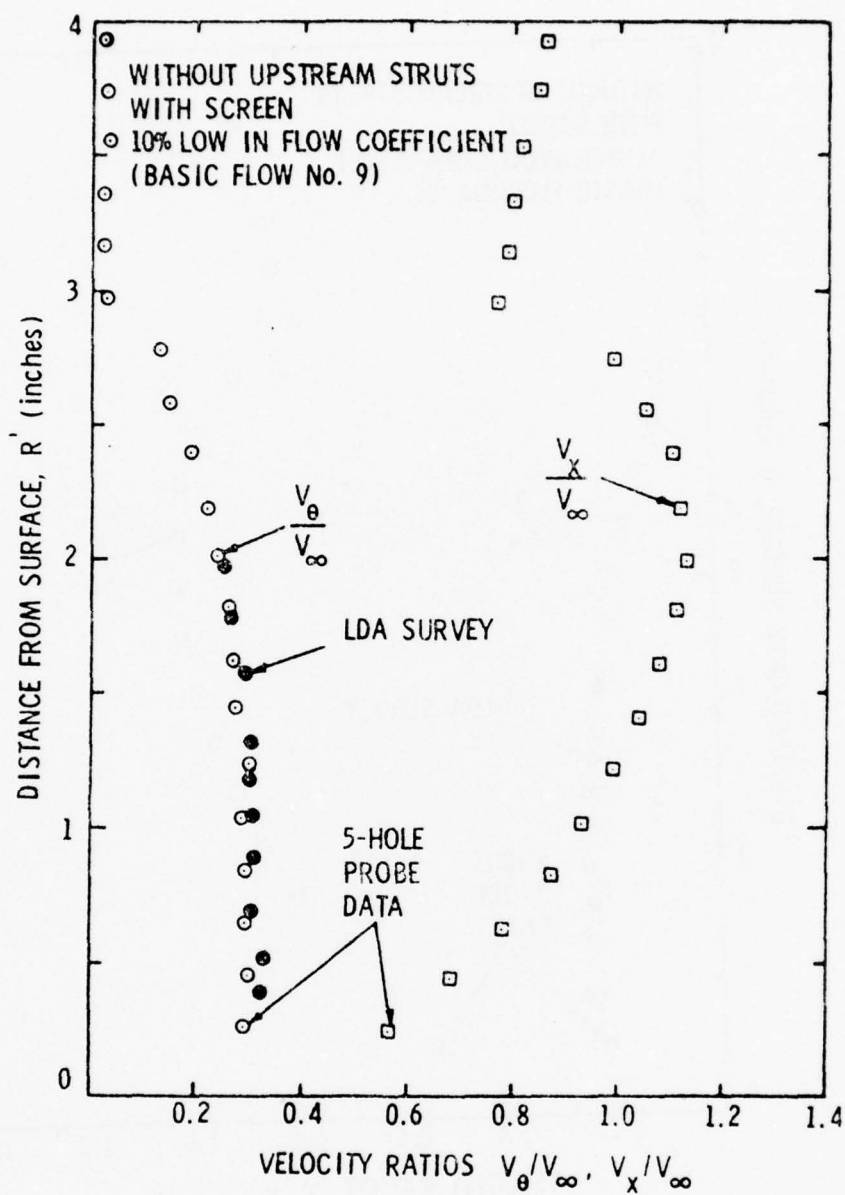


Figure 25. Rotor Outlet Velocity Profiles for Basic Flow No. 9

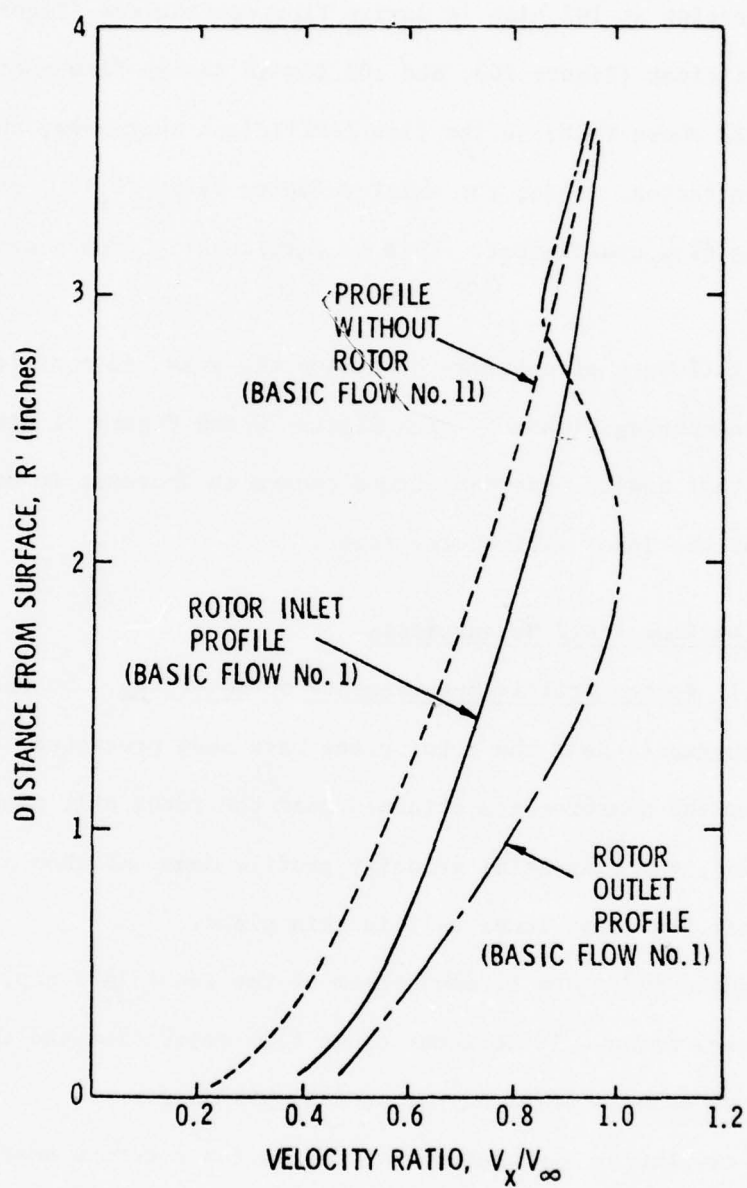


Figure 26. Comparison of Velocity Profiles for Basic Flow No. 1

A comparison of tangential velocity ratios (V_θ/V_∞) obtained with the rotor operating at 10% high in design flow coefficient (Figure 21), design flow coefficient (Figure 20), and 10% low in design flow coefficient (Figure 22) shows that, as the flow coefficient increases, the amount of turning decreases. Also, the axial velocity ratio (V_x/V_∞) decreases with increasing flow coefficient. This is particularly true near the inner wall.

The influence of upstream struts on the measured profiles can be noted by comparing Figure 17 with Figure 20 and Figure 22 with Figure 18. It shows that adding upstream struts causes an increase in both V_θ/V_∞ and V_x/V_∞ near the inner wall of the rotor.

3.4 Vortex Flow Field Measurements

3.4.1 Vortex Profile Measurements on Rotor Cap. So far, only the flow measurements near the rotor plane have been presented. As can be noted from the measurements obtained near the rotor exit plane (Figures 17 through 25), the tangential velocity profile does not show a well defined vortex near the rotor inner wall in this plane.

As shown in Figure 5, downstream of the rotor is a cap. A conical cap was used because it does not cause flow separation and therefore the flow can be calculated along the conical boundary.

The cavitation associated with the vortex occurred near the end of this cap. Therefore, flow measurements were obtained at the end of the cap. In addition, static pressure taps were located along the cap and these results will be discussed in the next section.

The behavior of the vortex when subjected to basic flow changes can be seen from measurements made at the end of the cap. These measurements

were made using a Laser Doppler Anemometer (LDA). Preliminary flow field observations using dye showed that a probe could not be used to measure the vortex structure near the end of the cap. Introduction of any probe into the vortex core caused vortex breakdown which resulted in the vortex core diffusing rapidly in front of the probe. This led to the development of the LDA for the 48-inch water tunnel.

A picture of the LDA setup for the 48-inch water tunnel is shown in Figure 27. The dual beam-backscatter mode was used for the measurements because optics could not be mounted on both sides of the water tunnel. In the dual beam mode, the laser beam is separated into two parallel beams of equal intensity. These two beams cross and focus at the focal point of a lens. The scattered light originating from the focal point is collected through the focusing lens and is directed to a photomultiplier tube. A Spectra Physics Model 164 Argon-ion laser was used as the coherent light source. A Thermo-Systems Model 1090 Tracker was used to process the signal.

The measurements of the flow structure at the end of the cap for several basic flows are shown in Figures 28 through 34. A discussion of the accuracy of these measurements is given in Appendix A. These figures show the complexity of the vortex. First of all, the vortex is not steady so that the measurements represent the mean value at a given radial position. In addition, the laser light probe volume is of finite size which will also contribute to the averaging process. Secondly, there were extremely large variations in the tangential velocity for some basic flows which are not shown in the figures. Variations as large as twice the mean tangential velocity were measured.

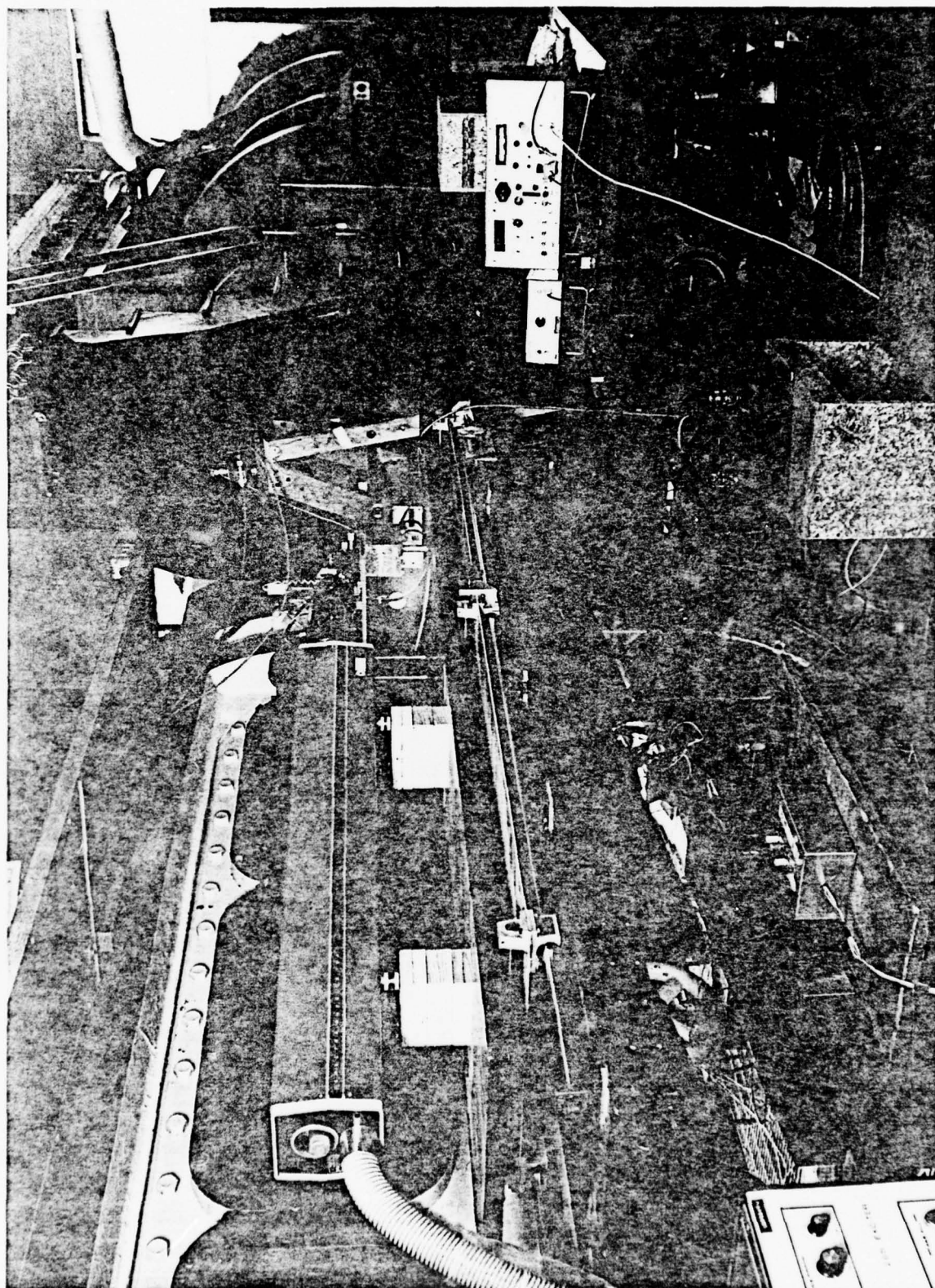


Figure 27 - Picture of LDA for 48-Inch Water Tunnel

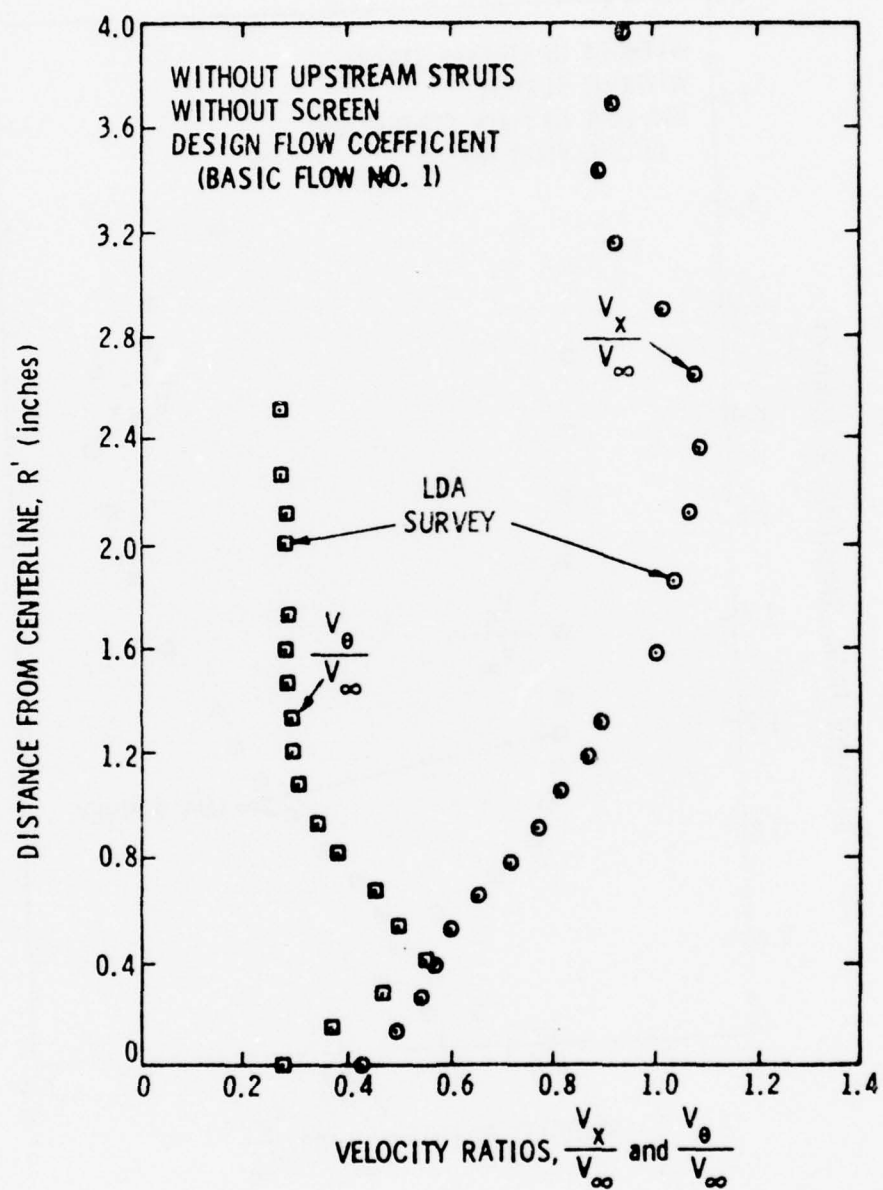


Figure 28. Velocity Profiles on Rotor Cap for Basic Flow No. 1

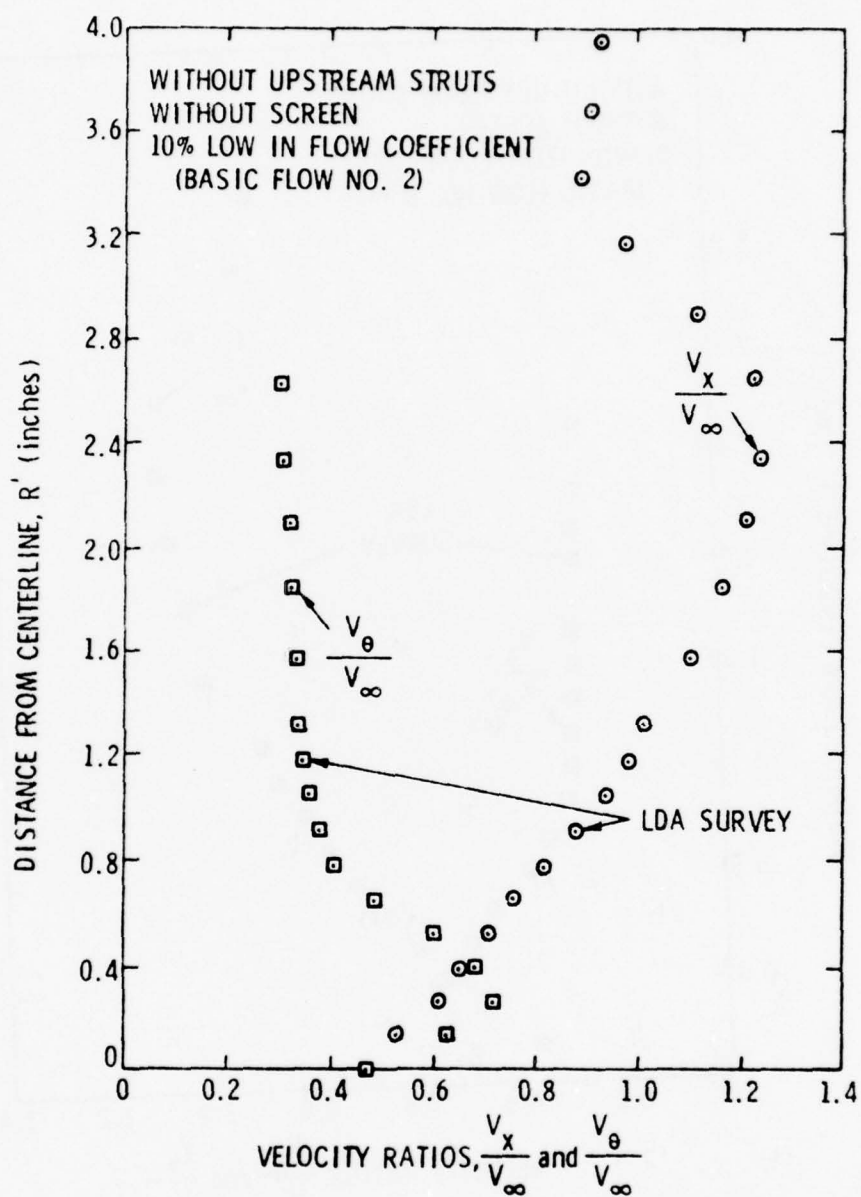


Figure 29. Velocity Profiles on Rotor Cap for Basic Flow No. 2

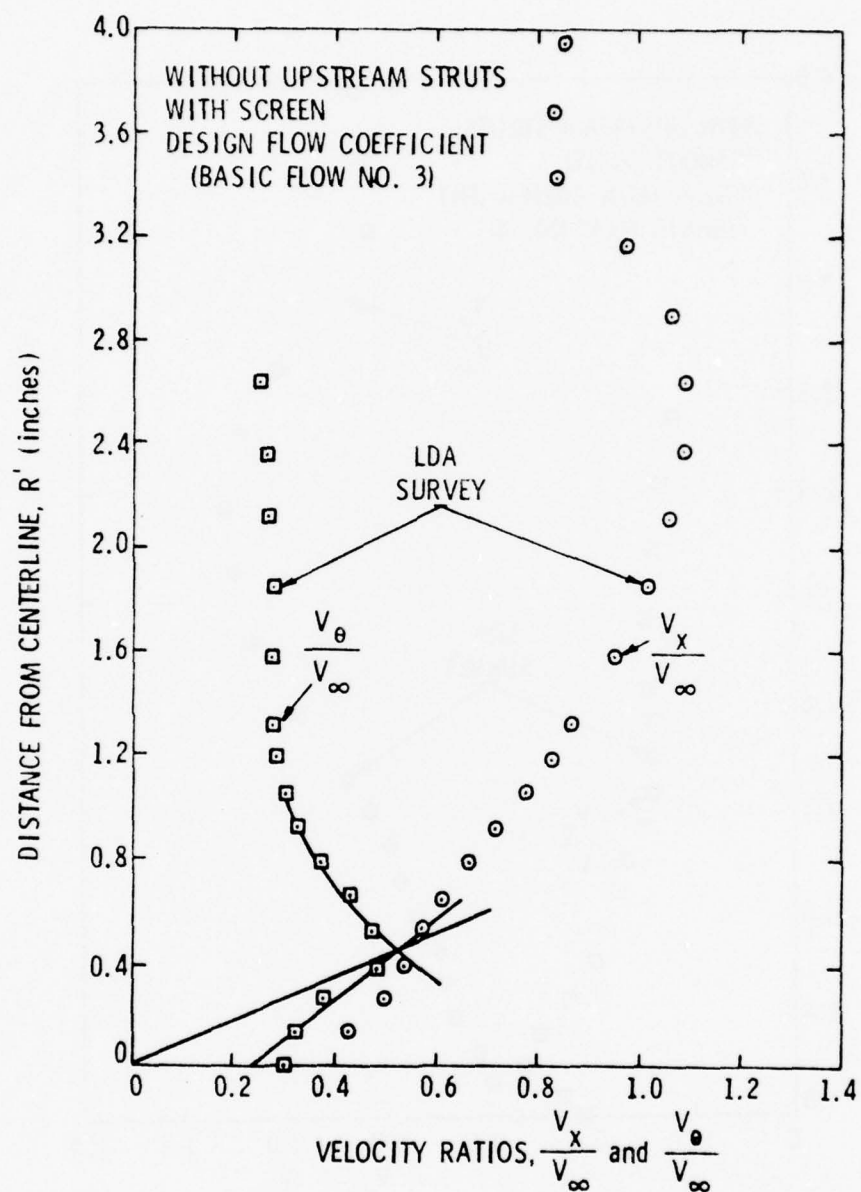


Figure 30. Velocity Profiles on Rotor Cap for Basic Flow No. 3

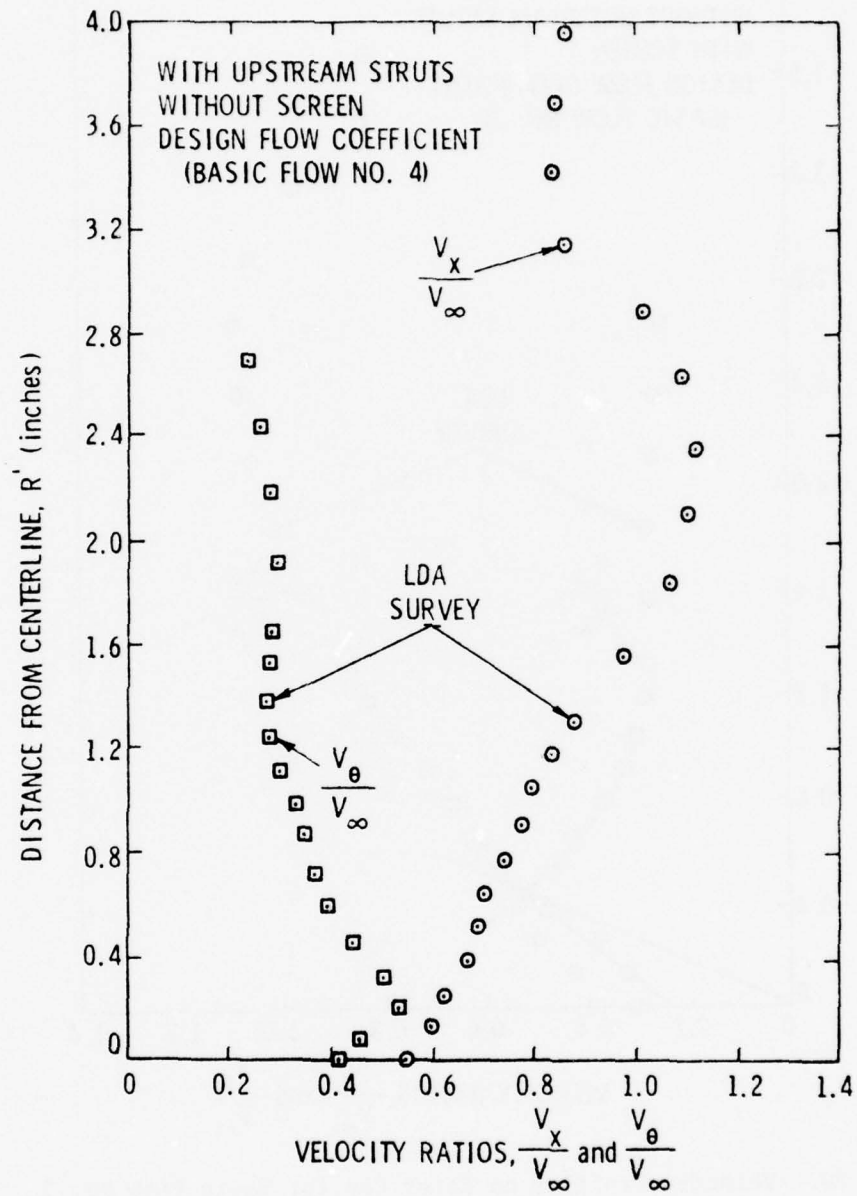


Figure 31. Velocity Profiles on Rotor Cap for Basic Flow No. 4

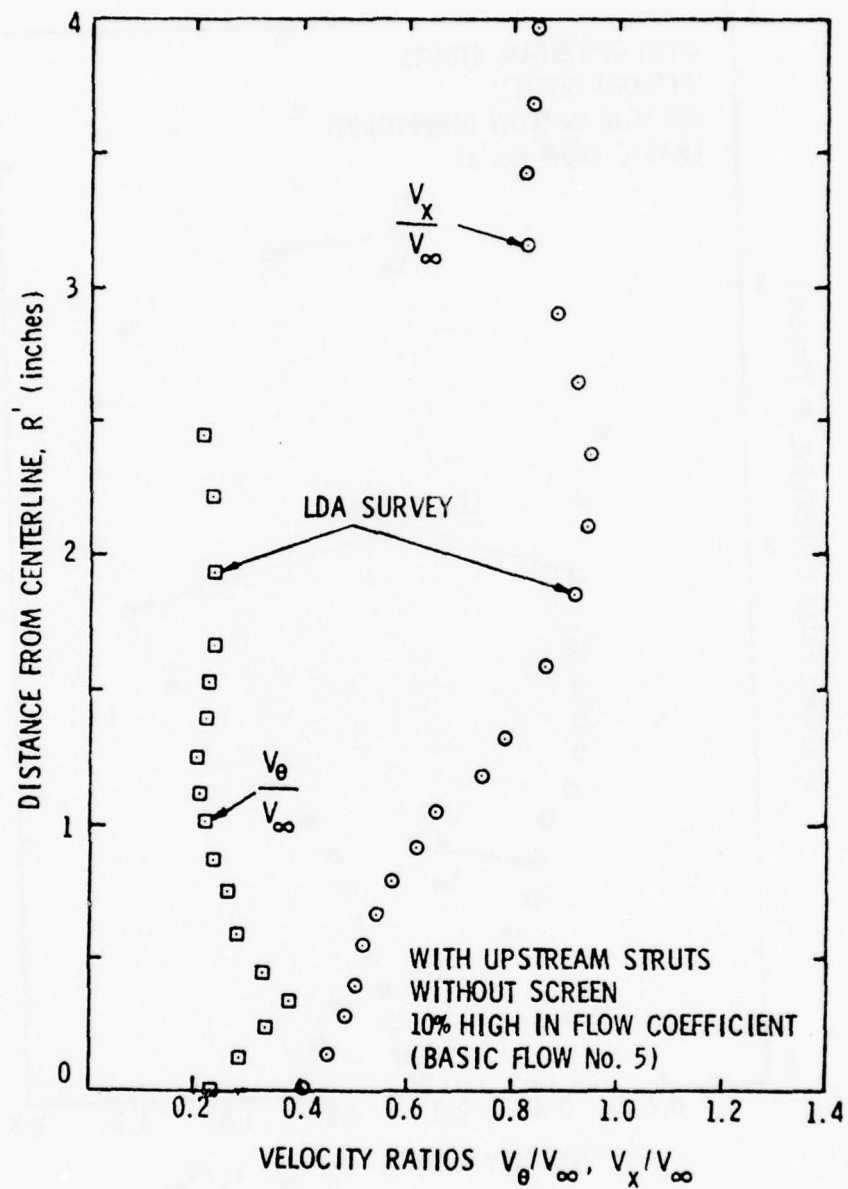


Figure 32. Velocity Profiles on Rotor Cap for Basic Flow No. 5

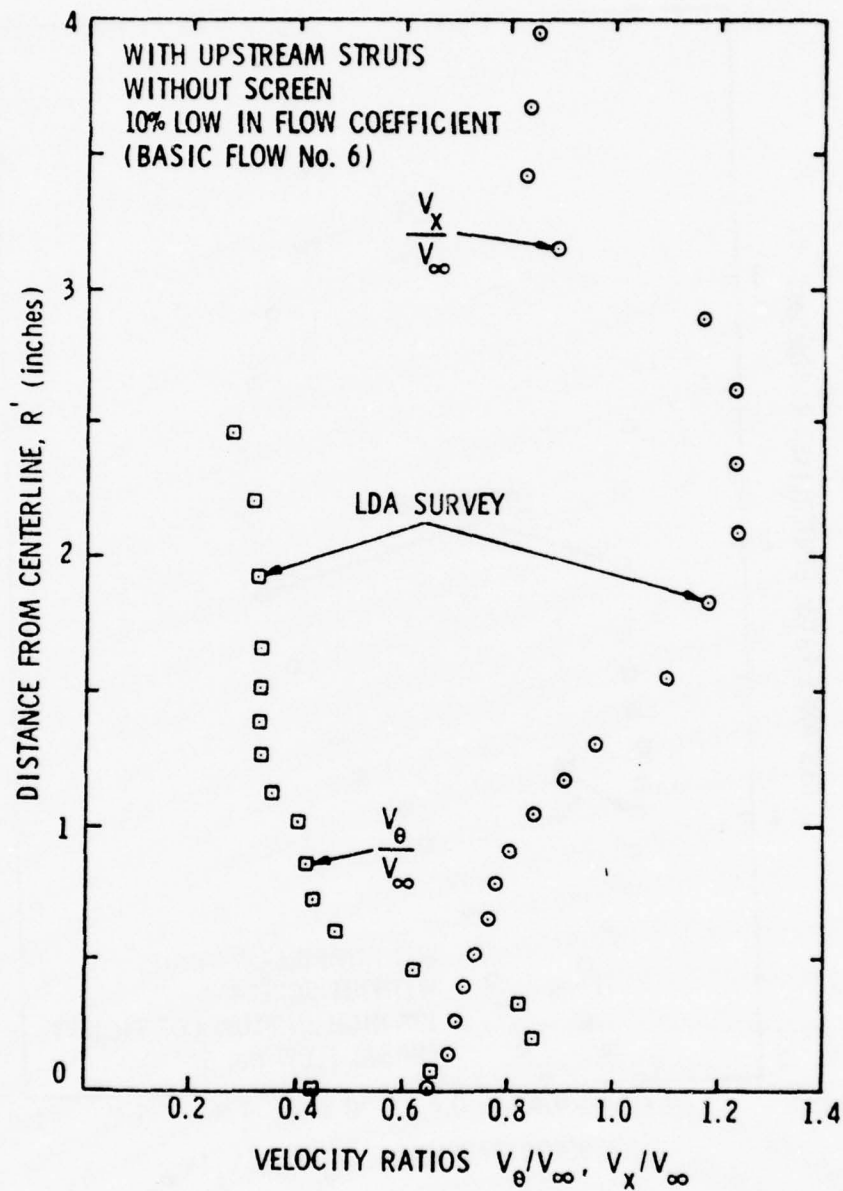


Figure 33. Velocity Profiles on Rotor Cap for Basic Flow No. 6

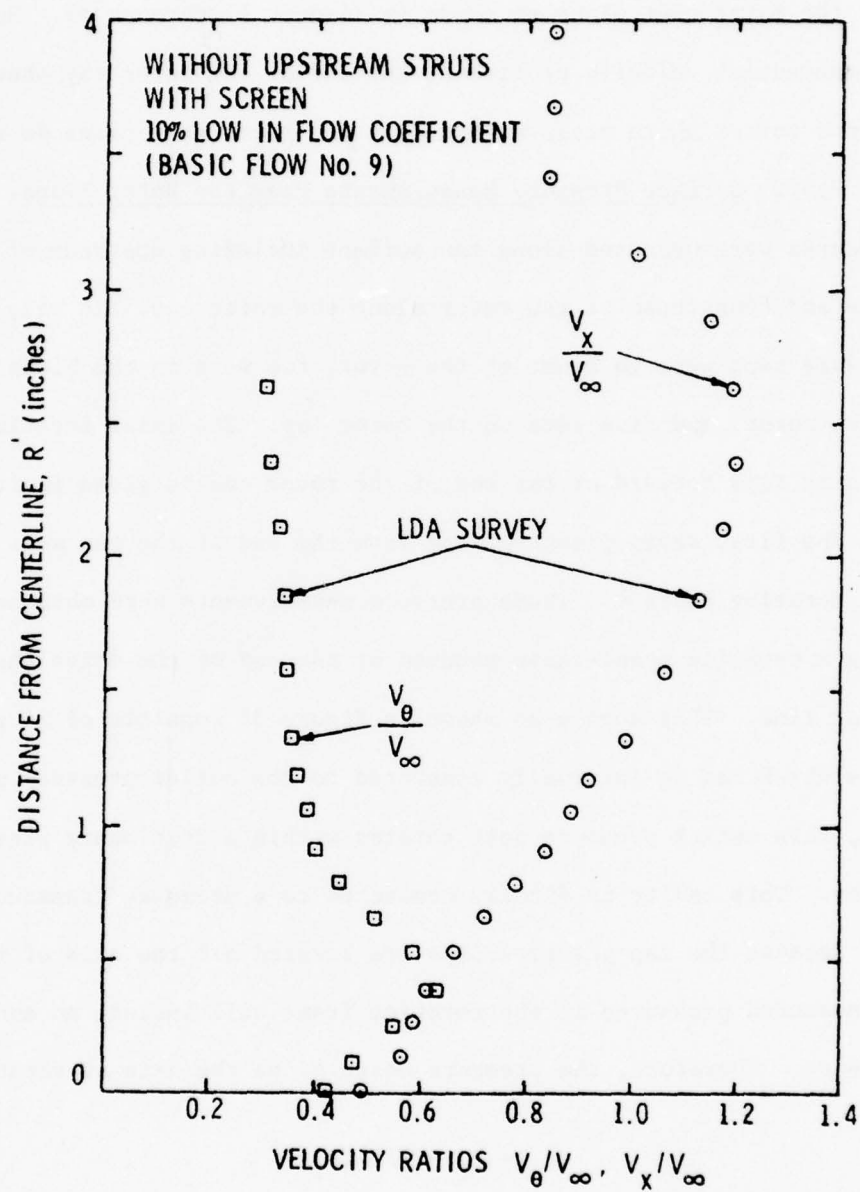


Figure 34. Velocity Profiles on Rotor Cap for Basic Flow No. 9

The axial velocity profile at the end of the cap shown in Figures 28 through 34 has a similar shape as the axial velocity profile measured near the rotor exit plane as shown in Figures 17 through 25. However, the tangential velocity profile at the end of the rotor cap shows a well defined vortex which measurements near the rotor exit plane do not show.

3.4.2 Surface Pressure Measurements Near the Rotor Plane. Static pressures were measured along the surface including upstream of the rotor plane and downstream of the rotor along the rotor cap. In all, five pressure taps were in front of the rotor, two were in the blade passage of the rotor, and five were on the rotor cap. The axial location of the pressure taps forward of the end of the rotor cap is given in Table 4.

The first seven pressure taps from the end of the cap were located on a rotating surface. These pressure measurements were obtained by using a rotating scani-valve mounted at the end of the drive shaft on the center line. This device as shown in Figure 35 consists of 24 pressure ports which can be internally connected to the outlet pressure port. In turn, this outlet pressure port rotates within a stationary pressure cavity. This cavity is finally connected to a pressure transducer.

Because the cap pressure taps are located off the axis of rotation, the measured pressures in the rotating frame will include an additional pressure. Therefore, the pressure measured on the axis of rotation is

$$P_{\text{C}} = P_{\text{T}} - 1/2\rho(r_{\text{T}}\hat{\omega})^2 \quad , \quad (17)$$

where $\hat{\omega}$ is the angular velocity and r_{T} is the distance from the axis of rotation to the tap location. The static pressure coefficient for the surface pressure tap becomes

TABLE 4
LOCATION OF SURFACE PRESSURE TAPS

Tap No.	Distance Forward of End of Rotor Cap (inches)
<u>On Stationary Surface</u>	
P_{T_1}	15.50
P_{T_2}	9.50
P_{T_3}	7.90
P_{T_4}	5.03
P_{T_5}	3.60
<u>On Rotor</u>	
P_{T_6}	3.34
P_{T_7}	2.71
<u>On Rotor Cap</u>	
P_{T_8}	0.66
P_{T_9}	0.50
$P_{T_{10}}$	0.34
$P_{T_{11}}$	0.17
$P_{T_{12}}$	0.00

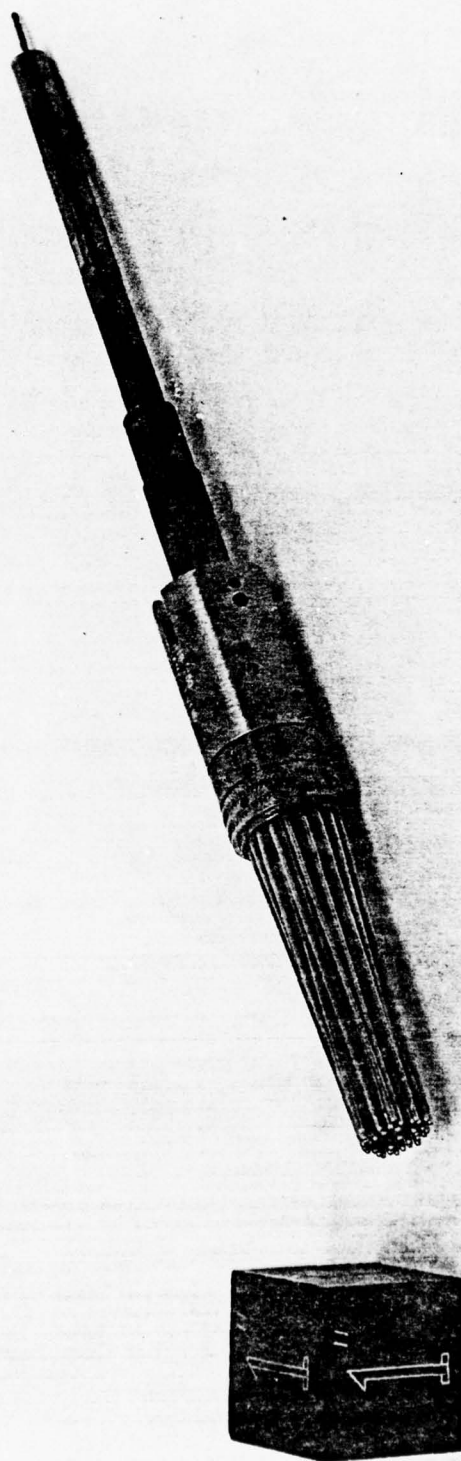


Figure 35 - Picture of the Rotating Scani-Valve

$$C_{P_{S_T}} = \frac{P_T - P_S}{1/2 \rho V_\infty^2} = \frac{P_L - P_S}{1/2 \rho V_\infty^2} + \left\{ \frac{r_T}{R_R \phi} \right\}^2, \quad (18)$$

where ϕ is the rotor flow coefficient and R_R is the rotor radius.

The static pressure coefficients measured on the body surface without the rotor are shown in Figure 36. The accuracy of these measurements is discussed in Appendix A. The effect of a rotating cap on the flow field can be seen by the decrease in static pressure coefficient near the end of the rotor cap.

The effect of adding the rotor to the surface is shown in Figure 37. In this figure, the pressure coefficients along the surface are compared for Basic Flow No. 11 without a rotor but with cap and Basic Flow No. 1 with a rotor. The rotor causes a pressure rise at the exit plane (P_{T_7}), and this pressure progressively decreases downstream. An apparent pressure minimum occurs at the end of the cap. In addition, the pressure coefficients upstream of the rotor plane are decreased. This indicates an increase in velocity to the rotor. The influence of the rotor on the surface pressure coefficient becomes small approximately two rotor diameters upstream.

A more detailed picture of the pressure coefficients on the cap downstream of the rotor is given in Figures 38 and 39. In all cases, the pressure coefficient decreased along the cap with the measured minimum at the end of the cap and the pressure coefficient decreased at each tap location as the velocity increased. The most interesting result is the effect of adding upstream struts (Figure 39) on the pressure coefficients along the cap. In comparing Figure 38 to Figure 39, the pressure coefficients are lower along the cap without upstream struts with a

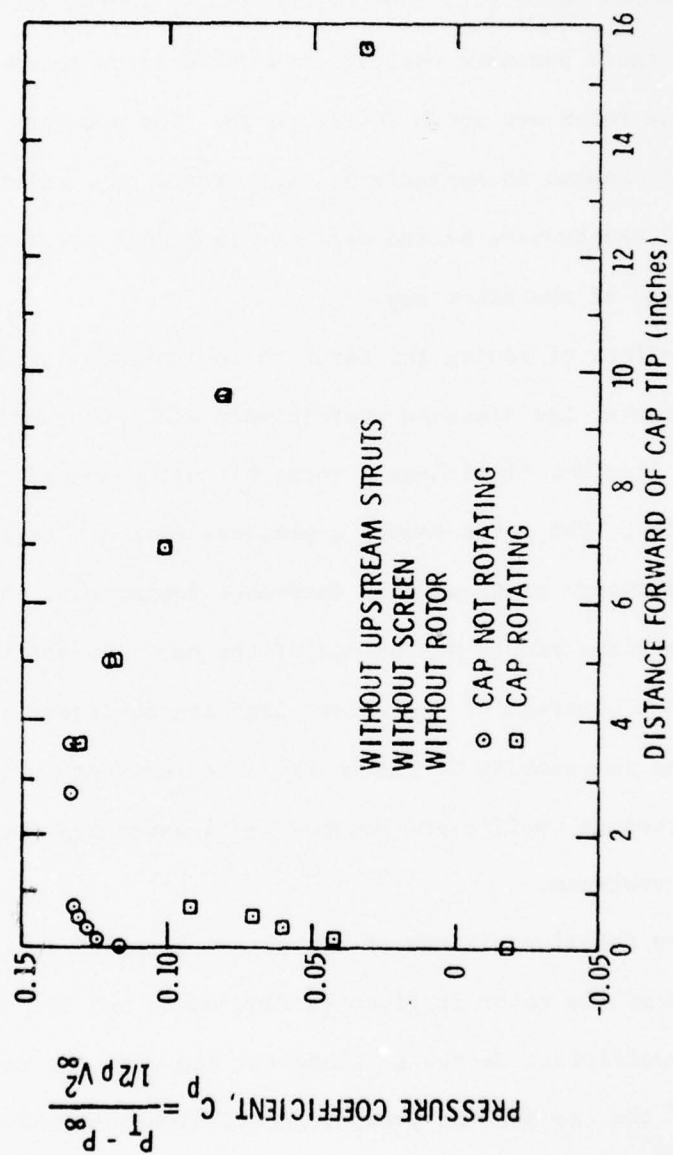


Figure 36. Static Pressure Coefficients Along Surface without Rotor

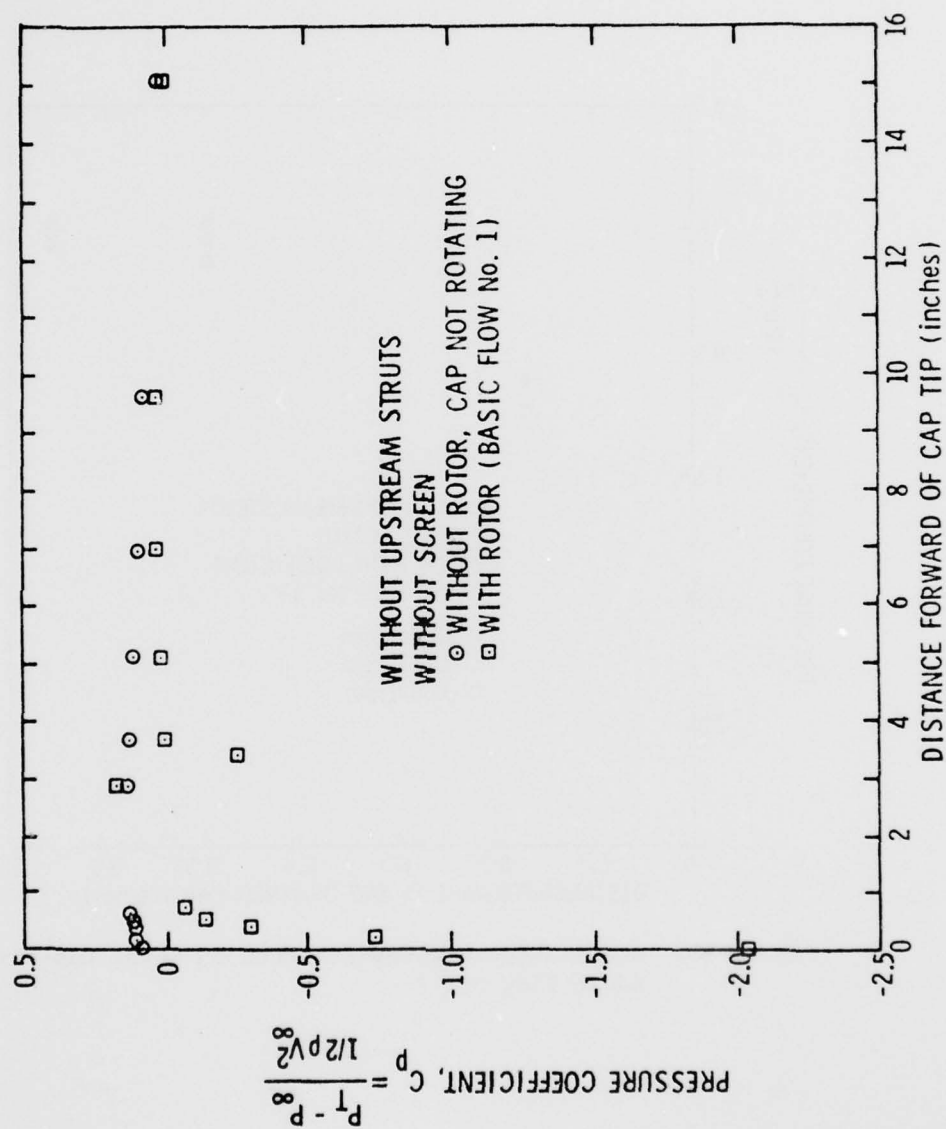


Figure 37. Static Pressure Coefficients Along Surface for Basic Flow No. 1

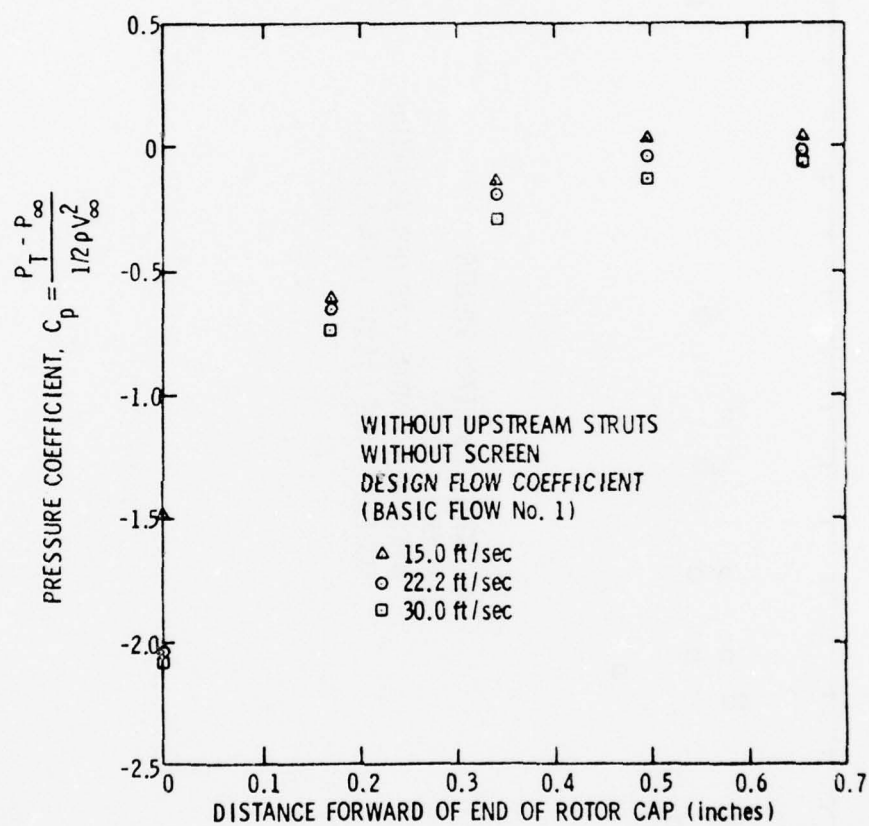


Figure 38. Static Pressure Coefficients on Rotor Cap for Basic Flow No. 1

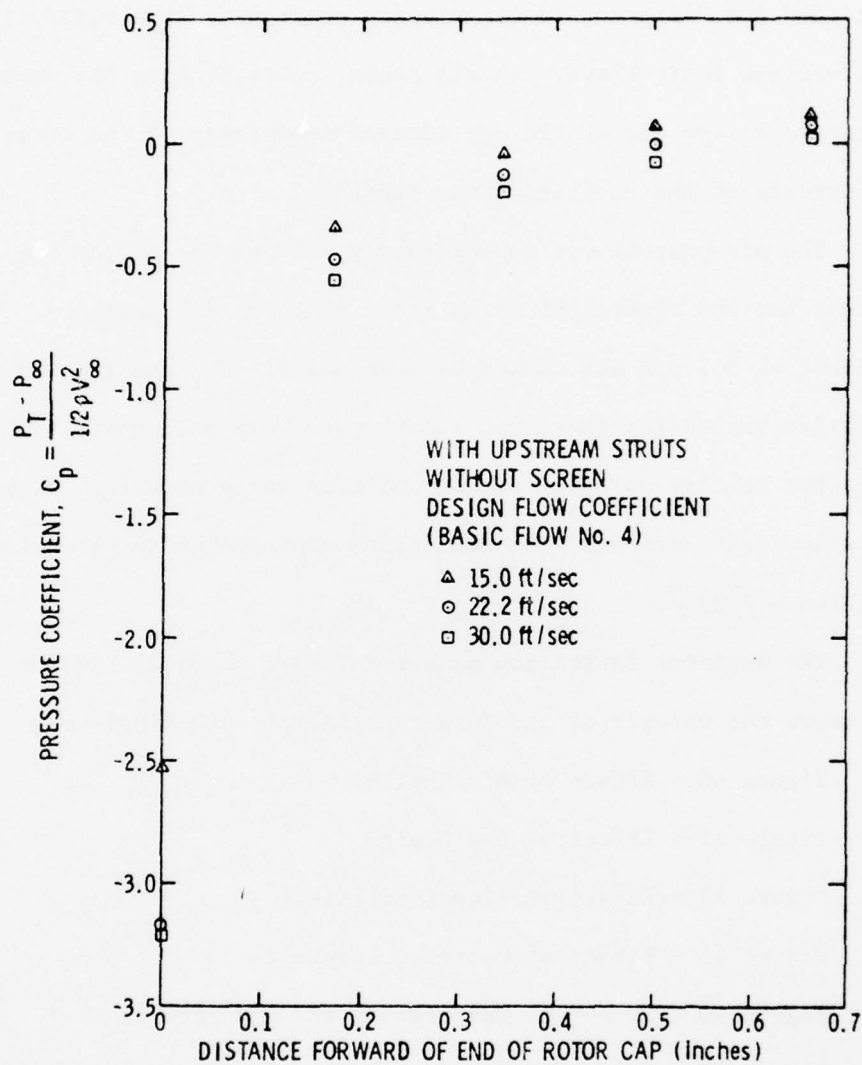


Figure 39. Static Pressure Coefficients on Rotor Cap for Basic Flow No. 4

notable exception near the end of the rotor cap. Near the end, the pressure coefficient is lower with added upstream struts.

3.4.3 Vortex Cavitation Data. Desinent cavitation number data were obtained for different inlet velocity profiles to the rotor, i.e., for the various Basic Flows. In all cases, cavitation in the vortex system occurred on the end of the cap located downstream of the rotor. The occurrence of the cavitation was sporadic.

The air content was approximately 3.1 ppm for all of the experiments except for one experiment which had a range of air contents. The air content of 3.1 ppm was chosen because gas effects are reduced and the relative saturation level was always much less than unity. The abbreviation ppm denotes moles of air per million moles of water. A more detailed description of the cavitation experiments is given in Reference [33].

The desinent cavitation number data are shown in Figures 40 through 46 where the effects of the following factors are displayed:

Figure 40 - Effect of Air Content

Figure 41 - Effect of Cap Design

Figure 42 - Effect of Flow Coefficient

Figure 43 - Effect of Upstream Struts

Figure 44 - Effect of Upstream Struts and Screens

Figure 45 - Effect of Screen and Flow Coefficient with Struts

Figure 46 - Effect of Screens and Flow Coefficient without Struts

Thus, Figures 40 through 46 show the effects on the desinent cavitation number due to air content level and cap design in addition to basic flow configurations.

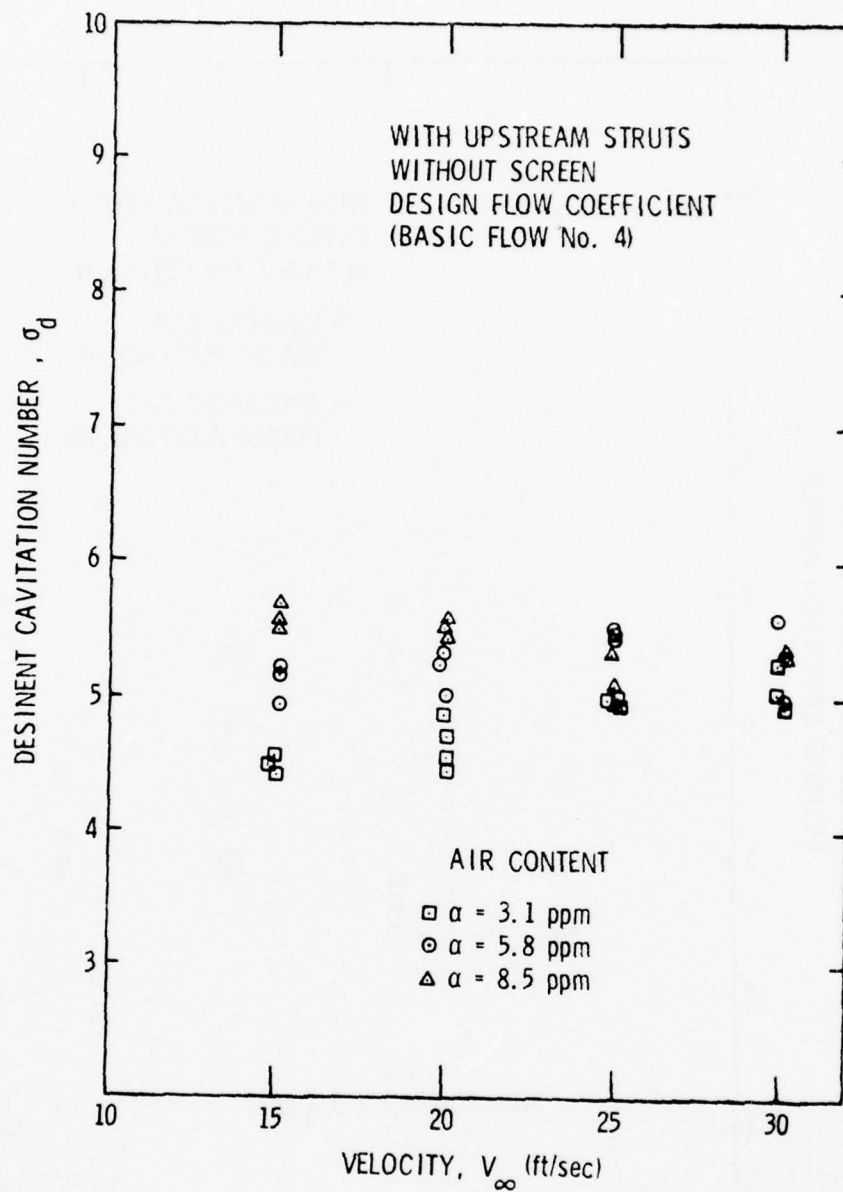


Figure 40. Cavitation Data - Effect of Air Content
(Basic Flow No. 4)

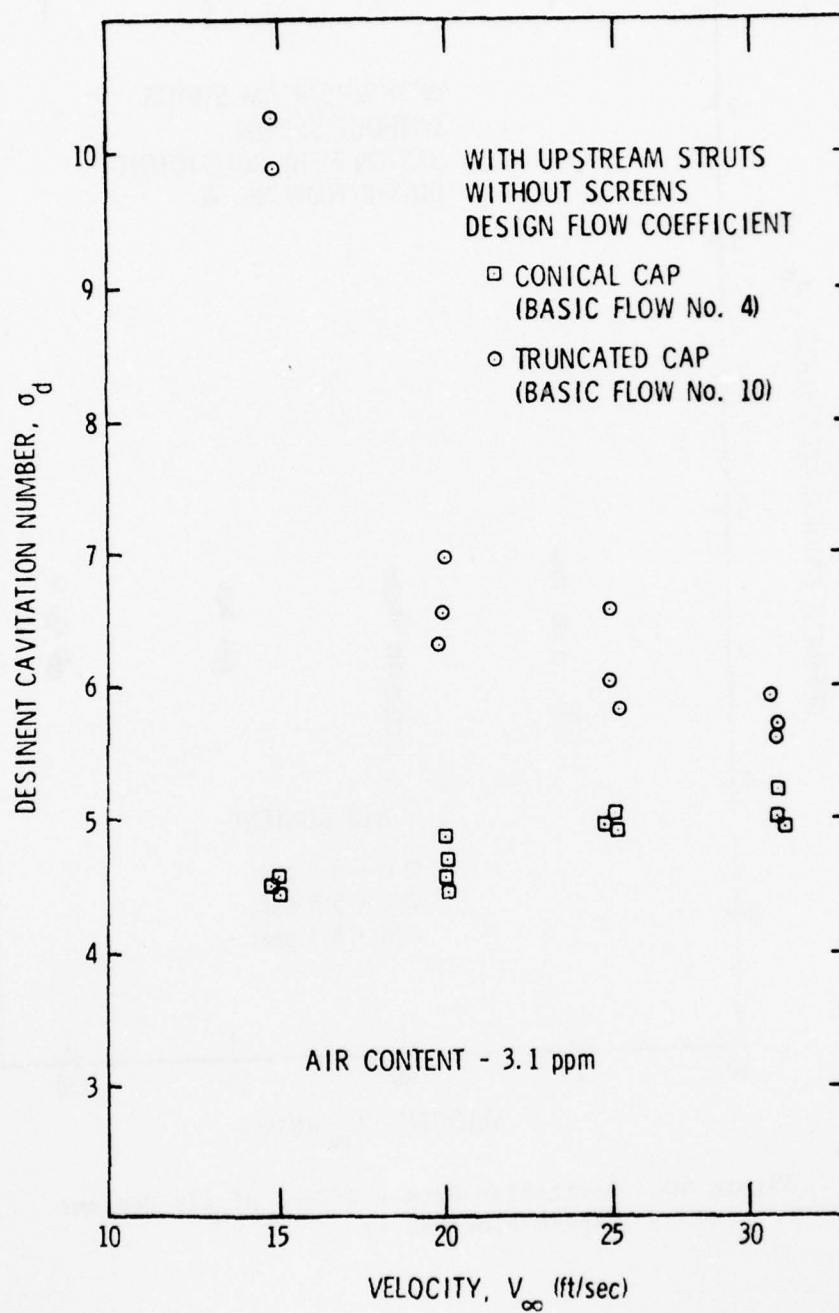


Figure 41. Cavitation Data - Effect of Cap Design
(Basic Flow Nos. 4 and 10)

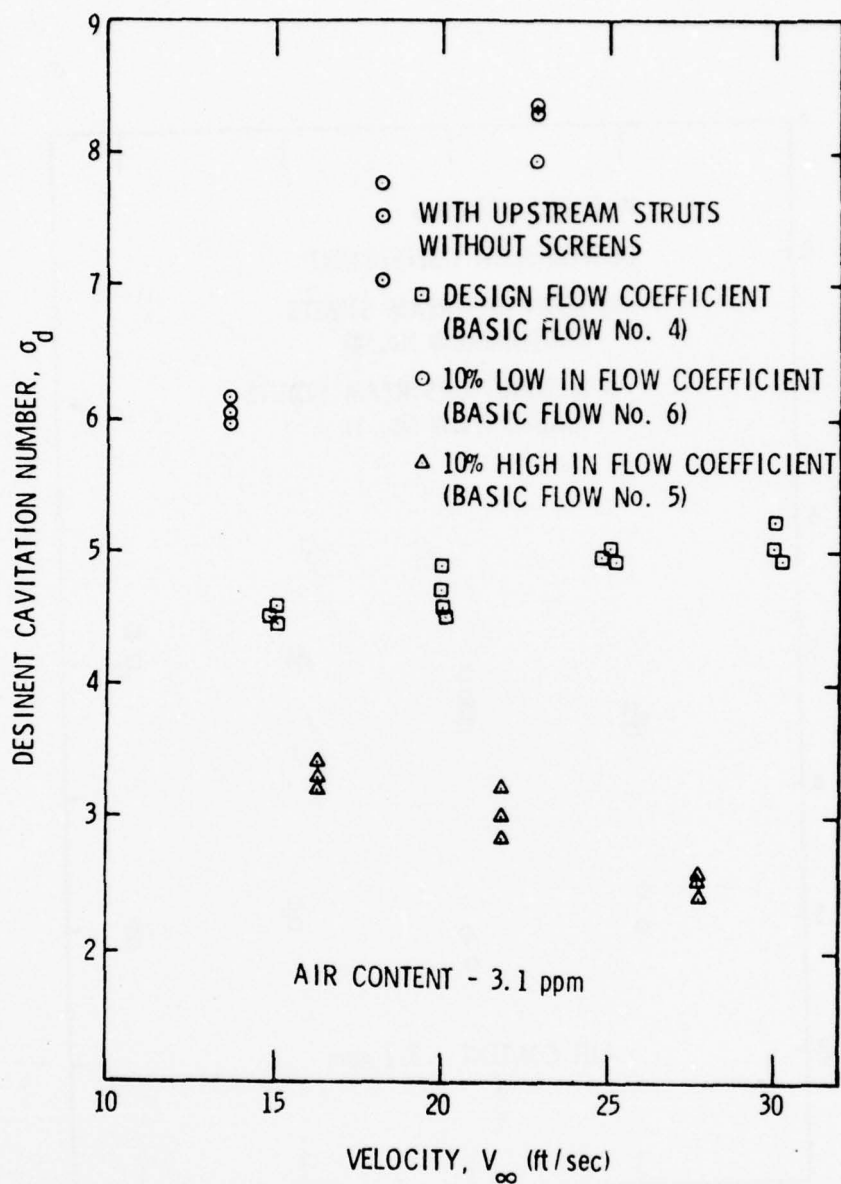


Figure 42. Cavitation Data - Effect of Flow Coefficient (Basic Flow Nos. 4, 5, and 6)

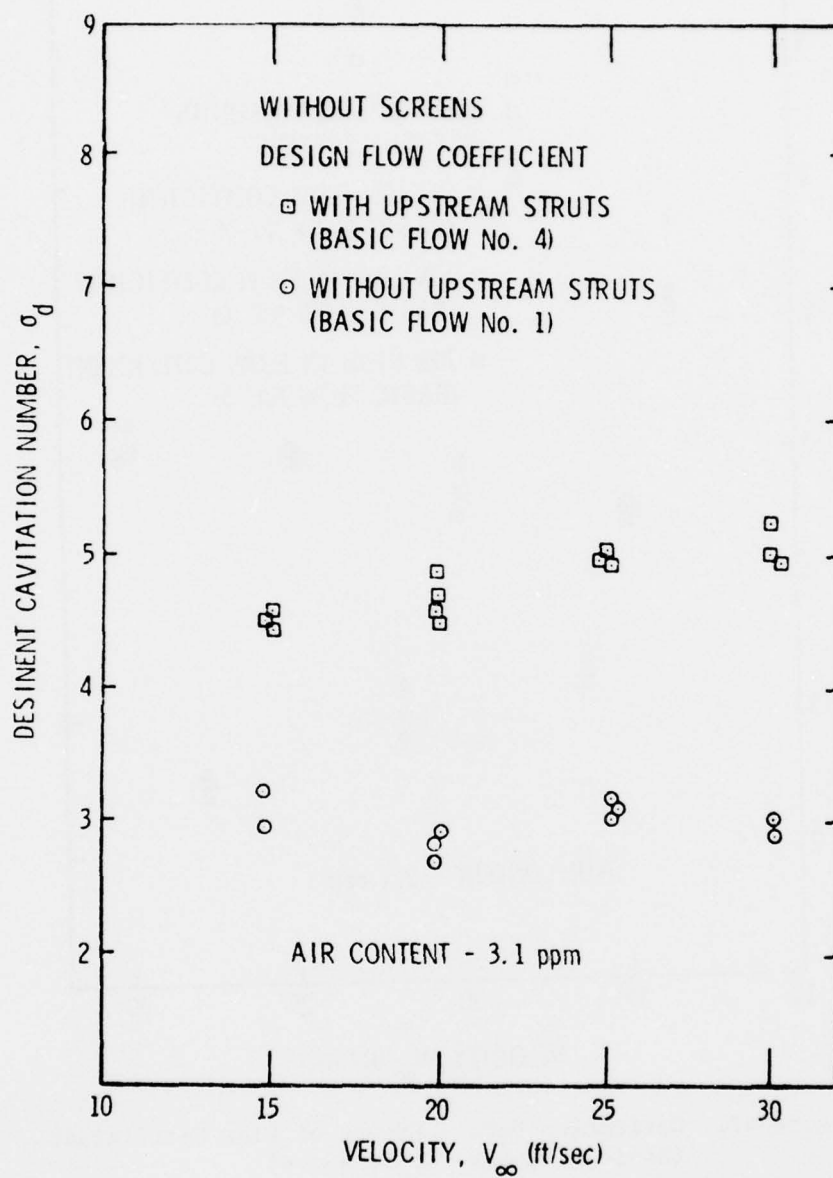


Figure 43. Cavitation Data - Effect of Struts
(Basic Flow Nos. 1 and 4)

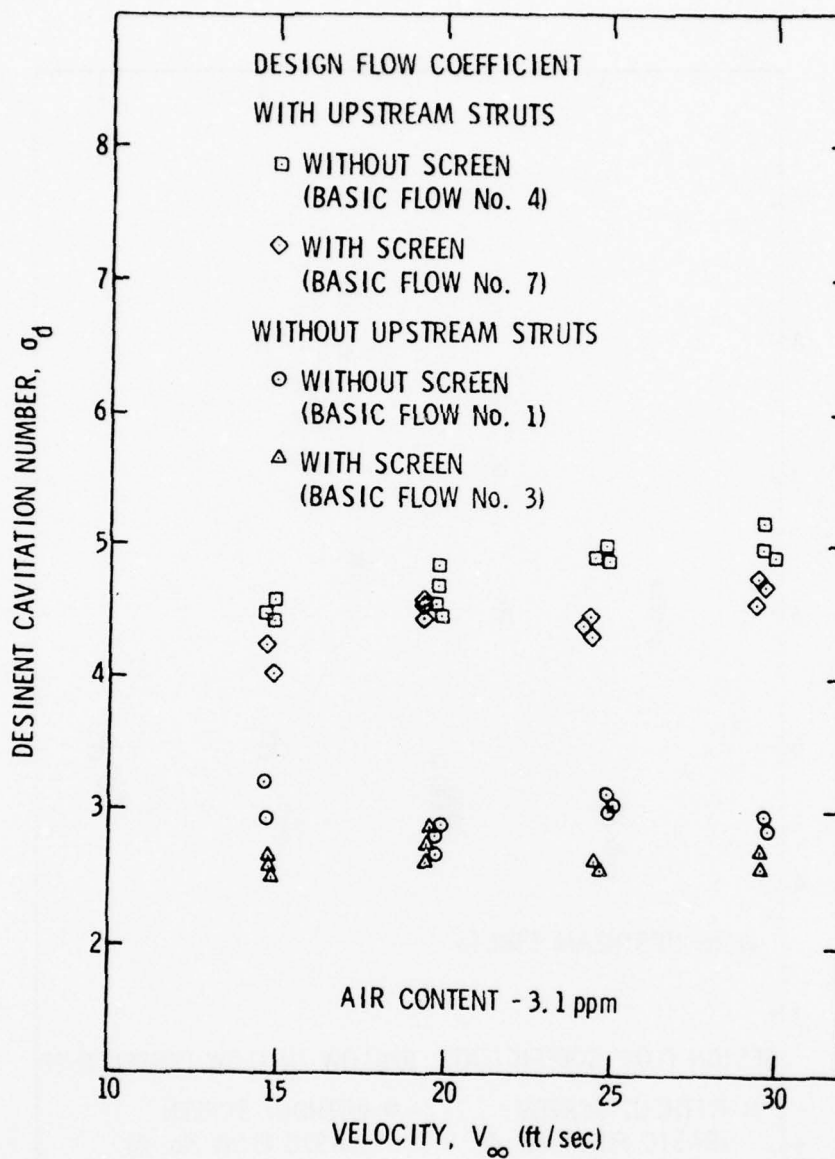


Figure 44. Cavitation Data - Effect of Struts and Screen (Basic Flow Nos. 1, 3, 4, and 7)

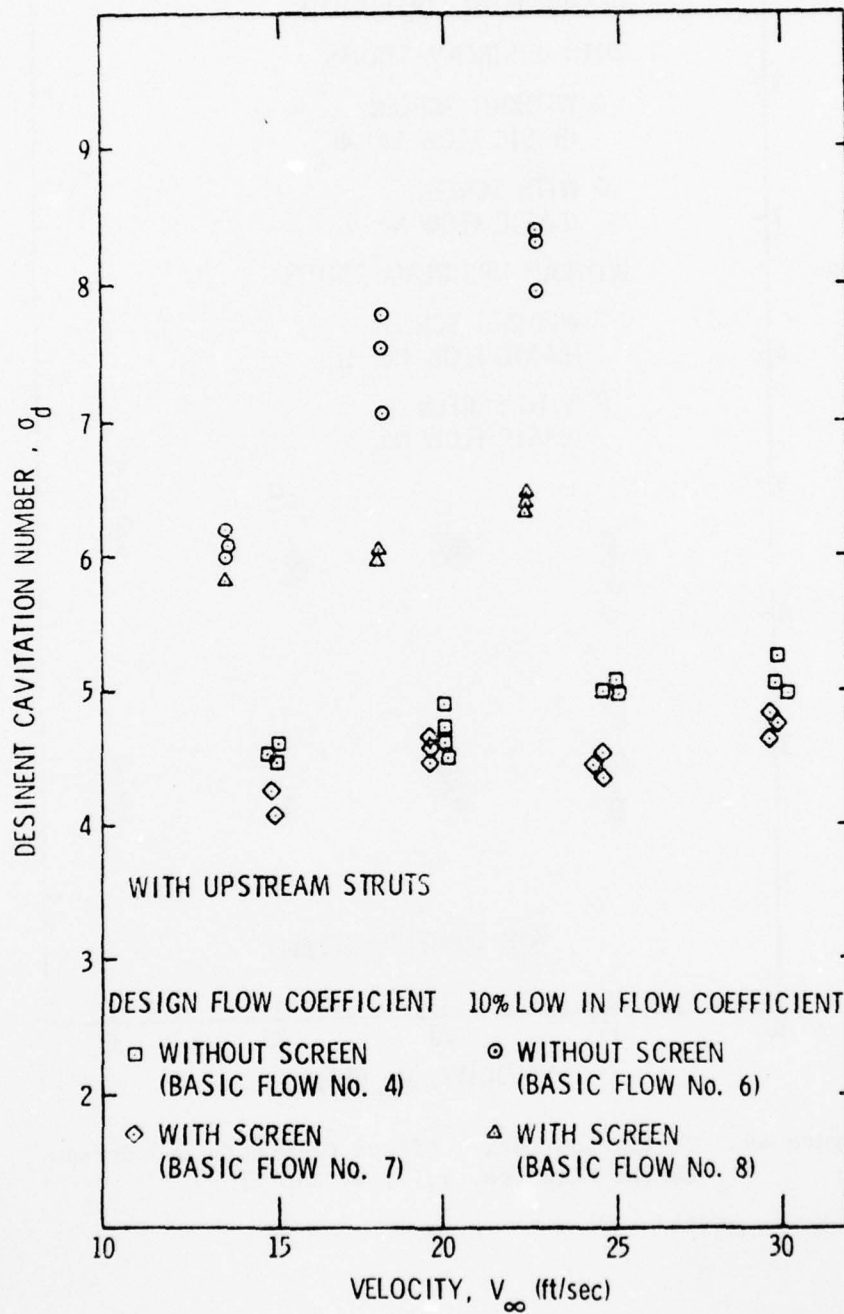


Figure 45. Cavitation Data - Effect of Screen and Flow Coefficient with Struts (Basic Flows Nos. 4, 6, 7, and 8)

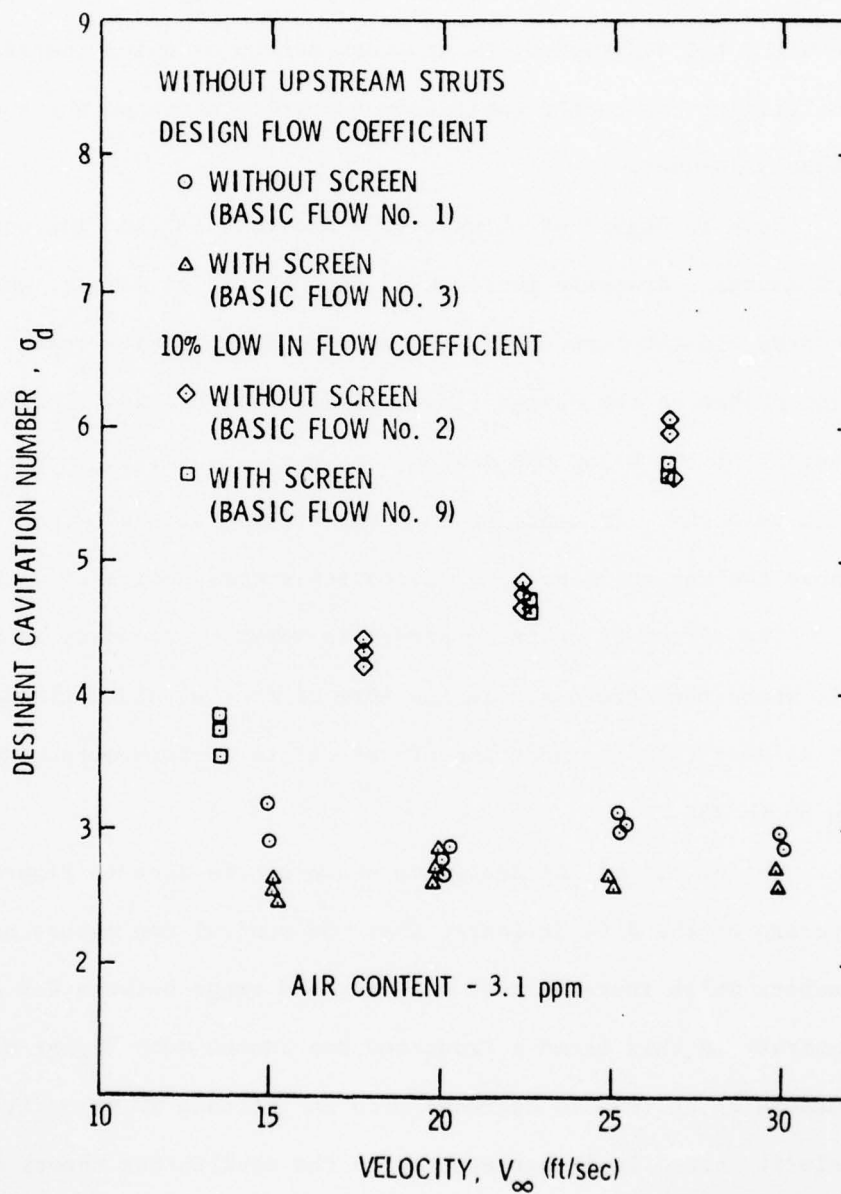


Figure 46. Cavitation Data - Effect of Screen and Flow Coefficient without Struts (Basic Flows Nos. 1, 2, 3, and 9)

In general, an increase in gas content, the addition of upstream struts, or a 10% decrease in flow coefficient causes the cavitation number to increase for a constant Reynolds number. In contrast to these results, the addition of an upstream screen or a 10% increase in flow coefficient causes the cavitation number to decrease for a constant Reynolds number.

Data in Figure 42 shows that a decrease in the flow coefficient by 10% causes a dramatic increase in the cavitation number, whereas a 10% increase in the flow coefficient causes the opposite trend. The cavitation number at the design flow coefficient increases slowly with velocity, whereas at 10% below the design flow coefficient, it increases rapidly with velocity. In contrast to these trends, at a flow coefficient 10% above the design value, the cavitation number decreases with velocity.

The effect of upstream struts is shown by the data in Figures 43 and 44, where the struts are in the form of four struts upstream of the rotor. It is seen that the addition of the struts increases the cavitation number by 50 to 70%.

The effect of cap design is shown by the data in Figure 41. The average of the data indicates that the conical cap causes cavitation numbers which increase with velocity and range between 4.5 and 5.1. In contrast to this trend a truncated cap causes much higher cavitation numbers which tend to decrease with an increase in velocity. This velocity trend is in agreement with the equilibrium theory discussed in Chapter 2. Assuming that $C_{p_{min}}$ and P_G are essentially constant, then Equation (7) can be expressed as

$$\sigma_d = \text{constant} + \frac{\text{constant}}{V_\infty^2} \quad (19)$$

The data for the truncated cap approximate this trend. Apparently, the separated flow increases the residence time of bubbles in the low pressure region which accentuates the gas effects predicted by the equilibrium theory.

The data in Figure 40 for a conical cap also show gas effects on the cavitation number. As the gas content increases, the cavitation number tends to increase.

As discussed in Chapter 2, previous experimental results indicate for vaporous cavitation that

$$\sigma_d \approx -C_{p_{\min}}, \quad (20)$$

assuming that air content effects are small. Therefore, a comparison can be made between the measured pressure coefficients at the end of the cap ($C_{p_{\min}}$) and the average cavitation data (σ_d).

Comparisons are given in Figure 47 for basic flows without struts and in Figure 48 for basic flows with struts. A closer agreement is found for the cases without struts than with struts. However, the correlation between the measured pressure coefficients at the end of the rotor cap and average cavitation data is at best poor. As the free stream velocity is increased, the correlation becomes increasingly worse.

3.5 Summary of Experimental Results

Most of this chapter is comprised of figures showing the flow field measurements and vortex cavitation data for the many basic flows. These measurements define the flow field from the rotor inlet to the end of the rotor cap. The following is a summary of measurements that were made:

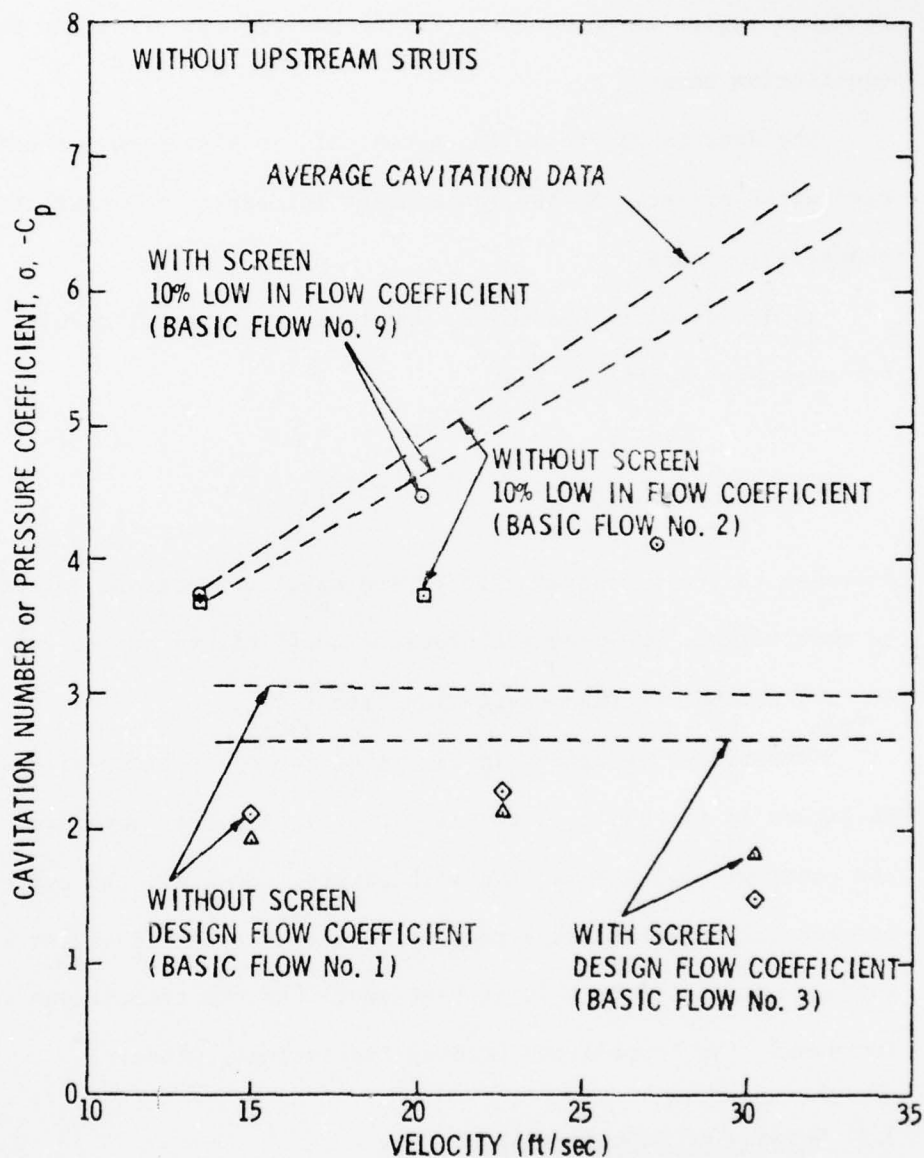


Figure 47. Comparison Between Static Pressure Coefficients at End of Rotor Cap with Cavitation Data for Several Basic Flows without Struts

Ap-A064 708

PENNSYLVANIA STATE UNIV UNIVERSITY PARK APPLIED RESE--ETC F/G 20/4
SECONDARY-FLOW-RELATED VORTEX CAVITATION.(U)

JUL 78 M L BILLET

N00024-79-C-6043

UNCLASSIFIED

ARL/PSU/TM-78-189

NL

2 of 3
AD
A064708





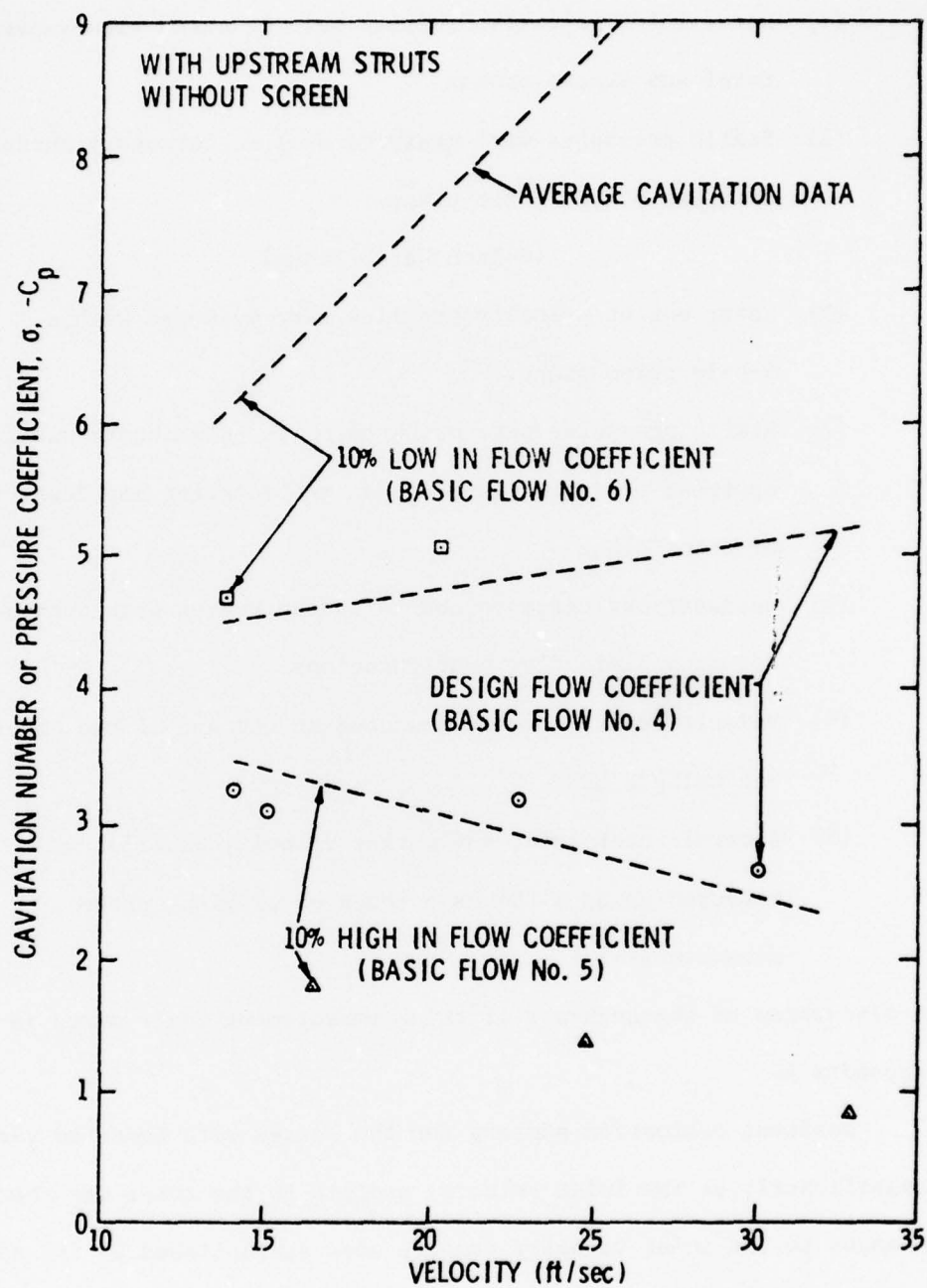


Figure 48. Comparison Between Static Pressure Coefficients at End of Rotor Cap with Cavitation Data for Several Basic Flows without Struts

48-Inch Wind Tunnel

- (1) Rotor inlet velocity profiles were measured with separate total and static probes.
- (2) Static pressures were measured on the stationary surface upstream of the rotor plane.

48-Inch Water Tunnel

- (1) Rotor outlet velocity profiles were measured with a 5-hole prism probe.
- (2) Static pressures were measured on the stationary surface upstream of rotor plane and on the rotating cap downstream of rotor plane.
- (3) Desinent cavitation numbers for the vortex were obtained for many basic flow configurations.
- (4) Velocity profiles were measured at the end of the rotor cap using a LDA.
- (5) Several rotor inlet and outlet velocity profiles were measured using a LDA as a check on previous probe measurements.

A discussion of the accuracy of these measurement instruments is given in Appendix A.

Desinent cavitation numbers for the vortex were found to vary significantly as the inlet velocity profile to the rotor was changed. Changes to the inlet velocity profile were accomplished by (1) adding a screen to the upstream surface, (2) adding upstream struts to the surface, (3) operating the rotor at different flow coefficients, and (4) varying the free stream velocity for constant flow coefficient. Each variation in

inlet velocity profile at a constant Reynolds number was given a Basic Flow Number.

An analysis of the inlet velocity profile data shown in Figures 6 through 10 shows that the largest changes in velocity occur near the rotor inner wall. At a position of $Y/R_R = 0.04$ near the rotor inner wall, operating 10% low in flow coefficient (Basic Flow No. 2) gives an increase of 12% in velocity from Basic Flow No. 1, adding a screen (Basic Flow No. 3) gives a decrease of 5% in velocity from Basic Flow No. 1, and adding struts (Basic Flow No. 4) gives an increase of 10% in velocity from Basic Flow No. 1. At a position of $Y/R_R = 0.40$ near the rotor mid-radius, Basic Flow No. 2 shows a 4% increase, Basic Flow No. 3 shows a 1% decrease, and Basic Flow No. 4 shows a 2% decrease in velocity from that for Basic Flow No. 1.

A comparison between the inlet velocity data and the critical cavitation data given in Figures 42 through 46 shows large changes in cavitation number for small inlet velocity changes. After taking the average of the cavitation data at each flow condition, an average cavitation number change per configuration can be made. This change gives the mean effect of variation in inlet flow. The mean effect of operating 10% low in flow coefficient is to increase the cavitation number by 46%, the mean effect of adding a screen is to decrease the cavitation index by 10%, and the mean effect of adding struts is to increase the cavitation number by 61%. The changes in inlet velocity near the inner wall are less than 12% as discussed in the previous paragraph.

The measurements made near the end of the rotor cap show that the structure of the vortex is formed along the inner wall. No single experimental curve clearly defines how this vortex develops. However,

comparisons of experimental data do give insight into the formation of the vortex.

If one assumes that all of the vorticity associated with the vortex is in the vortex core, the $C_{P_{min}}$ associated with this vortex is proportional to the square of the maximum tangential velocity located at the core radius (r_c) of the vortex. A comparison of Basic Flow No. 3 shown in Figure 30 to Basic Flow No. 1 shown in Figure 28 gives a decrease of 12% in absolute pressure coefficient. This compares favorably to a decrease of 10% in cavitation number. However, this comparison is the only one which correlates with cavitation number. As an example, a comparison between Basic Flow No. 4 shown in Figure 31 and Basic Flow No. 1 shown in Figure 28 shows a decrease in velocity at the core radii but the corresponding cavitation data give a 61% increase. In addition, the comparisons between the measured pressure coefficients at the end of the cap and the average cavitation data were poor. This is shown in Figures 47 and 48. The lack of direct correlation of cavitation data with measured velocity profiles and pressure coefficients implies that the minimum pressure of the vortex does not occur on the surface of the rotor cap.

A correlation between the change in inlet velocity profile and cavitation data and a lack of correlation between the measured vortex tangential velocity and cavitation data does indicate that secondary flows are important. Secondary flows generate additional streamwise vorticity near the inner wall when a boundary layer flow is turned by a rotor. This vorticity will induce an additional component of tangential velocity downstream of the rotor plane. Whether or not the influence of this additional streamwise vorticity on the tangential velocity is

completed at the end of the rotor cap is not important. The important fact is that this vorticity will change the net circulation near the inner wall.

If this secondary vorticity is an important part of the net circulation associated with the vortex, then the vortex core measured at the end of the rotor cap should be proportional to the distance in the normal direction from the surface over which the inlet velocity profile is important. In addition, the vortex core should be inversely proportional to the minimum pressure coefficient. The average measured vortex size can be obtained from Figures 28 through 34. Operating 10% low in flow coefficient (Basic Flow No. 2) gives a decrease of 28% in core radius from Basic Flow No. 1, adding a screen (Basic Flow No. 3) gives an increase of 5% in core radius from Basic Flow No. 1, and adding struts (Basic Flow No. 4) gives a decrease of 42% in core radius from Basic Flow No. 1. These results correlate the trends in cavitation data.

There are two possible flow parameters which control the core radius of the vortex. The first of these is a boundary layer parameter, such as momentum thickness. The other one is the amount of passage vorticity which exists near the inner wall of the rotor.

The boundary layer results for the rotor inlet velocity data are given in Table 2. These calculations show that operating 10% low in flow coefficient gives a decrease of 8% in momentum thickness from Basic Flow No. 1, adding a screen gives an increase of 15% momentum thickness, and adding struts gives an increase of 8% in momentum thickness. These results do not correlate the trends in cavitation data.

4. THEORETICAL ANALYSIS OF FLOW FIELD

4.1 Introduction

The experimental investigation shows that the structure of the vortex is formed along the inner wall. Two major conclusions can be made about the vortex. Firstly, the critical cavitation number of the vortex depends on the inlet velocity gradient near the inner wall. Secondly, the vortex core radius does not directly correlate with any boundary layer parameter of the inlet velocity profile.

In addition, the lack of correlation between the measured minimum pressure coefficients on the surface of the rotor cap and the cavitation data indicates that either the true minimum pressure associated with the vortex is not on the rotor cap or vortex breakdown occurred before the end of the rotor cap. In either case, it appears that the flow at the rotor exit is a better indicator of the vortex behavior than at the end of the rotor cap.

The calculation of the flow field near the inner wall of the rotor is a difficult problem. Assuming that the flow does not separate along the inner wall, the flow field near the inner wall depends upon the potential flow effects and viscous flow effects with the addition of the blade to blade secondary vorticity effects. For simplicity in the calculation of the flow field, the potential flow effects are the axisymmetric flow analysis obtained from the streamline curvature equations. This is referred to as the primary flow. The blade to blade secondary vorticity analysis is referred to as the secondary flow. Although viscous effects generate the inlet velocity profile to the rotor, no viscous effects are included in the calculation of the primary or secondary flow through the

rotor. The final flow field analysis through the rotor requires a coupling of the primary and secondary flows.

In order to calculate the secondary flow, a reasonable estimate of the streamlines near the inner wall is necessary. An approximate method has been developed to calculate these mean streamlines. This flow field is assumed to be axisymmetric, inviscid, and incompressible. The boundary conditions for the primary flow calculation are: (1) the flow outlet angles, (2) the velocity profile far upstream of the rotor plane, and (3) the bounding streamlines of the flow. The flow outlet angles are obtained from the blade angles of the rotor and a deviation angle. A schematic of the boundary conditions is shown in Figure 49.

This last boundary condition is the most difficult to define. The open rotor is unique because of the uncertainty of the bounding stream surface of the flow field. The flow field lacks a well-defined boundary, such as the walls of a turbine or compressor. For this reason, the flow field for the open rotor is considered to be a region constrained within a potential flow stream tube. The bounding stream surface of this stream tube is actually located infinitely far from the rotor; however, it is assumed that there is a finite distance beyond which the flow field is relatively unaffected by the presence of the rotor. This distance is assumed to be at least eight times the rotor radius. This stream surface located by this distance will serve as a flow boundary. In this manner, the bounding stream tube becomes analogous to the compressor and turbine walls.

It is important to realize that these boundary conditions imply a solution of the direct turbomachinery problem and not the indirect or design turbomachinery problem. For the direct problem, a rotor

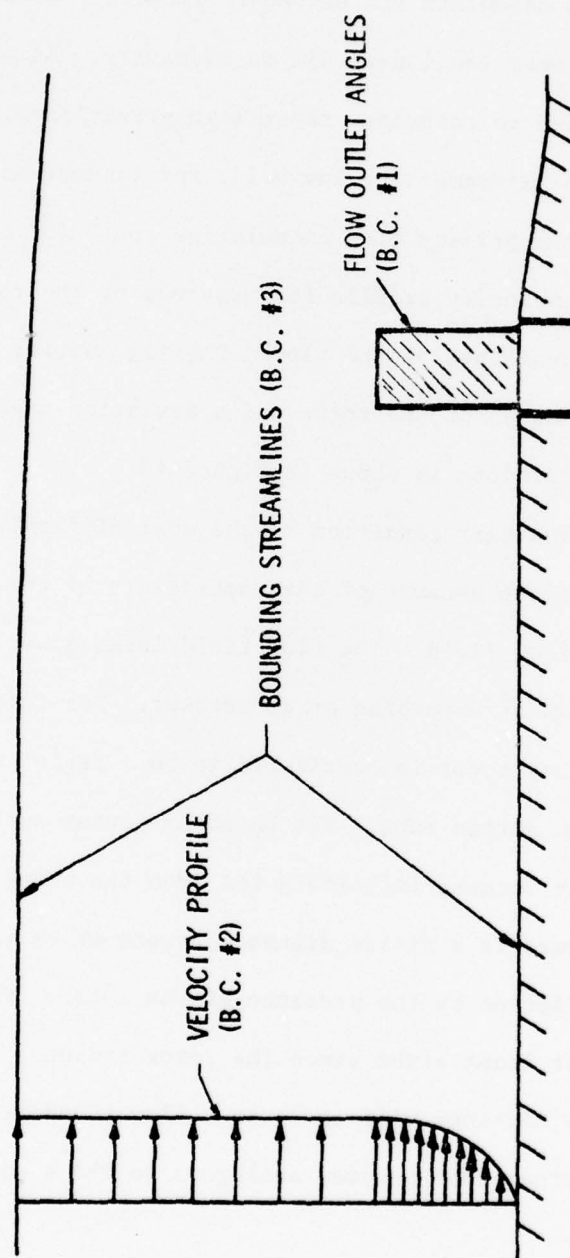


Figure 49. Schematic of Boundary Conditions

configuration is specified and the performance for any given initial condition is to be calculated. Thus, the flow outlet angles are specified instead of the tangential velocity (V_θ).

The equations which are commonly applied to calculate the flow field in an axisymmetric turbomachine are solved by use of the so-called streamline curvature method. This method has been used for some time for the design and analysis of various types of turbomachines. As described by Novak [34], Frost [35], and Davis [36], this system of equations has been successfully applied for the indirect analysis of compressors and turbines. Also, McBride [37] has applied this streamline curvature method to the indirect problem of an open hydrodynamic rotor.

In this chapter, a method to calculate the final mean streamlines for the direct problem is discussed. The method uses the streamline curvature equations to establish the flow field from the boundary conditions. The equations used for secondary flow calculations are discussed.

4.2 Primary Flow Field

4.2.1 Discussion of Calculation Procedure. A schematic of the calculation procedure for the final flow field is given in Figure 50. This outlines the iterative procedure for the calculation of the final flow field and indicates where secondary flow calculations are employed.

The initial conditions (Step 1) to the solution of the direct problem are (1) bounding stream tube and (2) velocity profile in rotor plane without rotor. With this information, the initial streamlines without rotor can be calculated (Step 2). The result of this calculation is the boundary condition of an initial velocity-energy profile at a station far upstream of the rotor plane.

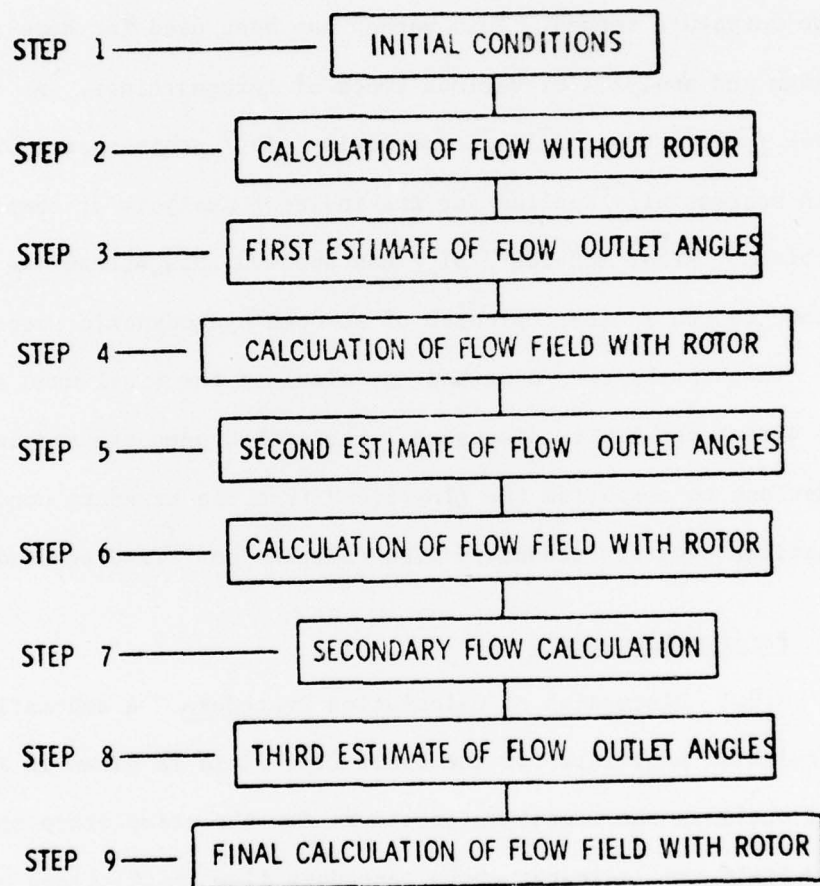


Figure 50. Outline of Calculation Procedure

Knowing the blade angles, the first estimate of the flow outlet angles (Step 3) can be calculated. These flow outlet angles depend on the blade angles (β_2) and deviation angle (δ). The deviation angle correlation developed by Howell [38] is initially applied. This relationship considers only thin blade sections and assumes that each blade section operates near design incidence. As shown in Figure 49, all of the boundary conditions are now known and the flow field can be solved with the rotor included (Step 4).

Once a convergent solution is obtained for the flow field using Howell's deviation rule (Step 4), the axial velocity distributions are known whereby the inlet angles can be estimated in addition to the acceleration through the rotor. Now a second estimate of the flow outlet angles (Step 5) can be made. For this deviation angle, the effects of acceleration ($\Delta\delta'$), blade camber (δ_o), and blade thickness ($\Delta\delta^*$) are calculated separately. For the calculation of the deviation term due to axial acceleration through the rotor, an equation developed by Lakshminarayana [39] is applied. For the calculation of deviation terms due to camber and thickness effects, the data collected by Lieblein [40] are used. The result is an improved outlet flow angle profile which can be used to again calculate the flow field (Step 6).

The convergent solution of the flow field (Step 6) is then used to solve the secondary vorticity equations (Step 7) and to determine a deviation term ($\Delta\delta_s$) which is due to blade to blade secondary flows. The details of the secondary flow calculations are described in Section 4.3. An improved outlet flow angle profile (Step 8) is obtained by adding this secondary flow term to the deviation terms previously calculated to obtain

$$\beta_2^* = \beta_2 - \Delta\delta' + \Delta\delta^* + \delta_o + \Delta\delta_s, \quad (21)$$

where β_2^* is the outlet flow angle and β_2 is the blade outlet angle. This outlet flow angle profile is then used as a boundary condition in the calculation of the final flow field (Step 9).

Finally, all of the deviation angle calculations are checked based on the flow field calculated in Step 9. If the angles did not change significantly, then the results obtained in Step 9 are the final flow field. If the angles were different, then these new angles are used to again calculate the final flow field (Step 9).

4.2.2 Streamline Curvature Method. The major equations used in the streamline curvature method of analysis are derived from the principles of conservation of mass, momentum, and total energy. In this analysis, the fluid is assumed to be incompressible, inviscid, and steady. Because the flow field is axisymmetric, it is necessary to use only two components of velocity. One component of velocity (the meridional velocity (V_m)) is tangent to the streamline and is projected onto the meridional plane. This component is related to the axial velocity by the cosine of the streamline angle (ϕ). The second component of velocity is called the tangential velocity (V_θ) and is in the circumferential direction which is perpendicular to the meridional plane.

The resultant equations allow for streamline curvature and for vorticity in the flow. However, it is important to realize that the solution to the flow field does not contain all of the vorticity. In particular, only the circumferential vorticity is totally included. The other components of vorticity contain derivatives with respect to the circumferential direction which are assumed to be zero with an

axisymmetric flow analysis. As discussed by Hawthorne and Novak [19], the neglected vorticity terms can be related to the secondary flows that occur in the blade passage.

The set of equations used for this streamline curvature method are as follows:

r-momentum equation --

$$\frac{1}{\rho} \frac{\partial P}{\partial r} = \frac{V_{\theta}^2}{r} + V_m^2 \left\{ \frac{\cos \phi}{R_m} - \frac{\sin \phi}{V_m} \frac{\partial V_m}{\partial m} \right\} , \quad (22)$$

θ -momentum equation --

$$\frac{\partial (rV_{\theta})}{\partial \theta} = 0 , \quad (23)$$

energy equation --

$$\frac{\partial P_o}{\partial m} = 0 \text{ {except across rotor plane}} , \quad (24)$$

and continuity equation --

$$2\pi \int_{r_1}^{r_2} V_m \cos \phi \, r \, dr = \text{constant} . \quad (25)$$

In these equations, R_m is the radius of curvature of the streamlines in the meridional plane and ϕ is the streamline angle with respect to the axial direction.

In Equation (22), there are three contributing factors in the development of the radial pressure gradient. The first term is directly related to the centrifugal force which the fluid experiences upon passing

through the rotor. The second term is due to a moving fluid particle being subjected to the streamline curvature in the meridional plane. The magnitude of this term depends directly on the radius of curvature of the streamline. The third term is due to the convective acceleration as the flow area either converges or diverges. The combination of these three terms defines the radial pressure gradient.

The computational procedure using the four equations is an iterative one. Initially, the velocity distribution at the reference station far upstream of rotor is transferred to the downstream flow by using the continuity equation. At the rotor exit plane, the tangential velocity profile is related to the axial velocity by

$$V_{\theta 2} = \Omega r - V_{x 2} \tan \beta_2^* \quad , \quad (26)$$

where β_2^* is the flow outlet angle. Now, the principle of constant angular momentum allows for the transfer of tangential velocity downstream of the rotor. Finally, the static pressure can be calculated along the streamlines using the radial pressure equation and a new meridional velocity profile is calculated by using this pressure. This velocity-pressure coupling is repeated until the streamlines are located such that the flow simultaneously satisfies continuity, conservation of momentum, and conservation of total energy.

4.2.3 Estimation of Rotor Outlet Angles. The accuracy of the calculated velocity profiles to experimental data depends primarily upon the prediction of the flow outlet angles (β_2^*) used in Equation (26). The flow outlet angle (β_2^*) is shown in Figure 51. This angle is a combination of blade geometry and a deviation angle. The blade angle

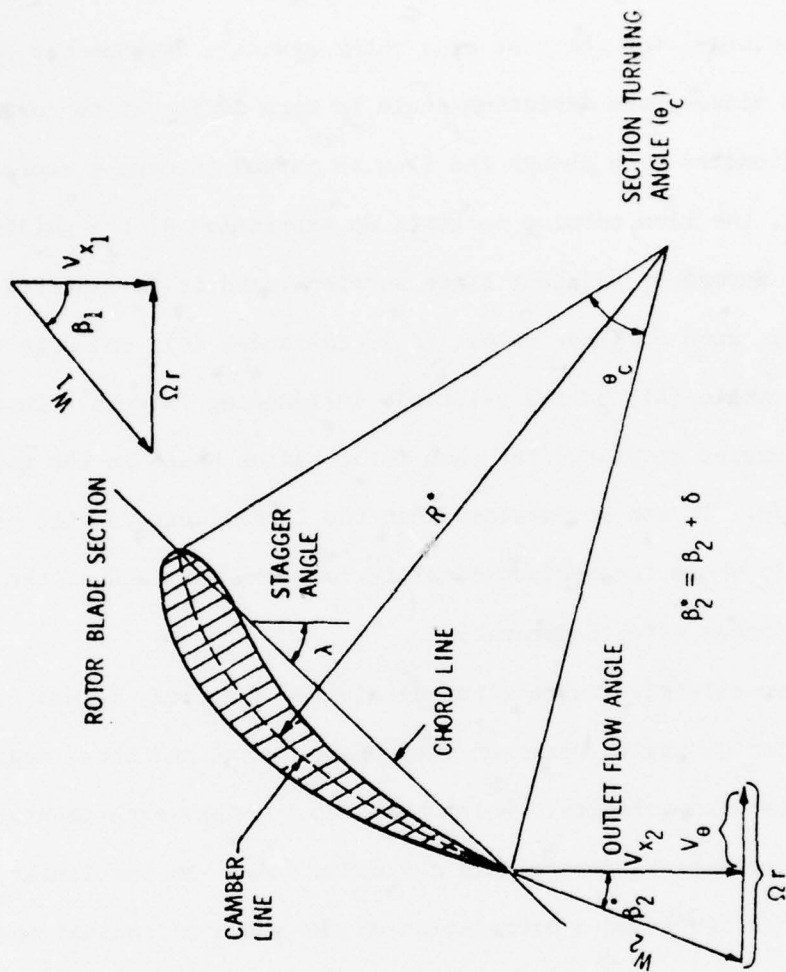


Figure 51. Definition of Blade Angles

(β_2) is defined as the angle between the tangent to the blade section camber line at the trailing edge and the exit axial direction.

The correct determination of the deviation angle presents a problem. In particular, for the case of a rotor having a low hub-tip ratio and twisted blades, the deviation angle is more difficult to correlate with blade geometry even though the flow is turned through a small angle. However, the flow turning is still an expression of the guidance of the passage formed by adjacent blade sections, and it is expected that the geometry, such as blade camber (θ_c), thickness (t), solidity (c/s), and stagger angle (λ), be the principle influencing factors. Thus, deviation angles can be estimated for each rotor radius based on the geometry of the blade. It can be expected that the largest errors will occur at the blade tip where three-dimensional factors dominate and at the inner wall where viscous effects dominate.

From extensive cascade potential-flow theories, it was found that the deviation angle increases with blade camber and chord angle and decreases with solidity. Using this result, many experimentors have correlated data to determine a deviation rule. In particular, Howell [38] has developed a correlation on the basis of nominal operating conditions. This condition pertains to a deflection of the flow which is 80% of its maximum stalling deflection. The deviation angle is defined for each blade section as

$$\delta_H = \frac{0.23(\theta_c)(s/c)^{1/2}(2a/c)^2}{1.0 - (0.1/50)(\theta_c)(s/c)^{1/2}}, \quad (27)$$

where θ_c is the section turning angle, s/c is the space-to-chord ratio, and a/c is the distance from the section leading edge to the point of maximum camber divided by the section chord length.

Equation (27) is used in the first estimate of flow outlet angles (Step 4) in the calculation of the flow field. It is important to note that this deviation correlation assumes thin blades and that each blade section operates near design incidence. Once a converged solution is obtained for the flow field using Howell's deviation (Step 5), the inlet and outlet axial velocity distributions are estimated. Now, the deviation angle can be recalculated based on the effects of axial acceleration ($\Delta\delta'$), camber (δ_o), blade thickness ($\Delta\delta^*$), and secondary flows ($\Delta\delta_s$). Therefore, a second order deviation angle can be expressed as

$$\delta = \delta_o + \Delta\delta^* - \Delta\delta' + \Delta\delta_s \quad (28)$$

The deviation term due to acceleration in the blade passage is given by Lakshminarayana [39] as

$$\Delta\delta' = \frac{AVR-1.0}{AVR} \left\{ \frac{\pi k(c/s) \left(\frac{G}{c} + \frac{\alpha^*}{4} \right) \cos\left(\frac{\beta_1 + \beta_2^*}{2}\right) ((AVR+1)^2 - 4)}{AVR-1.0} \right. \\ \left. \left[8 + \pi k(c/s) \left(\frac{\alpha^*}{4} + \frac{G}{c} \right) \cos\left(\frac{\beta_1 + \beta_2^*}{2}\right) ((AVR+1)\tan\beta_2^* + 2\tan\beta_1^*) \right] \right. \\ \left. - \frac{2\pi k(c/s)\tan\beta_1}{AVR \cos\left(\frac{\beta_1 + \beta_2^*}{2}\right) \sec^2\beta_1} \right\} \\ \left[8 + \pi k(c/s) \left(\frac{\alpha^*}{4} + \frac{G}{c} \right) \cos\left(\frac{\beta_1 + \beta_2^*}{2}\right) ((AVR+1)\tan\beta_2^* + 2\tan\beta_1^*) \right]$$

$$+ \tan \beta_2^* \left\{ \cos^2 \beta_2^* \right\}, \quad (29)$$

where AVR is the axial velocity ratio (V_{x2}/V_{x1}), k is the cascade influence coefficient, G/c is the ratio of the distance from the chord line to the maximum camber point of the section to chord length, β_1 and β_2^* are the inlet and outlet flow angles, respectively, and α^* is defined as the difference between the inlet flow angle (β_1) and the section stagger angle (λ). This relationship is valid for small changes in AVR and for small turning angles. Perhaps most important, the deviation angle due to axial acceleration in the flow always reduces the total deviation.

The deviation due to thickness and camber is given by empirical data which have been collected by Lieblein [40]. The thickness deviation is calculated from

$$\Delta \delta^* = (K_\delta)_{sh} \cdot (K_\delta)_t \cdot (\delta_o^o)_{10}, \quad (30)$$

where $(\delta_o^o)_{10}$ represents the basic variation for the 10% thick 65-series thickness distribution, $(K_\delta)_{sh}$ represents any correction necessary for a blade shape with a thickness distribution different from that of the 65-series blade, and $(K_\delta)_t$ represents any correction necessary for maximum blade thickness other than 10%. The value of $(K_\delta)_{sh}$ can range from 1.1 to 0.7; therefore, an average value of 0.9 is used for the rotor. Also, the other coefficients are determined from graphs of experimental data in Reference [40] knowing solidity and inlet flow angles.

The effect of camber on deviation is calculated by using

$$\delta_o = m \theta_c \quad , \quad (31)$$

where m is the slope of the deviation angle variation with camber angle (θ_c). Values of m can be determined from the figures given in Lieblein [40] by knowing the flow inlet angle and solidity. This slope is given for either circular-arc or parabolic-arc mean camber lines.

Equations (29), (30), and (31) are used for the second estimate of rotor outlet angles (Step 5). In order to use these deviation relationships the axial velocity through the rotor had to be estimated. This velocity estimation was accomplished by using Howell's correlation in the first calculation of the flow field.

The last deviation term to be considered is due to secondary flows. The effects of secondary flows are most dramatic near the rotor inner wall where the inlet velocity gradients are largest. Secondary flows produce a streamwise component of vorticity which is not taken into consideration by axisymmetric analysis.

The solution for the streamwise secondary vorticity involves the numerical solution of two equations which are discussed in the next section. After solving for the streamwise vorticity at the rotor exit plane, a secondary stream function is defined in this plane. The solution for the stream function gives perturbation velocities which are used to find a deviation angle ($\Delta\delta_s$).

4.3 Secondary Flow Field

4.3.1 Secondary Vorticity. In order to accomplish work in a rotor, angular momentum must be imparted to the fluid. The lifting action of the

rotor blades produces tangential pressure gradients. For the case of the rotor operating within a boundary layer, the pressure gradients are balanced by streamline curvature at a sufficient distance from the inner wall. Close to the inner wall, the velocities are much less than at the rotor tip. The fluid near the inner wall does not have sufficient momentum to balance the pressure gradients imposed by the flow. The result is a tangential component containing vorticity aligned in the streamwise direction. This additional streamwise vorticity causes a deviation in the outlet angles.

There are no simple techniques that accurately predict these inner wall velocity gradient effects for rotational flows. It is important to recognize that a satisfactory description of this boundary layer flow cannot come from refinements of the two-dimensional boundary layer theory, but rather from three-dimensional analysis. The reason is that boundary layer behavior in a rotor exhibits variations in its tangential direction. The occurrence of these secondary flows which are boundary layer flows having a component normal to the mainstream direction arise principally from blade to blade and radial pressure gradients. Similarity between the results of secondary flow analysis and the cross-flow in the outer part of a three-dimensional boundary layer has been established by Horlock [41].

The distributed passage secondary vorticity generated by turning a boundary layer flow is one of three possible types of secondary streamwise vorticity, which can occur near the inner wall of a rotor. As discussed by Hawthorne [42], three components of secondary vorticity are identified in the direction of flow at the exit of a blade row. These secondary sources of vorticity are usually regarded as a perturbation on the primary flow. They are (1) a distributed passage vorticity in the blade passage

which may result in the formation of the so-called passage vortex, (2) the trailing shed vorticity, and (3) the trailing filament vorticity. The latter two types of vorticity are due to the passage vortex and occur in the vortex sheet leaving the blade trailing edge. They lead to the formation of another vortex which is opposite in rotation to that of the passage vortex as shown in Figure 52. The trailing filament vorticity is caused by the stretching of the vortex filaments as they move over the surface of the blades. The last component of vorticity is the trailing shed vorticity which is caused by a change in circulation along the span of the blades.

Each of these vorticity components could be attributed to the existence of the wall boundary layer and not the change of the boundary layer due to viscous effects as flow passes through the rotor. Therefore, the primary assumption leading to the existing theoretical descriptions of secondary flows is that viscous effects produce a boundary layer on the inner wall upstream of the rotor. Whereas within the rotor, the imposed pressure gradients play the major role and viscosity has little effect in the resulting secondary flows. This assumption is characteristic of what is generally termed inviscid secondary flow analysis.

As shown in an analysis of secondary flows by Came and Marsh [43], the total strength of these three secondary components of streamwise vorticity is zero in the flow downstream of a many bladed cascade. However, this vorticity does have an effect on the flow field. The primary effect of this secondary vorticity is to cause a deviation in the flow outlet angle. This is due to the induced velocity field from the passage secondary vorticity. This deviation can be quite large when the inlet velocity gradient to the rotor is large or when the flow is turned

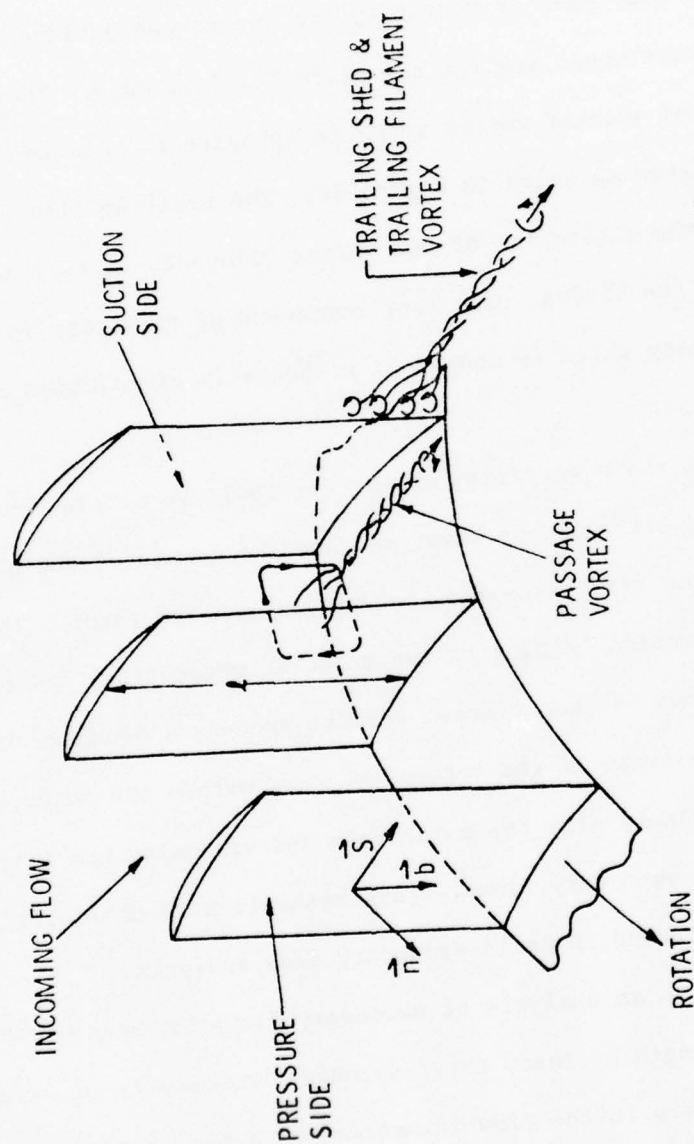


Figure 52. Schematic of Rotor Inner Wall Secondary Flows
(Lakshminarayana and Horlock [18])

through a large angle. The solution for this deviation must be consistent with the trailing vortex sheet, but the strength of this sheet does not need to be known.

Theoretical development of secondary flow equations begin with the fluid flow equations that govern the flow process. The equation of motion for incompressible flow with reference to axis rotating at constant angular velocity $(\vec{\Omega})$ is given in Greenspan [44] as

$$\vec{\xi} \times \vec{W} + 2\vec{\Omega} \times \vec{W} = -\nabla' \left(\frac{P}{\rho} \right) - \nabla' \left[\frac{W^2}{2} - \frac{1}{2} (\vec{\Omega} \times \vec{r}) \cdot (\vec{\Omega} \times \vec{r}) \right] - (\mu/\rho) \nabla' \times \nabla' \times \vec{W} \quad (32)$$

where the prime denotes differentiation with respect to the rotating frame $(\vec{\Omega})$, \vec{W} is the relative velocity, and $\vec{\xi}$ is the relative vorticity given by $\vec{\xi} = \nabla' \times \vec{W} = \vec{\omega} - 2\vec{\Omega}$. Taking the curl of Equation (32) gives the vorticity equation

$$(\vec{W} \cdot \nabla') \vec{\xi} = (\vec{\xi} \cdot \nabla') \vec{W} - 2\nabla' \times (\vec{\Omega} \times \vec{W}) + (\mu/\rho) \nabla'^2 \vec{\xi} \quad (33)$$

Expressions for the absolute secondary vorticity (ω) defined along a relative streamline valid for a rotor are obtained from Equation (33) by Lakshminarayana and Horlock [16]. The resultant equations are

$$\frac{\partial}{\partial s'} \left[\frac{\omega_{s'}}{W} \right] = \frac{2\omega_{n'}}{WR^*} + \frac{2\Omega_{b'} \omega_{n'}}{W^2} - \frac{2\Omega_{n'} \omega_{b'}}{W^2} + (\mu/\rho) \vec{s}' \cdot \frac{\nabla'^2 \vec{\xi}}{W^2} \quad (34)$$

and

$$\frac{\partial}{\partial n'} [\omega_{n'}, W] = \frac{W\omega_{b'}}{\tau} - \frac{W\omega_{n'}}{a_{b'}} \frac{\partial a_{b'}}{\partial s'} + (\mu/\rho) \vec{n}' \cdot \nabla'^2 \vec{\xi} \quad (35)$$

where as shown in Figure 53, \vec{s}' , \vec{n}' , \vec{b}' represent the natural coordinates for the relative flow, W is the relative velocity, ω_s , and ω_n , are absolute vorticity resolved along the relative streamline direction (\vec{s}') and the principal normal direction (\vec{n}'), $\vec{\Omega}$ is the rotation vector, and R^* is the radius of curvature of the relative streamline. In this relative coordinate system indicated by the primes, the streamwise direction (\vec{s}') is defined along the flow direction, the principal normal direction (\vec{n}') is defined toward the center of curvature of the streamlines, and the bi-normal direction (\vec{b}') is defined as $\vec{s}' \times \vec{n}' = \vec{b}'$. Additional definitions of the flow in the relative coordinate system are given in Reference [16].

The means by which the streamwise component of vorticity is produced in a relative flow are similar to those in a stationary system. However, it is important to note that additional secondary vorticity is generated when $\vec{\Omega} \times \vec{W}$ has a component in the relative streamwise direction. Rotation has no effect when the absolute vorticity vector lies in the s' - n' plane and the rotation ($\vec{\Omega}$) has no component in the bi-normal direction (\vec{b}').

The equations for secondary vorticity created in the passage, namely, Equations (34) and (35), are extremely difficult to apply because they are nonlinear partial differential equations. Therefore, some simplifying assumptions and specifications of the flow field must be made for this application. The basic flow parameters for this vortex problem are a thick boundary layer entering the rotor and the rotor operating at a flow coefficient less than 0.5. It is also important to note that the primary flow through the rotor is rotational.

In order to evaluate the relative importance of the terms that describe the passage secondary vorticity, the vorticity equations were

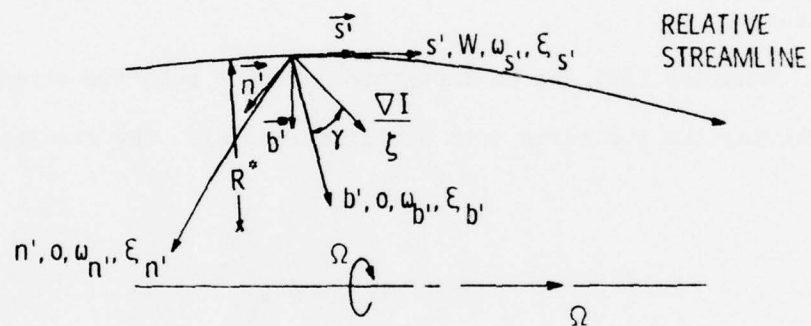


Figure 53. Notation for Rotating Coordinate System

first nondimensionalized. Then an order to magnitude evaluation was applied. The details of this process are given in Reference [45].

The resulting normal relative vorticity equation is

$$\frac{\partial}{\partial s'} (\omega_n, W) = - \frac{W \omega_n}{a_{b'}} \cdot \frac{\partial a_{b'}}{\partial s'}, \quad (36)$$

where $a_{b'}$ is the distance between neighboring streamlines in $\vec{b'}$ direction. Two assumptions applied in developing Equation (36) are (1) the ratio of boundary layer thickness to rotor tip radius is of order one and (2) the blade chord (c) is an order of magnitude less than the camber radius.

Equation (36) can be integrated along a relative streamline by combining the two terms into one differential. The result is

$$\omega_n = \omega_{n_1} \cdot \frac{W_1 a_{b_1}}{W a_{b'}}, \quad (37)$$

where the subscript 1 refers to the rotor inlet and unnumbered subscripts refer to any position along a streamline in the rotor. This simplified equation shows a dependence of the relative component of the normal vorticity on the variation of relative velocity (W) along a relative streamline, on the relative component of the absolute inlet normal vorticity (ω_{n_1}), and on the flow convergence-divergence in the bi-normal direction (a_{b_1}).

Equation (37) can be evaluated along a relative streamline if the streamline spacing ($a_{b'}$) in the bi-normal direction and the relative velocity along a relative streamline are known. These quantities can be

obtained from the primary flow analysis using the streamline curvature equations.

For some rotors having a high hub-to-tip ratio, the streamline spacing in the radial direction (a_b) remains constant, so that Equation (37) becomes

$$\omega_{n'} = \omega_{n'_1} \cdot \frac{W_1}{W} \quad (38)$$

This result relates the change in the relative component of the absolute normal vorticity ($\omega_{n'}$) to changes in the relative velocity (W). Also, assuming a weak shear flow so that the axial velocity remains constant gives

$$\omega_{n'} = \omega_{n'_1} \cdot \frac{\cos \beta_1}{\cos \beta} \quad (39)$$

These last two relationships are commonly used for secondary flow cascade theory.

The resulting streamwise vorticity equation is

$$\frac{\partial}{\partial s'} \left\{ \frac{\omega_{s'}}{W} \right\} = \frac{2\omega_{n'}}{WR^*} + \frac{2\Omega_{b'}\omega_{n'}}{W^2} - \frac{2\Omega_{n'}\omega_{b'}}{W^2} \quad (40)$$

The second term on the right-hand side of Equation (40) is due to curvature induced secondary vorticity. The third term is due to rotation induced secondary vorticity. The last term is important because $\Omega_{n'}$ is large because the flow coefficient is less than one. Integrating Equation (40) in the relative streamwise direction yields

$$\begin{aligned}
 \omega_{s_2}' = W_2 \int_1^2 \frac{2\omega_{n'}'}{WR^*} ds' + W_2 \int_1^2 \frac{2\Omega_{b'}'\omega_{n'}'}{W^2} ds' \\
 - W_2 \int_1^2 \frac{2\Omega_{n'}'\omega_{b'}'}{W^2} ds' + \omega_{s_1}' \left\{ \frac{W_2}{W_1} \right\} . \quad (41)
 \end{aligned}$$

It is important to note that the boundary layer thickness is the same order as the rotor tip radius and much larger than the blade chord. The velocity gradients for these conditions are not as large as would be the case if the boundary layer thickness would be much less than the rotor tip radius. Therefore, stream surfaces in the blade passage will not be significantly distorted so that Bernoulli's surface rotation (see Reference [46]) is not important.

If the relative streamlines and the absolute vortex lines lie on cylindrical surfaces ($\omega_b = 0$) and the rotation vector ($\vec{\Omega}$) is parallel to the axis of the cylindrical surfaces, then Equation (41) would become

$$\frac{\omega_{s_2}'}{W_2} - \frac{\omega_{s_1}'}{W_1} = \int_1^2 \frac{2\omega_{n'}'}{WR^*} ds' . \quad (42)$$

This relationship is commonly used in most cascade flow calculations and is the equivalent of an equation developed by Squire and Winter [47] but with a relative reference frame.

More comparisons between the equations for the secondary vorticity in a rotating reference frame and cascade secondary vorticity are discussed in Reference [45].

The solution for the absolute streamwise vorticity defined along a relative streamline can be calculated using Equations (37) and (41). However, the primary flow field must be initially calculated.

From the solution of the primary flow field, the relative velocity (W), the streamline spacing in the b' -direction ($a_{b'}$), the rotation (Ω), the flow turning angle ($\beta_1 - \beta_2^*$), and the inlet absolute normal velocity (ω_{n1}) are known for a mean relative streamline.

As shown in Figure 54, these quantities can be divided into their components and used in the secondary flow equations. A mean radius of curvature (R^*) for the blade sections defined by a mean relative streamline is calculated from

$$R^* = \frac{c}{(\beta_1 - \beta_2^*)} \quad (43)$$

for small turning angles ($\beta_1 - \beta_2^*$). Also, the component of absolute vorticity defined in the relative bi-normal direction ($\omega_{b'}$) is assumed to be proportional to

$$\omega_{b'} \propto \frac{W}{R^*} \quad (44)$$

for the rotor considered.

4.3.2 Secondary Velocities. Secondary motions are induced by the distributed secondary vorticity in the flow between the blades. With large blade turning angles, the secondary motions in the blade passage are masked by large spanwise flows associated with changes in axial velocity profile referred to as displacement effects. Hawthorne and Armstrong [48] have developed an analysis for predicting these

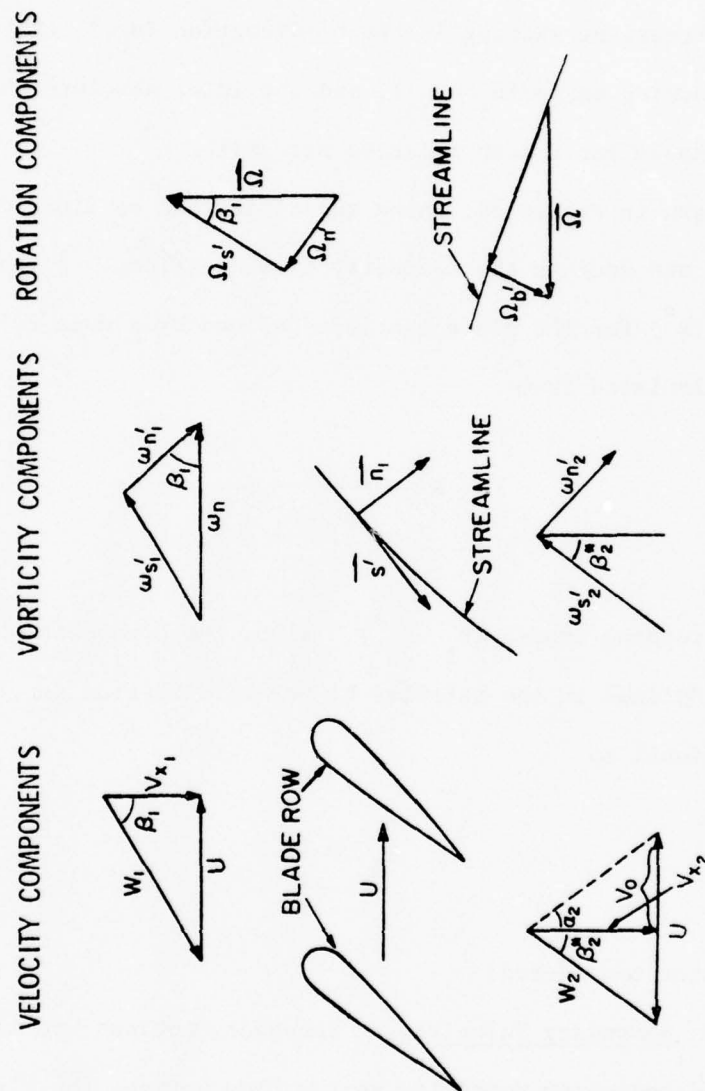


Figure 54. Schematic of Flow Parameters in Rotating Coordinate System

displacement effects which reduce the secondary motions. With small blade turning angles, the secondary motion largely determines the variation in outlet angle downstream. For most rotor design, the turning near the inner wall is small where secondary motions are the largest.

Formulas for calculating the two-dimensional solution for the secondary motion in blade passages have been given by Hawthorne [49], Hawthorne and Novak [19], and Dixon [50]. The secondary motion in terms of velocities (u , v , and w) is assumed to be induced by the streamwise secondary vorticity ($\omega_{s2}, -\omega_{s1}$) at the trailing edge plane of the rotor. This streamwise secondary vorticity was calculated along a mean streamline and is a function of radius only. It is important to note that the normal component of vorticity (ω_n) is accounted for in the axisymmetric flow analysis.

The effect of the streamwise component of secondary vorticity ($\omega_{s2}, -\omega_{s1}$) within the blade passage is similar to that obtained in the flow through a duct bend (Hawthorne [51], Eichenberger [52], Detra [53]); however, there is the difficulty of devising a reasonable approximate method of satisfying the Kutta-Joukowski condition at the trailing edge.

The method developed by Hawthorne and Novak [19] assumes that the flow is contained in a duct defined by the blades and streamlines of the primary flow leaving the trailing edge of each blade. In this trailing edge plane, the secondary streamwise vorticity is divided into a tangential and axial component. The former term, namely, $(\omega_{s2}, -\omega_{s1}) \sin \beta^*$, causes a radial gradient of axial velocity and the latter leads to an equation for a stream function describing the radial and tangential velocities in the trailing edge plane (r, θ).

Referring to Figure 55, the velocity perturbations induced by $(\omega_{s_2}, -\omega_{s_1})$ have components u, v, w in the r, θ, x directions, respectively. The secondary streamwise vorticity as calculated from Equations (37) and (41) and the relative velocity (W) are only a function of radius. The components of the streamwise vorticity are

$$(\omega_{s_2}, -\omega_{s_1}) \sin \beta_2^* = \omega_{\theta_2} = -\frac{dw}{dr} \quad (45)$$

and

$$(\omega_{s_2}, -\omega_{s_1}) \cos \beta_2^* = \omega_{x_2} = \frac{1}{r} \left[\frac{\partial(rv)}{\partial r} - \frac{\partial(u)}{\partial \theta} \right], \quad (46)$$

where w is only a function of radius and u is not a function of x .

Equation (45) can be integrated to

$$w = - \int_{R_i}^{R_R} (\omega_{s_2}, -\omega_{s_1}) \sin \beta_2^* dr, \quad (47)$$

where the constant of integration is obtained from continuity. The net mass flow through the exit plane due to the secondary velocity (w) must be zero. Therefore, the boundary condition for Equation (47) is

$$2\pi \int_{R_i}^{R_R} wr dr = 0. \quad (48)$$

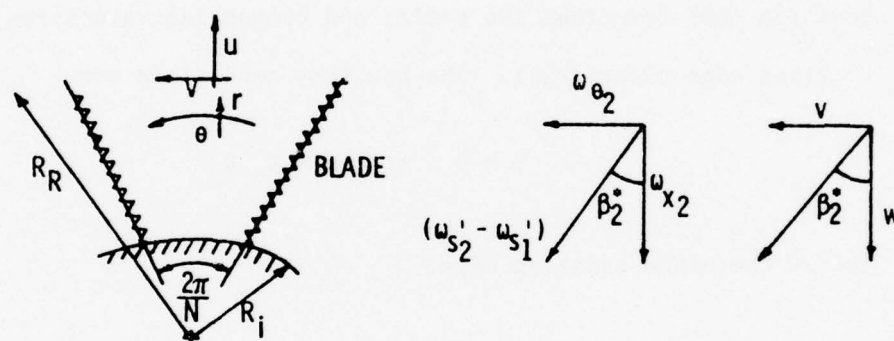


Figure 55. Schematic of Secondary Velocity Flow Field

Defining a secondary stream function (Ψ) as

$$u = \frac{1}{r} \frac{\partial \Psi}{\partial \theta} \quad \text{and} \quad v = - \frac{\partial \Psi}{\partial r} \quad , \quad (49)$$

the continuity equation and the x-direction vorticity equation can be combined into a stream function equation. The result is

$$\frac{\partial^2 \Psi}{\partial r^2} + \frac{1}{r} \frac{\partial \Psi}{\partial r} + \frac{1}{r^2} \frac{\partial^2 \Psi}{\partial \theta^2} = - (\omega_{s_2}, -\omega_{s_1}) \cos \beta_2^* \quad . \quad (50)$$

Equation (50) describes the radial and tangential velocities in the trailing edge plane (r, θ). The boundary conditions are

$$\Psi = 0 \quad \text{at} \quad r = R_i, R_R \quad (51)$$

and at the blade trailing edge,

$$w \sin \beta_2^* = v \cos \beta_2^*$$

or

$$\frac{\partial \Psi}{\partial r} = - w \tan \beta_2^* = f(r) \quad (52)$$

at

$$\theta = 0 \quad , \quad 2\pi/N \quad , \quad 4\pi/N \quad \dots \quad .$$

Hawthorne and Novak [19] redefine a new stream function which includes the boundary condition of Equation (52). The result is that the stream function will now be zero everywhere on the boundary. The stream function is defined as

$$\Psi(r, \theta) = \Psi^*(r, \theta) + \bar{\Psi}(r) \quad , \quad (53)$$

where $\Psi^* = 0$ at $r = R_i, R_R$ and at $\theta = 0, 2\pi/N, 4\pi/N, \dots$.

Equation (50) becomes

$$\begin{aligned} \frac{\partial^2 \Psi^*}{\partial r^2} + \frac{1}{r} \frac{\partial \Psi^*}{\partial r} + \frac{1}{r^2} \frac{\partial^2 \Psi^*}{\partial \theta^2} &= \frac{w}{r} \frac{d}{dr} (r \tan \beta_2^*) \\ &+ \tan \beta_2^* \frac{dw}{dr} \\ &- (\omega_{s_2}, -\omega_{s_1}) \cos \beta_2^* \quad . \end{aligned} \quad (54)$$

Finally, Equation (45) can be used in Equation (54) giving

$$\nabla^2 \Psi^* = \frac{w}{r} \frac{d}{dr} (r \tan \beta_2^*) - (\omega_{s_2}, -\omega_{s_1}) \sec \beta_2^* \quad . \quad (55)$$

The right-hand side of Equation (55) is a function of r only. Equation (55) is identical to that obtained by Hawthorne and Novak [19] except the equation is for a relative reference frame.

In a discussion of a paper, Hawthorne [54] gives the transformation of Stoke's equation from r, θ coordinates to z, y coordinates. The transformation is

$$r/R_i = e^{\left(\frac{2\pi z}{N}\right)} \quad (56a)$$

and

$$\theta = \frac{2\pi y}{N} \quad . \quad (56b)$$

Substituting Equation (56) into the stream function equation gives

$$\frac{\partial^2 \psi^*}{\partial z^2} + \frac{\partial^2 \psi^*}{\partial y^2} = \left(\frac{2\pi r}{N}\right)^2 F(r) = G(z) \quad , \quad (57)$$

with the boundary conditions of $\psi = 0$ at $y = 0$ and $y = 1$ and at $z = 0$ and $z = \ell$. The quantity ℓ is defined as

$$\ell = \left(\frac{N}{2\pi}\right) \ln\left(\frac{R_i}{R_R}\right) \quad .$$

The solution of Equation (57) must be periodic so that

$$G(z) = G(z) \sum_{1,3,5}^{\infty} \frac{4}{n\pi} \sin n\pi y \quad (58)$$

and is in the form

$$\psi^* = \sum_{1,3,5}^{\infty} \psi_n(z) \sin n\pi y \quad . \quad (59)$$

A general solution of Equation (57) in the form of Equation (59) has been obtained by Hawthorne [54] using the method of variation of parameters. The solution for $\psi_n(z)$ is

$$\begin{aligned} \psi_n(z) = & -\frac{4/(n\pi)^2}{\sinh(n\pi\ell)} \left[\sinh(n\pi z) \int_z^{\ell} G(t) \sinh(n\pi(\ell-t)) dt \right. \\ & \left. + \sinh n\pi(\ell-z) \int_0^z G(t) \sinh(n\pi t) dt \right] \quad , \quad (60) \end{aligned}$$

and for $\Psi'_n(z)$ is

$$\frac{d\Psi'_n(z)}{dz} = \frac{4/n\pi}{\sinh(n\pi\ell)} \left[\cosh(n\pi(\ell-z)) \int_0^z G(t) \sinh(n\pi t) dt - \cosh(n\pi z) \int_z^\ell G(t) \sinh(n\pi(\ell-t)) dt \right] \quad (61)$$

A mean deviation angle ($\Delta\delta_s$) due to secondary flows can be calculated for any radius. The mean deviation angle is defined as

$$\Delta\delta_s = \frac{\bar{v} \cos^2 \beta^* - w \sin^2 \beta^*}{V_x \sec^2 \beta^*} \quad (62)$$

where

$$\bar{v} = N/2\pi \int_0^{2\pi/N} v \, d\theta \quad (63)$$

Using Equations (49), (52), and (53), Equation (62) becomes

$$\Delta\delta_s = - \frac{N \cos^2 \beta^*}{2\pi V_x} \int_0^{2\pi/N} \frac{\partial \Psi^*}{\partial r} d\theta \quad (64)$$

In terms of the transformed z, y coordinates, Equation (64) can be written as

$$\Delta\delta_s = - \frac{N \cos^2 \beta}{\pi^2 V_x R_i} \cdot e^{-\frac{2\pi z}{N}} \cdot \sum_{n=1,3,5,\dots}^{\infty} \frac{1}{n} \frac{d\psi_n(z)}{dz} \quad (65)$$

5. CALCULATION OF FLOW FIELD AND VORTEX PARAMETERS

5.1 Calculation of Final Flow Field

5.1.1 Flow Field for Basic Flow No. 1. The case of the rotor operating near design (Basic Flow No. 1) was calculated initially in order to obtain some general results about the influence of the deviation angle on the flow field. For this case, the rotor operated within an axisymmetric boundary layer created by an upstream surface. The steps in the calculation procedure are listed in Figure 50.

The measured velocity profile in the rotor plane without the rotor was extended upstream by the streamline curvature method (Step 2) in order to obtain a velocity profile far upstream of the rotor. This upstream profile is needed as a boundary condition of the flow field. A comparison between the measured profile in the rotor plane and a profile obtained by projecting the upstream profile to the rotor plane using the streamline curvature method is shown in Figure 56.

The theoretical design circulation distribution for the rotor is shown in Figure 57. Most of the loading occurs near the mid-radius where the camber angles are the largest. The stagger angles are high as a result of the design flow coefficient being less than one. The blade sections are thin except near the inner wall. The blade outlet angles (β_2) were determined from the blade geometry by using

$$\beta_2 = \lambda - \chi_2 \quad , \quad (66)$$

where λ is the stagger angle and χ_2 is the outlet camber angle. A description of the various geometric angles is shown in Figure 58.

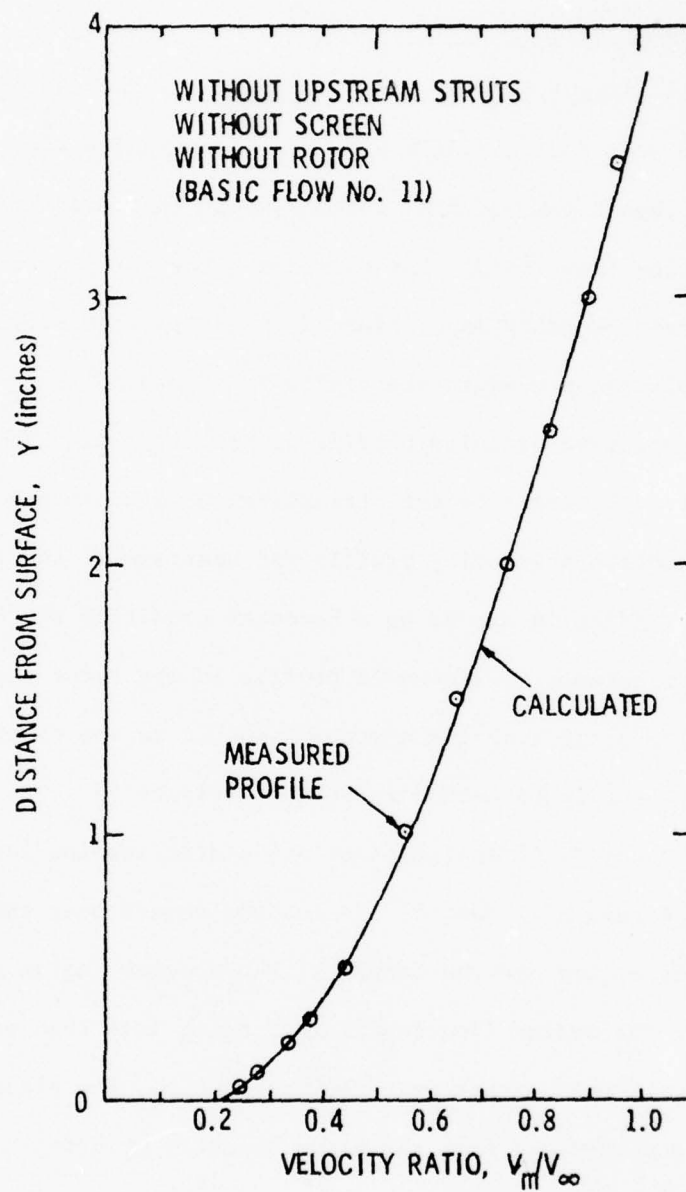


Figure 56. Calculated Meridional Velocity Profile for Basic Flow No. 11

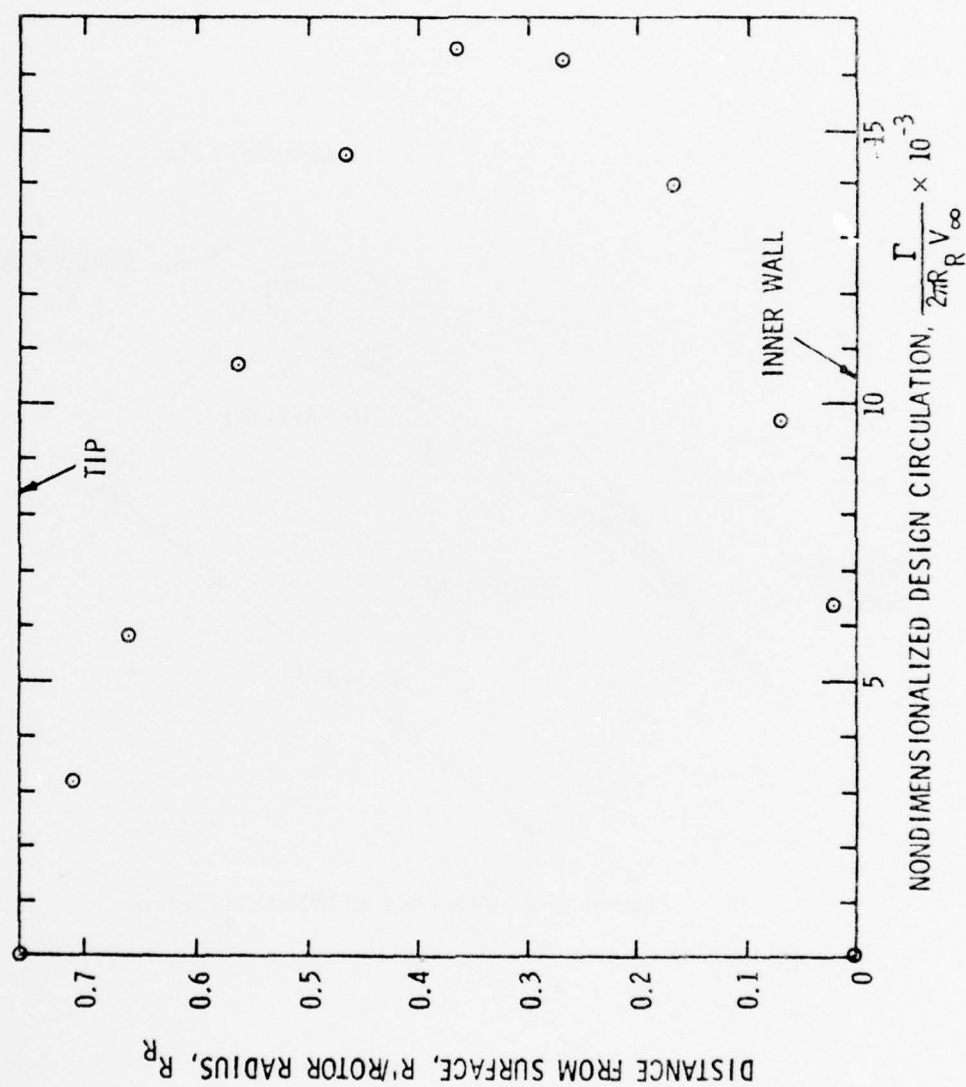


Figure 57. Design Circulation of Rotor

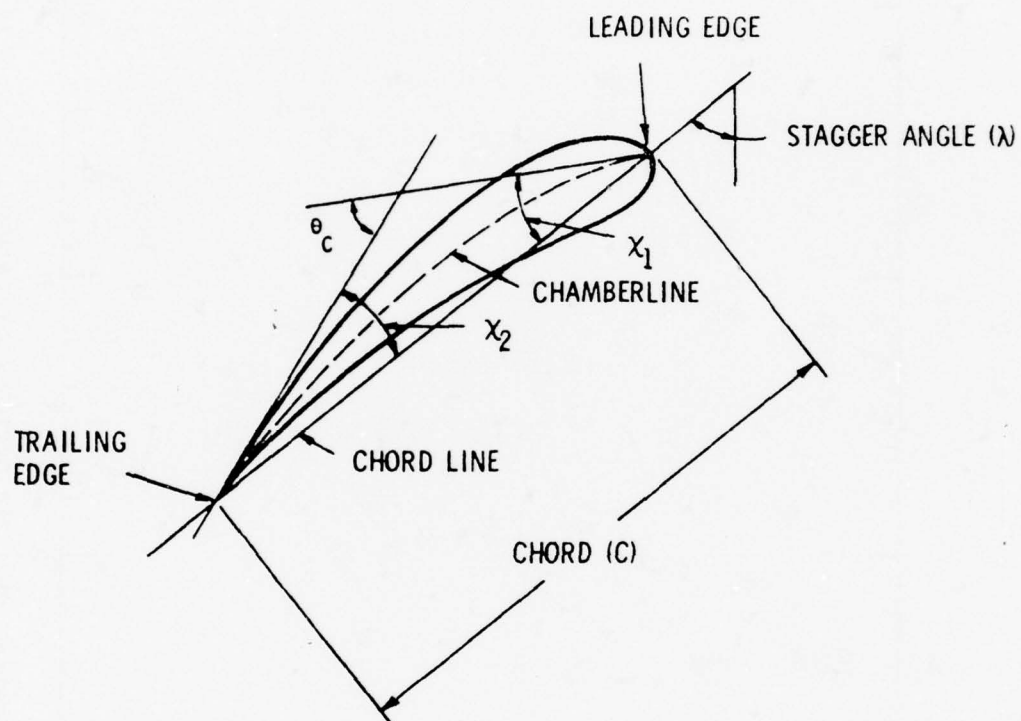


Figure 58. Geometry of Blade Sections

The first estimate of the flow outlet angles (Step 3) was calculated using the blade outlet angles (β_2) and a deviation angle based on Howell's correlation given by Equation (27). The flow outlet angles are given in Table 5 for Basic Flow No. 1.

Using the estimated flow outlet angles and the design flow coefficient, the flow field was calculated using the streamline curvature equations (Step 4). There were forty-eight streamlines calculated in the flow field of which twenty-eight were through the rotor plane, the first streamline being at the inner wall and the twenty-eighth streamline going through the rotor tip. The streamlines through the rotor were spaced more closely near the inner wall because secondary flows are most important near the inner wall. Some of the results at several radii are given in Table 5. The streamline curvature equations are inviscid so that there is a finite positive velocity at the inner wall. More details of the flow field for all the streamlines are given in Reference [55].

The velocity components given in Table 5 are for radii used in the flow outlet angle calculations. A comparison shows a large acceleration of the axial velocity through the rotor with the exception of the rotor tip where the flow is most difficult to define.

A second estimate of the flow outlet angles (Step 5) for this rotor was made using the flow field calculated in Step 4. The inlet flow angles (β_1) and the axial velocity ratios (AVR) were computed so that a method developed by Lieblein [40] was applied to estimate the deviation angle for any blade incidence angle. The effects of axial acceleration ($\Delta\delta'$), blade thickness ($\Delta\delta^*$), and camber (δ_0) given by Equations (29), (30), and (31), respectively, were calculated for the primary blade radii.

TABLE 5

OUTLET ANGLES USING HOWELL'S CORRELATION
(STEP 4) FOR BASIC FLOW NO. 1

R/R_R	β_2	δ_H	β_2^*
0.26	49.0	3.0	52.0
0.30	49.8	4.0	53.8
0.40	52.7	4.6	57.3
0.50	55.9	5.1	61.0
0.60	59.6	5.8	65.4
0.70	63.5	5.3	68.8
0.80	67.2	4.5	71.7
0.90	70.2	3.1	73.3
0.95	73.3	1.9	75.2

R/R_R	Inlet Velocity Profile		Outlet Velocity Profile			AVR
	V_x/V_∞	β_1	V_x/V_∞	V_θ/V_∞	β_2^*	
0.26	0.401	65.8	0.489	0.260	52.3	1.217
0.30	0.509	63.7	0.569	0.254	53.8	1.117
0.40	0.631	65.3	0.719	0.249	57.4	1.139
0.50	0.706	67.7	0.828	0.229	60.9	1.172
0.60	0.764	69.7	0.861	0.175	65.5	1.127
0.70	0.812	71.4	0.886	0.129	68.8	1.091
0.80	0.841	73.0	0.895	0.087	71.4	1.064
0.90	0.864	74.4	0.916	0.055	73.2	1.061
0.95	0.872	75.1	0.854	0.021	75.2	0.979

The deviation angles for Basic Flow No. 1 are given in Table 6 where the total deviation angle (δ) was determined from

$$\delta = \delta_o + \Delta\delta^* - \Delta\delta' \quad . \quad (67)$$

These new deviation angles were used to calculate a second estimate of flow outlet angles. A second calculation of the flow field (Step 6) was then conducted. The resulting inlet and outlet velocity components are given in Table 6 for the primary rotor radii. It is important to note that the major differences in the second calculation of the flow field as compared to the first calculation with Howell's correlation are due to the effects of acceleration near the mid-radius and the effects of blade thickness near the inner wall. The tangential velocity near the inner wall was reduced primarily by the effect of thickness and the axial velocity near the mid-radius was increased by including the AVR effect.

An estimate of the rotor streamlines was calculated from the flow analysis using the second estimate of flow outlet angles. The effect of secondary flows can now be calculated along the twenty-eight rotor streamlines. Equations (37) and (41) were used to calculate $\omega_{n,2}$ and $\omega_{s,2}$, respectively.

These secondary flow equations give the change in vorticity due to the presence of the blades. The difference in the streamwise vorticity between the rotor exit ($\omega_{s,2}$) and the inlet ($\omega_{s,1}$) is the passage secondary vorticity. The effect of this additional vorticity was found by initially solving for a secondary stream function (Equation 55) in the rotor exit plane. The solution of Equation (55) was then used in Equation (64) to obtain a deviation angle due to the passage secondary vorticity ($\Delta\delta_s$).

TABLE 6

OUTLET ANGLES USING NASA'S CORRELATION
(STEP 5) FOR BASIC FLOW NO. 1

R/R_R	β_2	δ_o	$\Delta\delta^*$	$\Delta\delta'$	β_2^*
0.26	49.0	2.6	10.1	4.5	57.2
0.30	49.8	3.5	6.9	2.2	58.0
0.40	52.7	4.6	4.2	2.5	59.0
0.50	55.9	5.4	2.5	2.9	60.9
0.60	59.6	5.7	1.7	2.0	65.0
0.70	63.5	5.1	1.3	1.4	68.5
0.80	67.2	4.4	0.7	0.9	71.4
0.90	70.2	3.2	0.6	0.8	73.2
0.95	73.3	1.5	0.3	0.0	75.1

R/R_R	<u>Inlet Velocity Profile</u>		<u>Outlet Velocity Profile</u>			AVR
	V_x/V_∞	β_1	V_x/V_∞	V_θ/V_∞	β_2^*	
0.26	0.370	67.5	0.432	0.215	57.5	1.167
0.30	0.483	64.9	0.516	0.209	57.9	1.069
0.40	0.618	65.8	0.692	0.244	58.9	1.120
0.50	0.704	67.8	0.831	0.229	60.9	1.181
0.60	0.768	69.6	0.877	0.185	64.9	1.148
0.70	0.818	71.3	0.905	0.139	68.3	1.107
0.80	0.845	72.9	0.899	0.090	71.3	1.063
0.90	0.867	74.4	0.921	0.058	73.1	1.063
0.95	0.874	75.0	0.860	0.024	75.1	0.984

The effect of the passage secondary vorticity can be seen in Table 7 which lists the final flow outlet angles used in the calculation of the final flow field for Basic Flow No. 1. Secondary flows are only significant near the inner wall where the inlet velocity gradients are the largest. The result is an overturning of the flow field near the inner wall where the inlet velocity gradients are the largest. The result is an overturning of the flow field near the inner wall giving a larger tangential velocity (V_θ) than expected. Outside this small region near the inner wall, the secondary passage vorticity does not have a significant effect on the deviation angle. The calculations gave a deviation angle change of less than 0.2° in this outer region.

A third calculation of the flow field (Step 9) was done by including the secondary flow effects with the previous NASA deviation angles. Because each deviation angle was calculated for a slightly different flow field, a check was made on the effects of axial acceleration, camber, and blade thickness on the deviation angles using the flow field calculated in Step 9. The results showed changes less than 0.2° in the final deviation angle (δ). Therefore, the flow field calculated in Step 9 was the final flow field. The final deviation angles for Basic Flow No. 1 are given in Table 7.

A correlation can now be made between the calculated flow field (Step 9) and the measured rotor inlet and outlet profiles which were discussed in Section 3.3. A comparison between the calculated and measured inlet velocity profiles to the rotor is shown in Figure 59. In this figure, the measured meridional velocity profile was corrected to the axial velocity profile using the streamline angles which were less than 8° . This figure shows quite good correlation except near the

TABLE 7
FINAL OUTLET ANGLES FOR BASIC FLOW NO. 1

R/R_R	β_2	δ_o	$\Delta\delta^*$	$\Delta\delta'$	$\Delta\delta_s$	β_2^*
0.26	49.0	2.5	12.2	3.3	-5.3	55.1
0.30	49.8	3.6	7.2	2.1	-2.9	55.6
0.40	52.7	4.7	4.0	2.3	-0.9	58.2
0.50	55.9	5.4	2.4	2.9	0.0	60.8
0.60	59.6	5.8	1.7	2.2	0.0	64.9
0.70	63.5	5.2	1.2	1.6	0.0	68.3
0.80	67.2	4.5	0.8	0.8	0.0	71.7
0.90	70.2	3.2	0.6	1.0	0.0	73.0
0.95	73.3	1.8	0.0	0.0	0.0	75.1

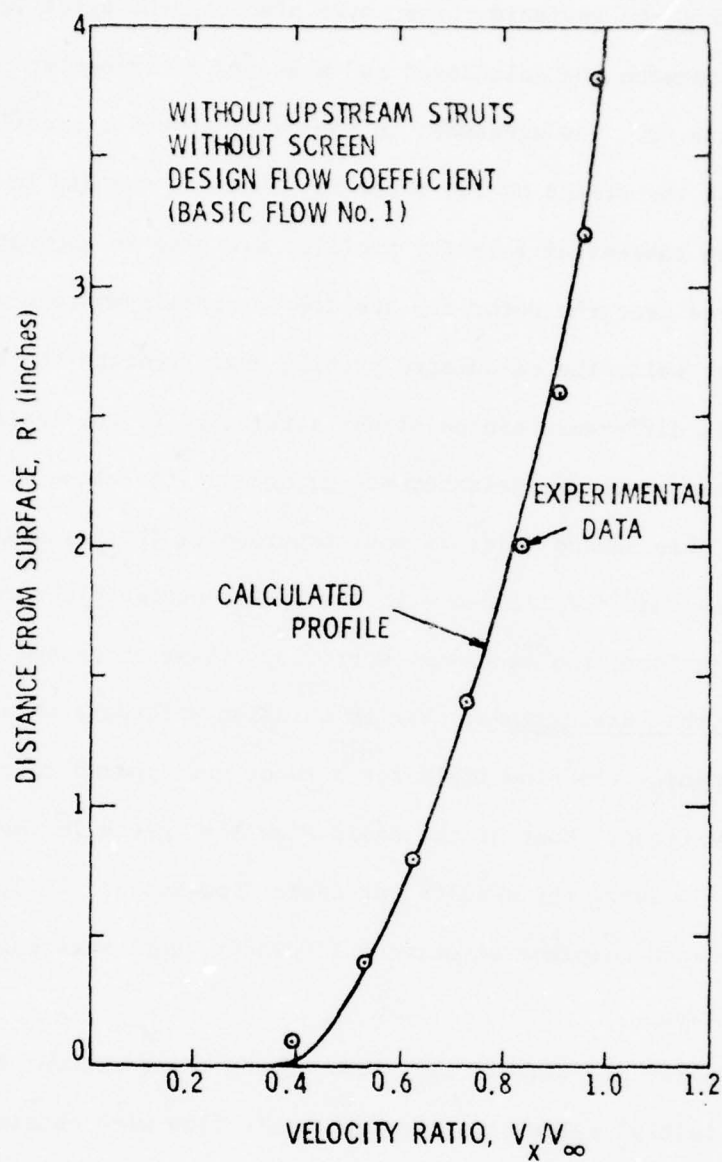


Figure 59. Rotor Inlet Velocity Comparison for Basic Flow No. 1

inner wall where the inviscid theory over predicts the axial velocity. A comparison between the calculated and measured rotor outlet profile is shown in Figure 60. The agreement in the axial velocity profile is quite good including the effect of the rotor tip shown by the dip in the axial velocity. The tangential velocity profiles are also in good agreement. The differences near the rotor tip are due to nonaxisymmetric effects. Near the inner wall, the calculated profile over predicts the measured profile. This difference can be either attributed to the inviscid secondary flow theory or to the measurements being made too close to the rotor exit plane. This second point is most important. The secondary flow theory assumes that the induced velocity field occurs in the rotor exit plane when, in fact, the secondary vorticity filaments extend downstream.

5.1.2 Other Basic Flows. The calculation procedure shown in Figure 50 for determining the flow field for a rotor was applied to other basic flow configurations. Most of the Basic Flow Nos. given in Table 1 were calculated. However, the results for Basic Flow Nos. 1, 2, 3, and 4 are presented because complete experimental velocity data were only available for these flows.

The velocity profiles in the plane of the rotor without the rotor used in the initial calculation of each basic flow were obtained from experimental data presented in Section 3.3.1. All of the basic flows had an axisymmetric velocity profile with the exception of Basic Flow No. 4. For this case which had upstream struts, a circumferentially averaged profile was used.

The flow outlet angles (β_2^*) were determined for each basic flow by the method previously outlined. The final angles are given in Table 7 for Basic Flow No. 1, in Table 8 for Basic Flow No. 2, in Table 9 for

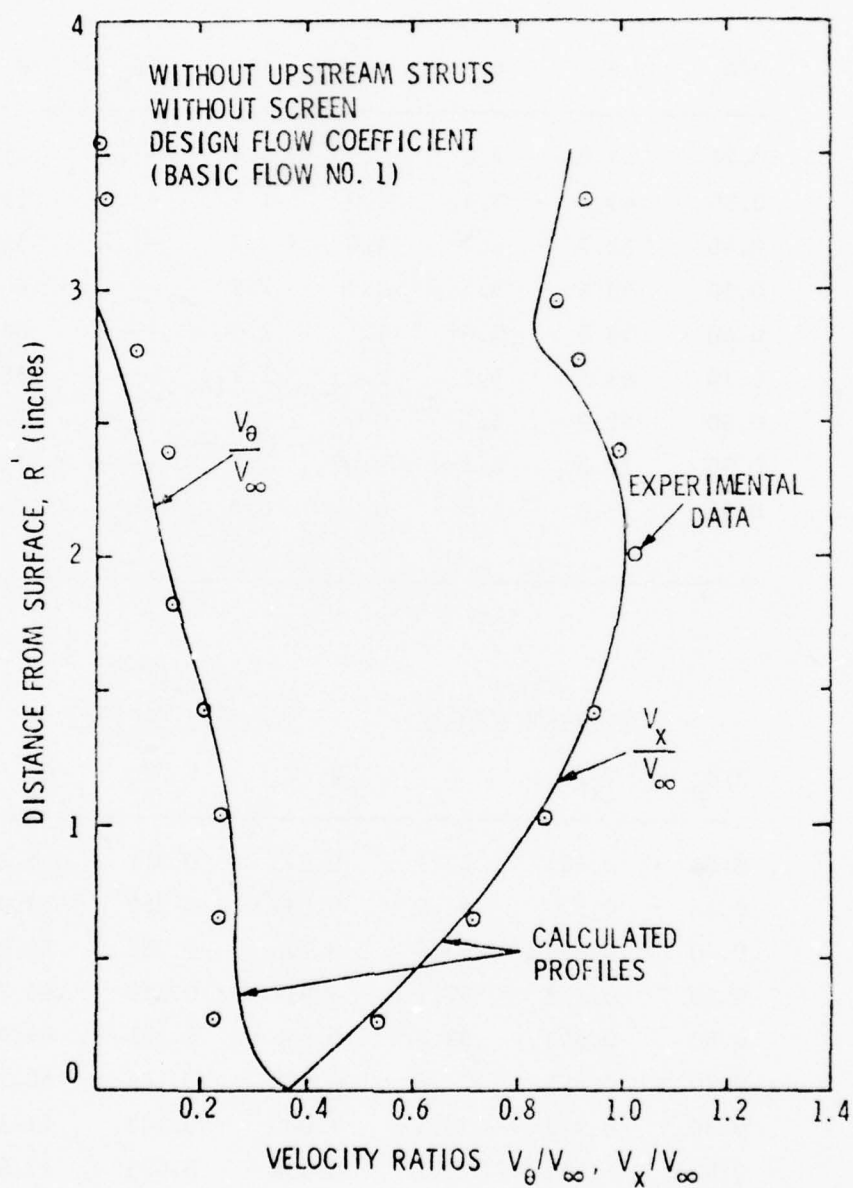


Figure 60. Rotor Outlet Velocity Comparison for Basic Flow No. 1

TABLE 8
FINAL OUTLET ANGLES FOR BASIC FLOW NO. 2

R/R_R	β_2	δ_o	$\Delta\delta^*$	$\Delta\delta'$	$\Delta\delta_s$	β_2^*
0.26	49.0	2.6	9.6	3.4	-5.9	51.9
0.30	49.8	3.4	7.0	1.1	-3.2	55.9
0.40	52.7	4.7	4.0	2.2	-1.1	58.1
0.50	55.9	5.4	2.3	2.9	----	60.7
0.60	59.6	5.8	1.7	2.3	----	64.8
0.70	63.5	5.2	1.2	1.7	----	68.2
0.80	67.2	4.5	0.8	1.4	----	71.1
0.90	70.2	3.2	0.6	1.1	----	72.9
0.95	73.3	1.9	0.3	0.0	----	75.5

R/R_R	Inlet Velocity Profile		Outlet Velocity Profile		
	V_x/V_∞	β_1	V_x/V_∞	V_θ/V_∞	β_2^*
0.26	0.465	64.9	0.543	0.301	51.8
0.30	0.569	63.6	0.594	0.269	55.9
0.40	0.693	65.6	0.774	0.280	58.2
0.50	0.779	67.8	0.917	0.279	60.7
0.60	0.843	69.8	0.966	0.231	64.9
0.70	0.891	71.6	0.998	0.184	68.2
0.80	0.912	73.4	1.000	0.132	71.1
0.90	0.914	75.1	1.034	0.095	72.8
0.95	0.913	75.9	0.927	0.043	75.5

TABLE 9
FINAL RESULTS FOR BASIC FLOW NO. 3

R/R_R	β_2	δ_o	$\Delta\delta^*$	$\Delta\delta'$	$\Delta\delta_s$	β_2^*
0.26	49.0	2.5	9.0	2.9	-5.5	52.1
0.30	49.8	3.4	6.8	1.8	-2.9	55.3
0.40	52.7	4.6	4.0	2.2	-1.1	58.0
0.50	55.9	5.4	2.7	2.9	----	61.1
0.60	59.6	5.8	1.7	2.2	----	64.9
0.70	63.5	5.2	1.4	1.6	----	68.5
0.80	67.2	4.5	0.8	0.9	----	71.6
0.90	70.2	3.2	0.6	1.0	----	72.9
0.95	73.3	1.9	0.3	0.0	----	75.5

R/R_R	Inlet Velocity Profile		Outlet Velocity Profile		
	V_x/V_∞	β_1	V_x/V_∞	V_θ/V_∞	β_2^*
0.26	0.442	63.7	0.495	0.258	52.1
0.30	0.515	63.5	0.557	0.227	55.3
0.40	0.636	65.1	0.707	0.239	58.1
0.50	0.708	67.7	0.821	0.236	61.1
0.60	0.758	69.8	0.871	0.197	65.0
0.70	0.804	71.6	0.892	0.149	68.5
0.80	0.830	73.2	0.882	0.099	71.6
0.90	0.844	74.7	0.934	0.075	72.8
0.95	0.847	75.5	0.831	0.027	75.6

Basic Flow No. 3, and in Table 10 for Basic Flow No. 4. A comparison between basic flows shows large differences in outlet angles near the inner wall. Additional streamline data are given in Reference [55].

A comparison between the calculated and experimental rotor inlet and outlet profiles is given in Figures 59 and 60 for Basic Flow No. 1, in Figures 61 and 62 for Basic Flow No. 2, in Figures 63 and 64 for Basic Flow No. 3, and in Figures 65 and 66 for Basic Flow No. 4. In general, the calculations are in good agreement with the experimental results. The calculated axial velocity near the inner wall is greater for the inlet profiles and for most outlet profiles. The tangential velocity profile is over predicted for all basic flows near the inner wall. This is due to the secondary vorticity model which assumes that the influence of the vorticity on the velocity field occurs in the trailing edge plane of the rotor. Comparisons between basic flows show that the tangential velocity increased significantly by operating at a low flow coefficient and by adding upstream struts.

The torque coefficient is a measure of the magnitude of the tangential velocity. It is defined as

$$C_Q = \int_{R_i/R_R}^1 \left(\frac{V_\theta}{V_\infty} \right) \left(\frac{V_m}{V_\infty} \right) \left(\frac{r}{R_R} \right) d\left(\frac{r}{R_R} \right) \quad (68)$$

This coefficient was calculated from the flow field for each basic flow and was normalized by the coefficient obtained from a reference which was Basic Flow No. 1.

These torque results obtained from the calculated flow field are compared to experimental data as shown in Figure 67. The changes in

TABLE 10
FINAL RESULTS FOR BASIC FLOW NO. 4

R/R_R	β_2	δ_o	$\Delta\delta^*$	$\Delta\delta'$	$\Delta\delta_s$	β_2^*
0.26	49.0	2.5	8.7	1.2	-5.0	54.0
0.30	49.8	3.4	6.6	0.1	-3.2	56.5
0.40	52.7	4.6	4.1	2.9	-1.3	57.2
0.50	55.9	5.4	2.5	2.9	----	60.9
0.60	59.6	5.7	1.7	2.3	----	64.7
0.70	63.5	5.1	1.3	1.6	----	68.3
0.80	67.2	4.5	0.8	1.0	----	71.5
0.90	70.2	3.2	0.6	1.5	----	72.5
0.95	73.3	1.8	0.3	0.0	----	75.4

R/R_R	Inlet Velocity Profile		Outlet Velocity Profile		
	V_x/V_∞	β_1	V_x/V_∞	V_θ/V_∞	β_2^*
0.26	0.459	62.8	0.486	0.229	53.9
0.30	0.542	62.3	0.531	0.230	56.5
0.40	0.608	66.1	0.709	0.270	57.3
0.50	0.704	67.8	0.819	0.251	60.9
0.60	0.759	69.8	0.873	0.209	64.8
0.70	0.802	71.6	0.896	0.162	68.3
0.80	0.827	73.3	0.883	0.111	71.5
0.90	0.834	74.9	0.952	0.091	72.4
0.95	0.834	75.7	0.835	0.037	75.5

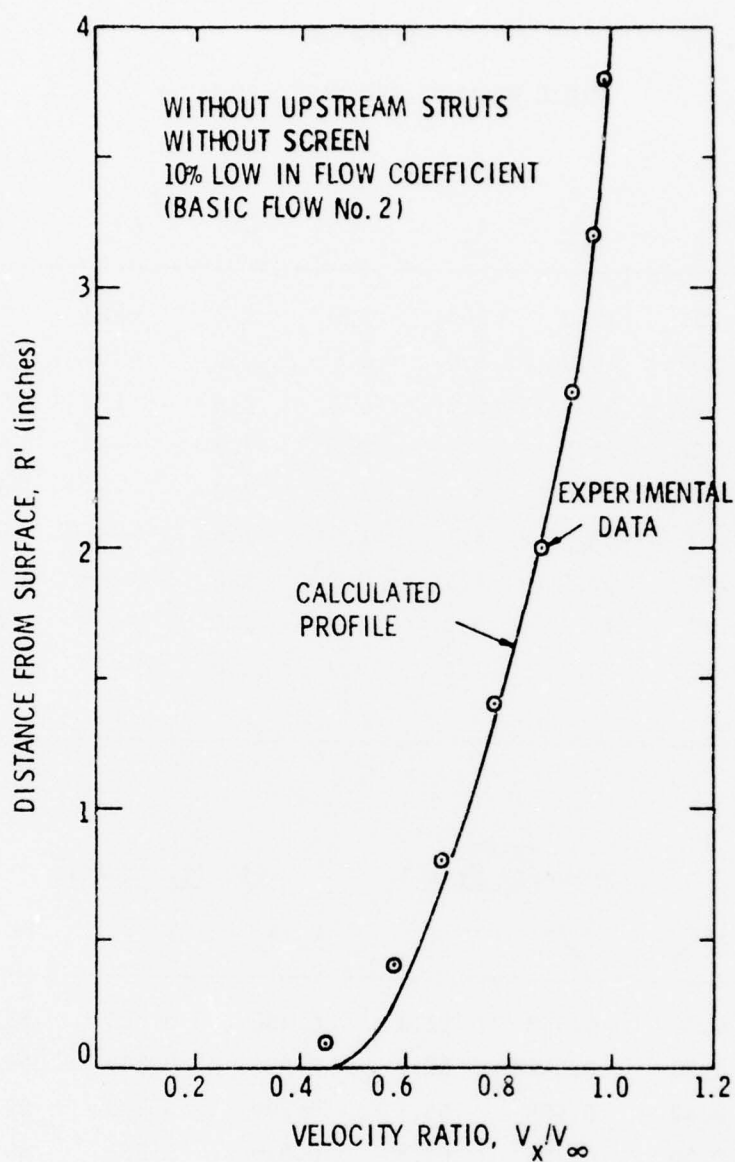


Figure 61. Rotor Inlet Velocity Comparison for Basic Flow No. 2

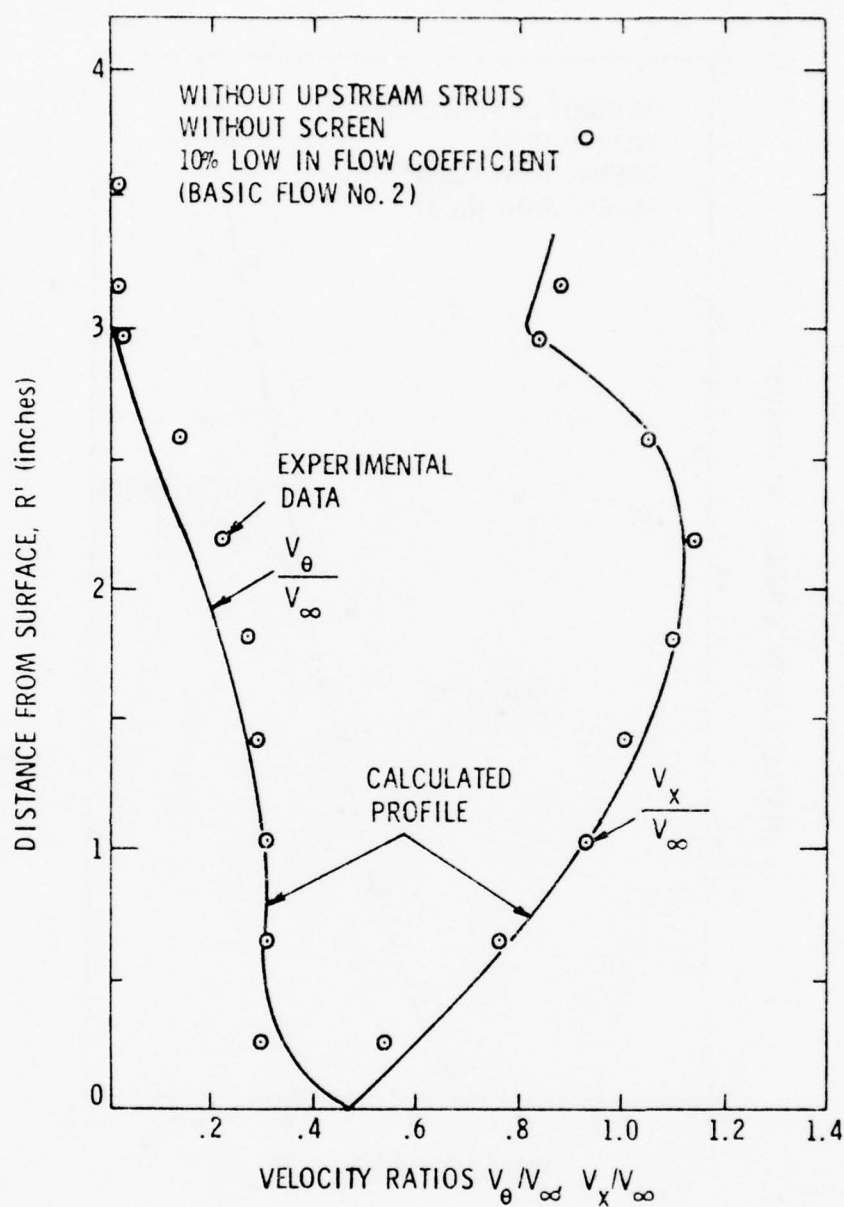


Figure 62. Rotor Outlet Velocity Comparison for Basic Flow No. 2

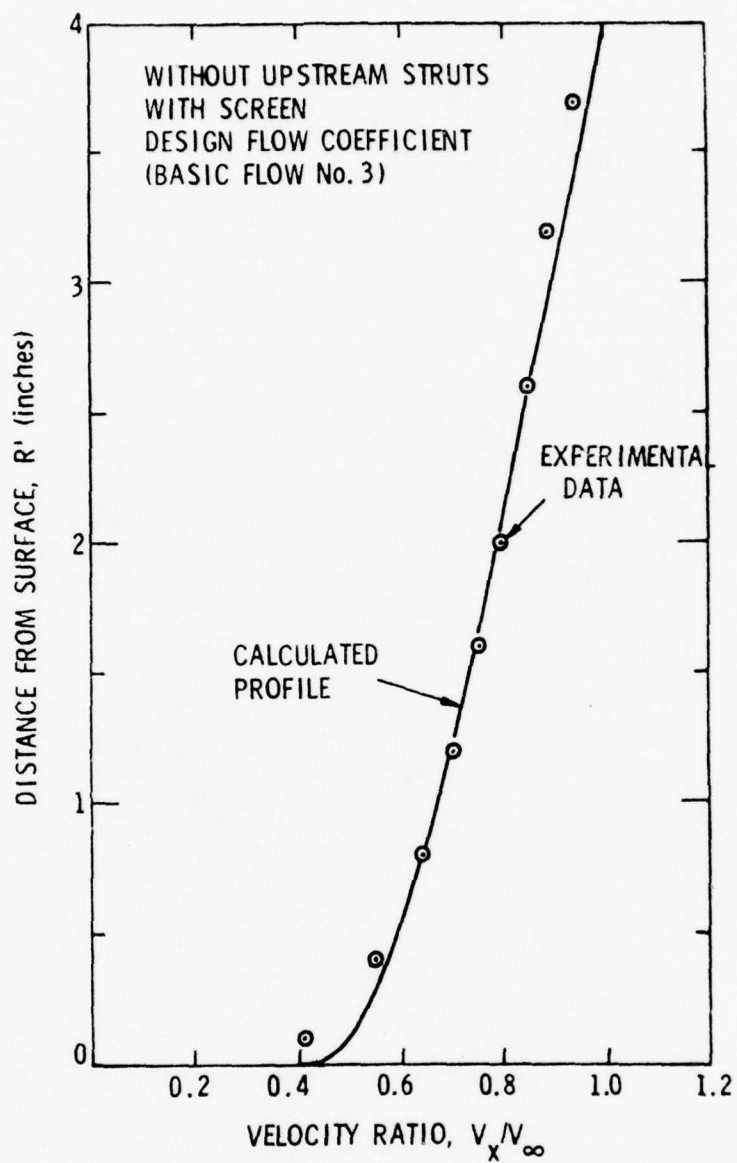


Figure 63. Rotor Inlet Velocity Comparison for Basic Flow No. 3

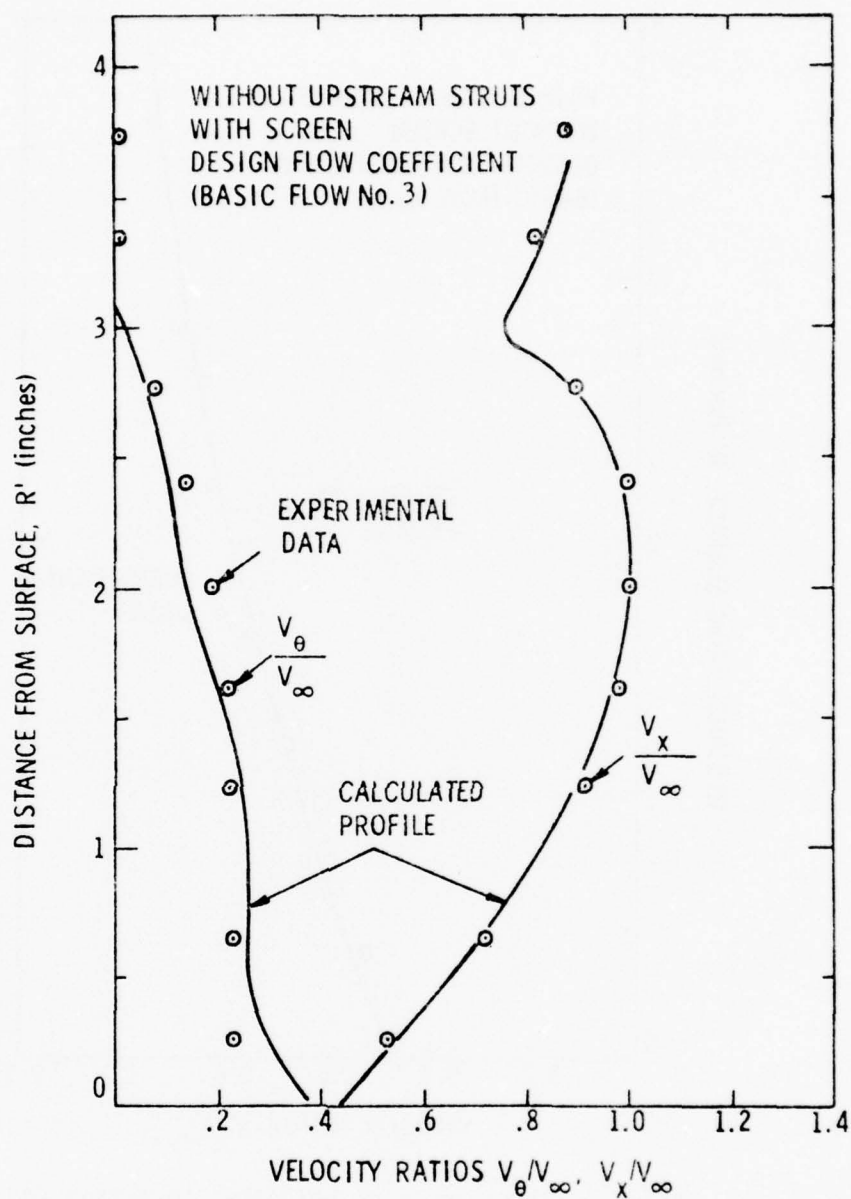


Figure 64. Rotor Outlet Velocity Comparison for Basic Flow No. 3

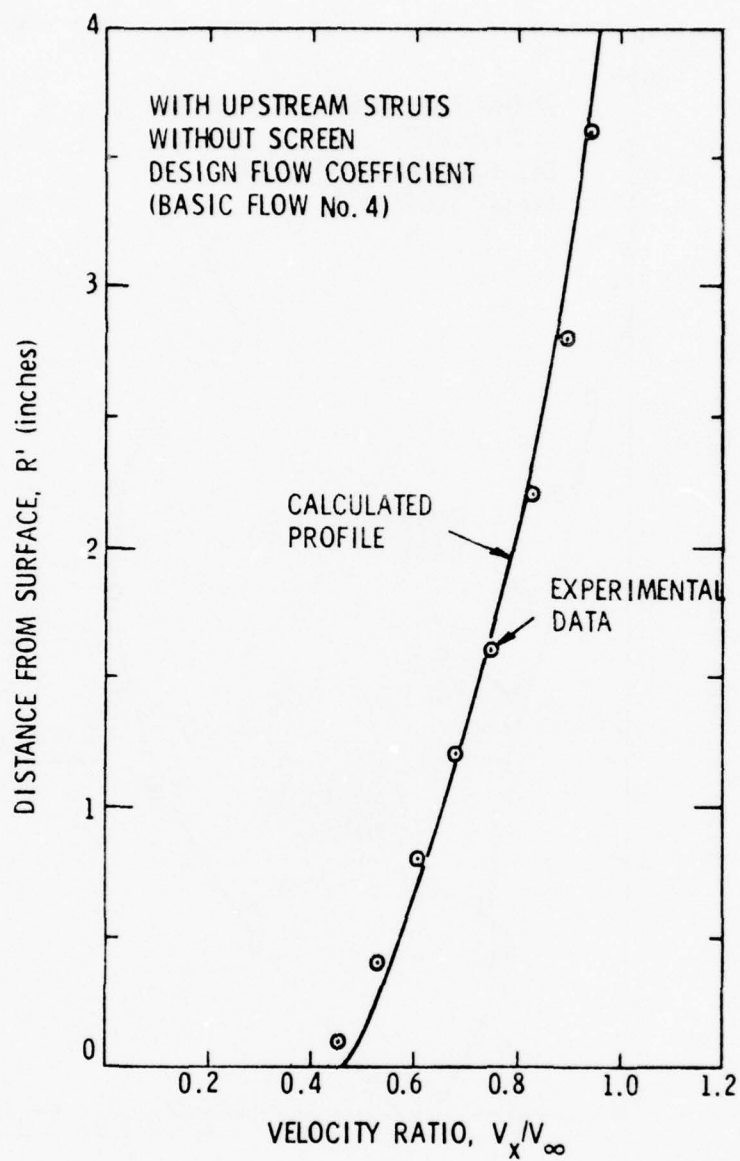


Figure 65. Rotor Inlet Velocity Comparison for Basic Flow No. 4

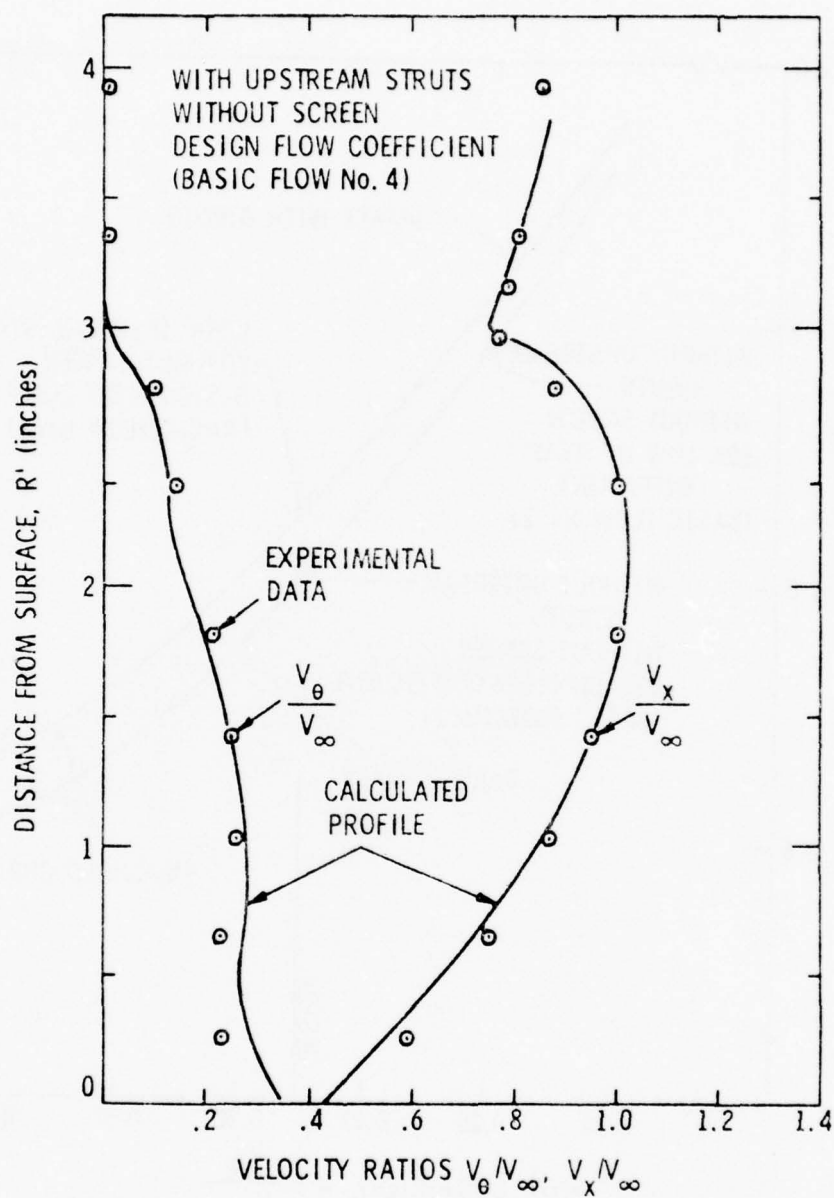


Figure 66. Rotor Outlet Velocity Comparison for Basic Flow No. 4

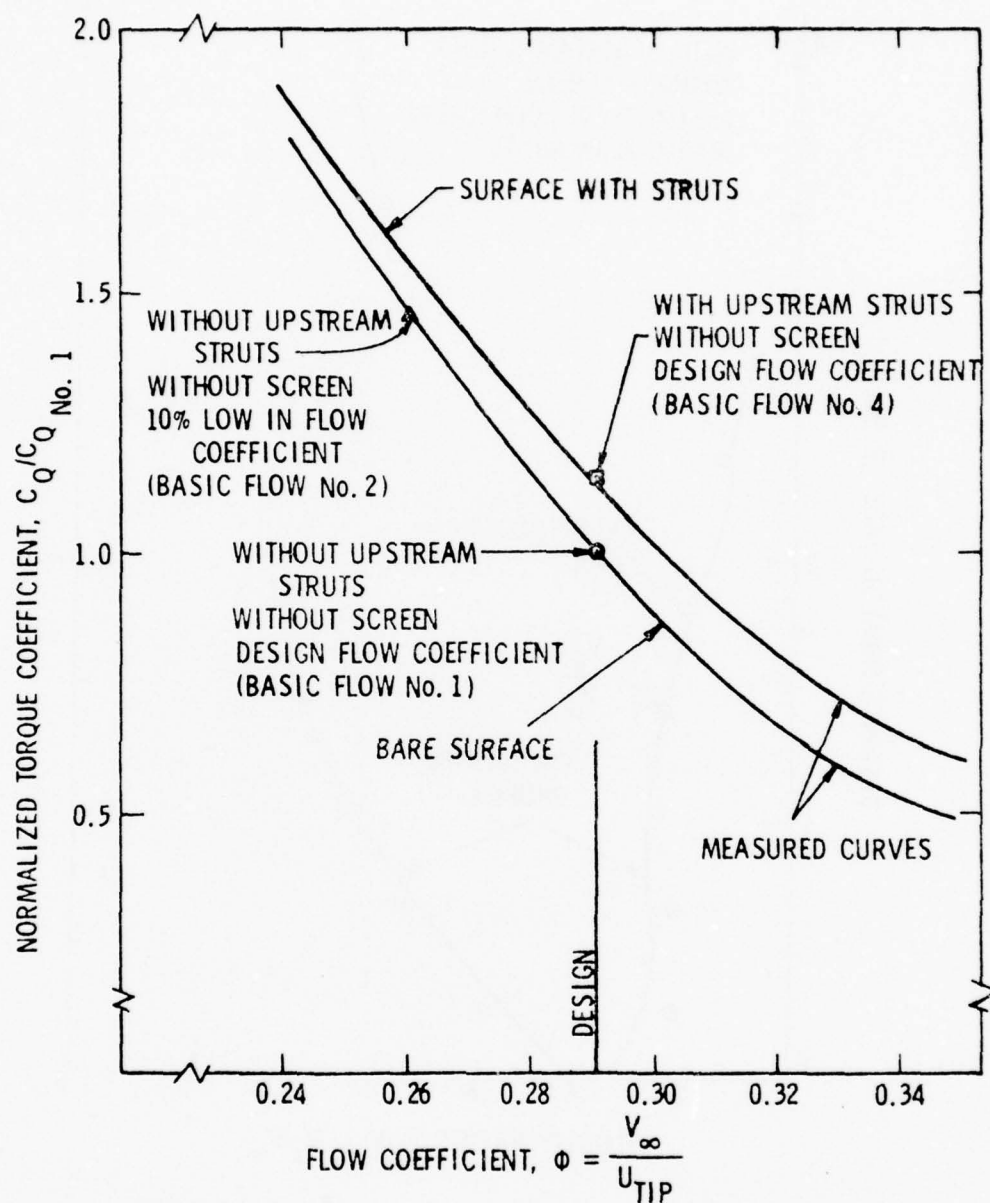


Figure 67. Normalized Torque Coefficient for Rotor

torque due to adding struts or operating off-design are predicted very well.

5.1.3 Comparisons Between Calculated and Measured Flow Fields at the End of the Rotor Cap. So far, only comparisons between flow field calculations and flow measurements near the rotor plane have been presented. The measured tangential velocity profile near the rotor plane does not show a well defined vortex near the inner wall. However, measurements of the tangential velocity profile at the end of the cap do show a vortex.

Figure 68 shows a comparison at the end of the rotor cap between the final flow field calculation (Step 9) and experimental data for Basic Flow No. 1. The tangential velocity profiles are in very good agreement outside of the vortex core; however, the axial velocity profiles do not agree near the vortex core. This is opposite to the correlation trends obtained at the rotor outlet between the calculated flow field and experimental data.

The end of the rotor cap is located several chord lengths downstream of the rotor exit plane. Therefore, it is not surprising that the agreement between the calculated flow field including secondary flows and measured tangential velocity profile agreement is better at the end of the rotor cap. The tangential velocity profile calculated by the streamline curvature equations using a secondary flow deviation angle compares well with the tangential velocity profile data outside of the rotational region of the vortex. A poor agreement is found inside the vortex core because of the assumptions used in the development of the streamline curvature equation.

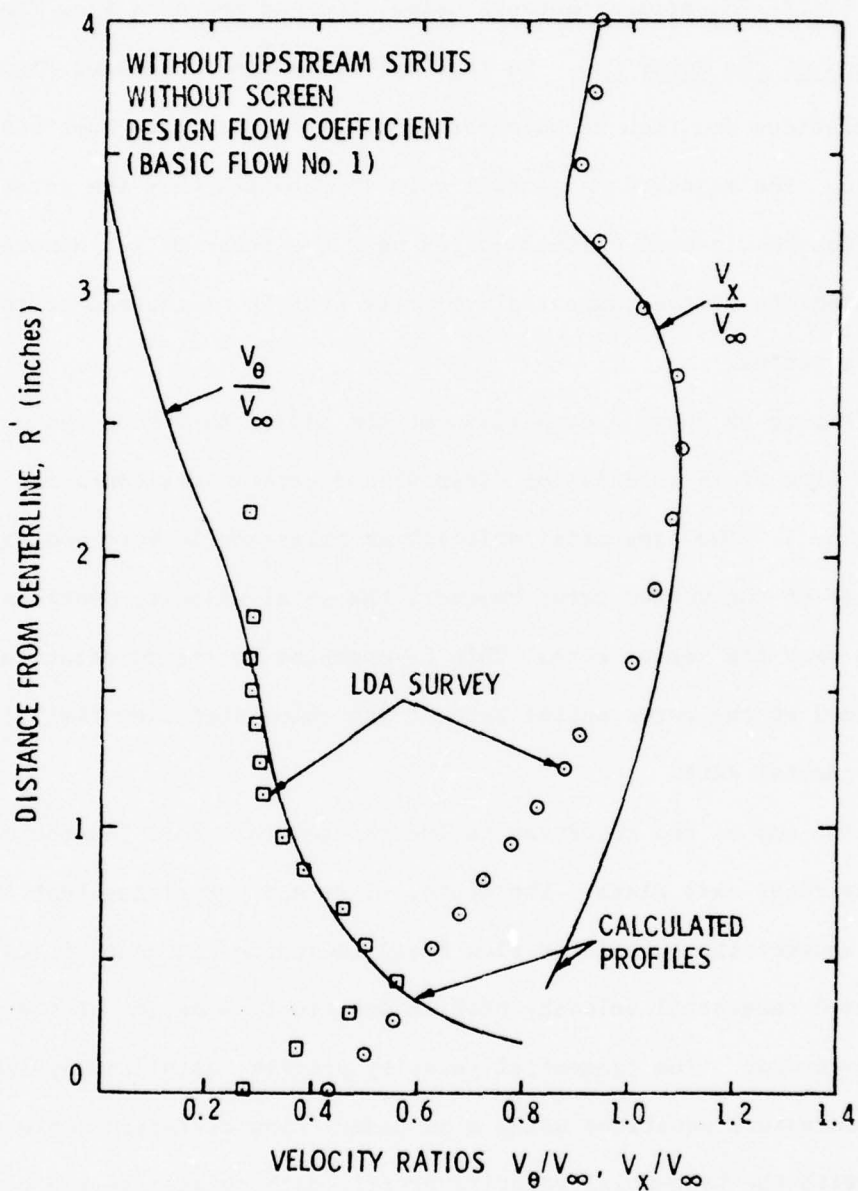


Figure 68. Rotor Cap Velocity Comparison for Basic Flow No. 1

In addition to the influence of the passage streamwise secondary vorticity on the tangential velocity profile, the secondary vorticity also changes the axial velocity profile. However, the net mass flow change to the axial velocity profile due to secondary vorticity must be zero.

The calculation of the change in axial velocity occurring downstream of a rotor plane due to the secondary vorticity is a difficult problem. Even assuming that downstream of the blade row the vorticity become distributed circumferentially, few good correlations with axial velocity exists and, in most cases, axial velocity changes are ignored.

Hawthorne [42] has shown that there are three components of axial vorticity downstream of the blade exit plane. One is the passage secondary vorticity; the other two are the trailing shed vorticity and the trailing filament vorticity which lie along the blade wake. The trailing shed vorticity is caused by a gradient in circulation along the blade span and the contributions of both the primary and secondary parts are included in the final flow field analysis (Step 9). The secondary part of the trailing shed vorticity is the change in blade turning due to the passage secondary vorticity.

Trailing filament vorticity arises from the cellular motion induced in the blade passage by the secondary streamwise vorticity. Dixon [50] derives an expression for the axial component of the combined passage and trailing filament vorticities. The results are

$$\omega_{x_A} = (\omega_{s_2} - \omega_{s_1}) \cos \beta_2^* - u_o \frac{N}{\pi r} \quad , \quad (69)$$

where u_0 is the radial perturbation velocity due to the secondary passage vorticity evaluated at $\theta = 0, 2\pi/N, \dots$. The radial velocity is given by Equation (49), knowing the solution of the stream function given by Equation (55).

The axial component of vorticity can be integrated over the radial direction to give an axial velocity variation. The constant of integration is obtained from continuity. Again, the net mass flow through a downstream plane induced by the axial component of vorticity must be zero.

Calculation of ω_x for Basic Flow No. 1 using Equation (69) shows that the axial secondary vorticity is approximately zero over the blade span. Thus, the axial component of passage secondary vorticity and the axial component of trailing filament vorticity are approximately equal and opposite at each streamline. Therefore, for Basic Flow No. 1 where the rotor operates within the inlet velocity gradient, no variation in axial velocity profile due to axial vorticity would be anticipated. This result was also shown by Smith [56].

However, the aforementioned result does not explain the large differences between measured and calculated axial velocity near the vortex core. The measured axial velocity profile correlated well with measurements made near the rotor plane. One possible hypothesis for this discrepancy is that the secondary flow field does not become distributed downstream of the rotor plane. Although the net axial secondary vorticity remains approximately zero, the passage vorticity remains concentrated and dominates the flow field near the rotor inner wall.

For this flow field, the axial velocity variation calculated by Equations (47) and (48) used in the solution of the secondary stream function was applied to the calculated profile at the end of the rotor

cap. The variation calculated for each of the twenty-eight streamlines in the rotor exit plane was added to the corresponding streamline in the rotor cap plane. The results are shown in Figure 69 for Basic Flow No. 1. The correlation between measured and calculated axial velocity profiles is very good using only the passage secondary vorticity.

Additional comparisons between the final flow field calculations (Step 9) and experimental data obtained at the rotor cap are given in Figures 70, 71, and 72. Comparisons between measured and calculated velocity profiles for Basic Flows No. 2, 3, and 4 are shown in Figures 70, 71, and 72, respectively. In all of these figures, an axial velocity variation due to secondary axial vorticity was not included.

5.2 Calculation of Secondary Vorticity and Vortex Parameters

5.2.1 Secondary Vorticity for Basic Flow No. 1. In the schematic for the calculation of the final flow field shown in Figure 50, the secondary flow calculation is shown in Step 7. This calculation not only adds the blade to blade flow effects due to secondary vorticity to the final flow field but also gives the vortex parameters. The substeps of Step 7 are shown in Figure 73.

For Step 7B, the vorticity was numerically calculated along a relative streamline (s') using Equation (34) for the relative normal component of the absolute vorticity ($\omega_{n,}$) and Equation (41) for the relative streamwise component of the absolute vorticity ($\omega_{s,}$). The flow parameters necessary for the vorticity calculation were defined along a relative streamline from the flow field calculation in Step 6. In all, the vorticity for twenty-eight relative streamlines was calculated for the rotor. The initial vorticity components ($\omega_{s,1}$, $\omega_{n,1}$) were calculated from

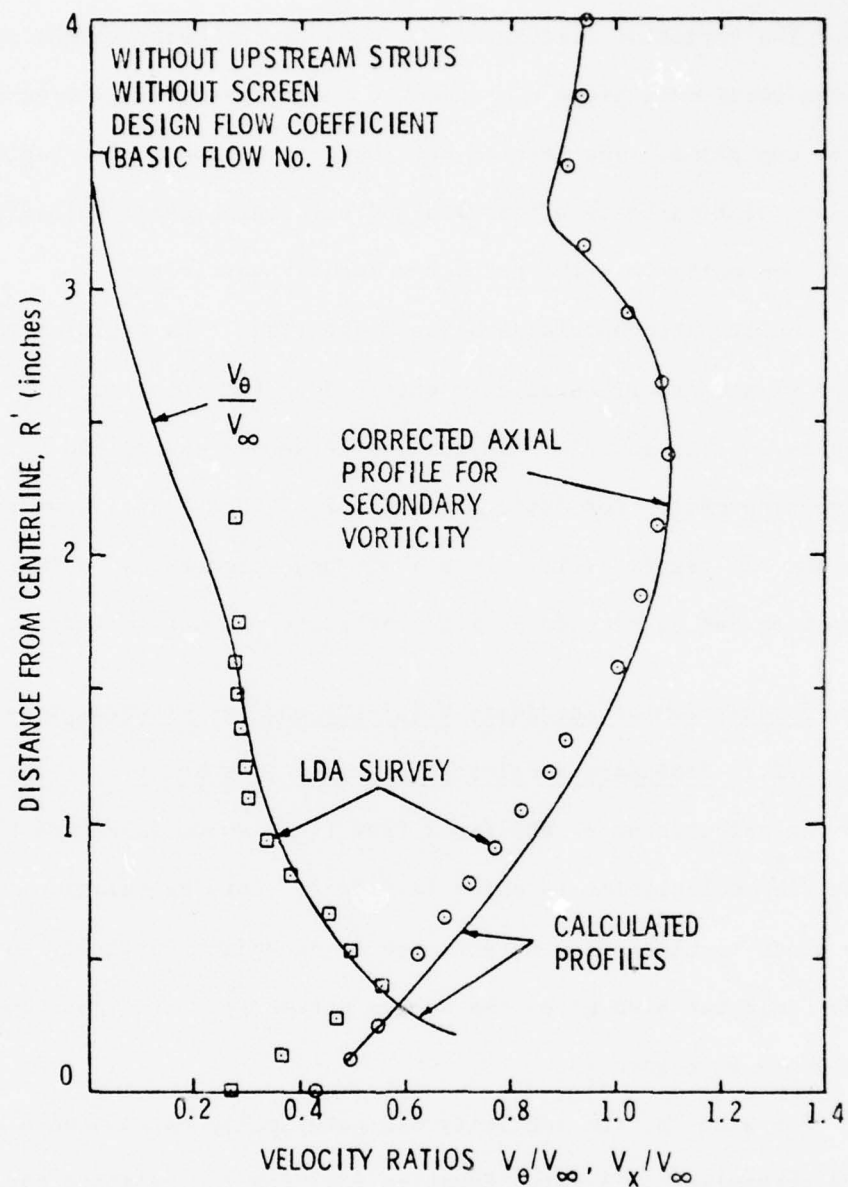


Figure 69. Rotor Cap Velocity Comparison Including Axial Velocity Variation for Basic Flow No. 1

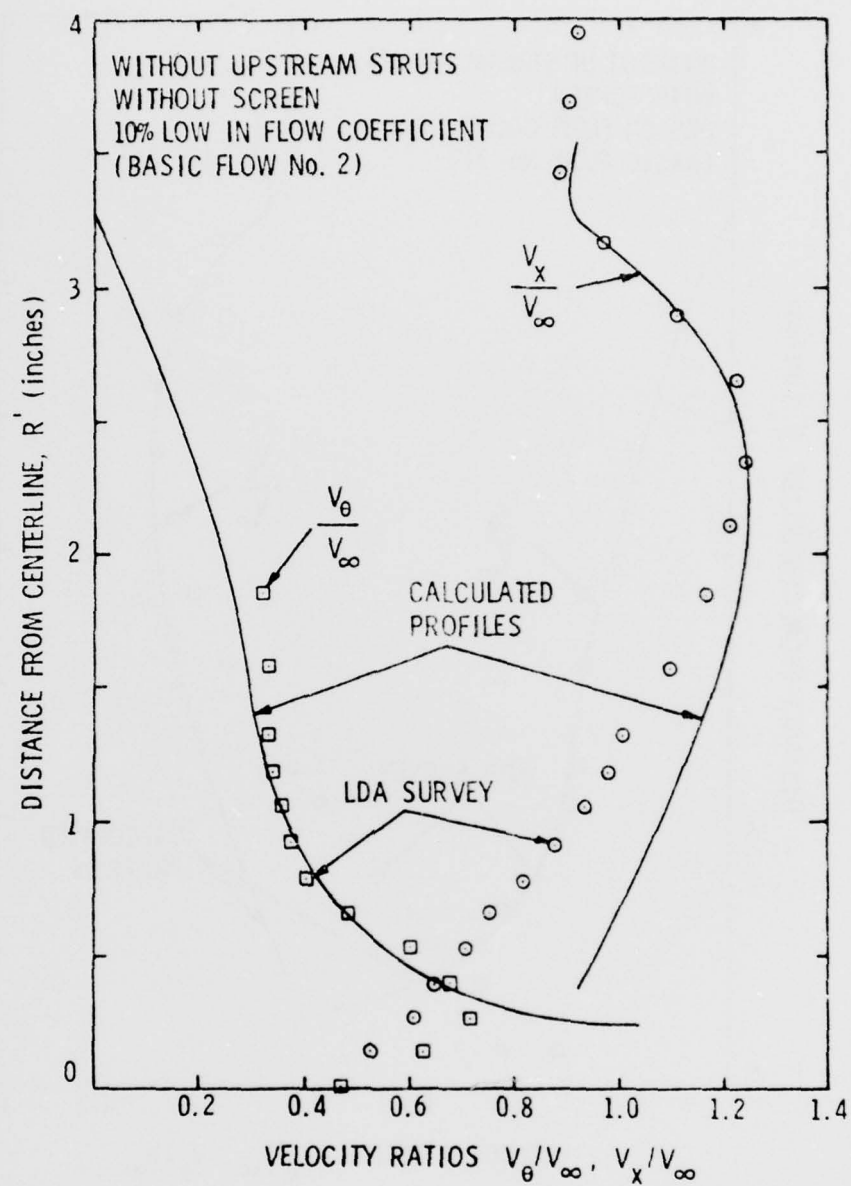


Figure 70. Rotor Cap Velocity Comparison for Basic Flow No. 2

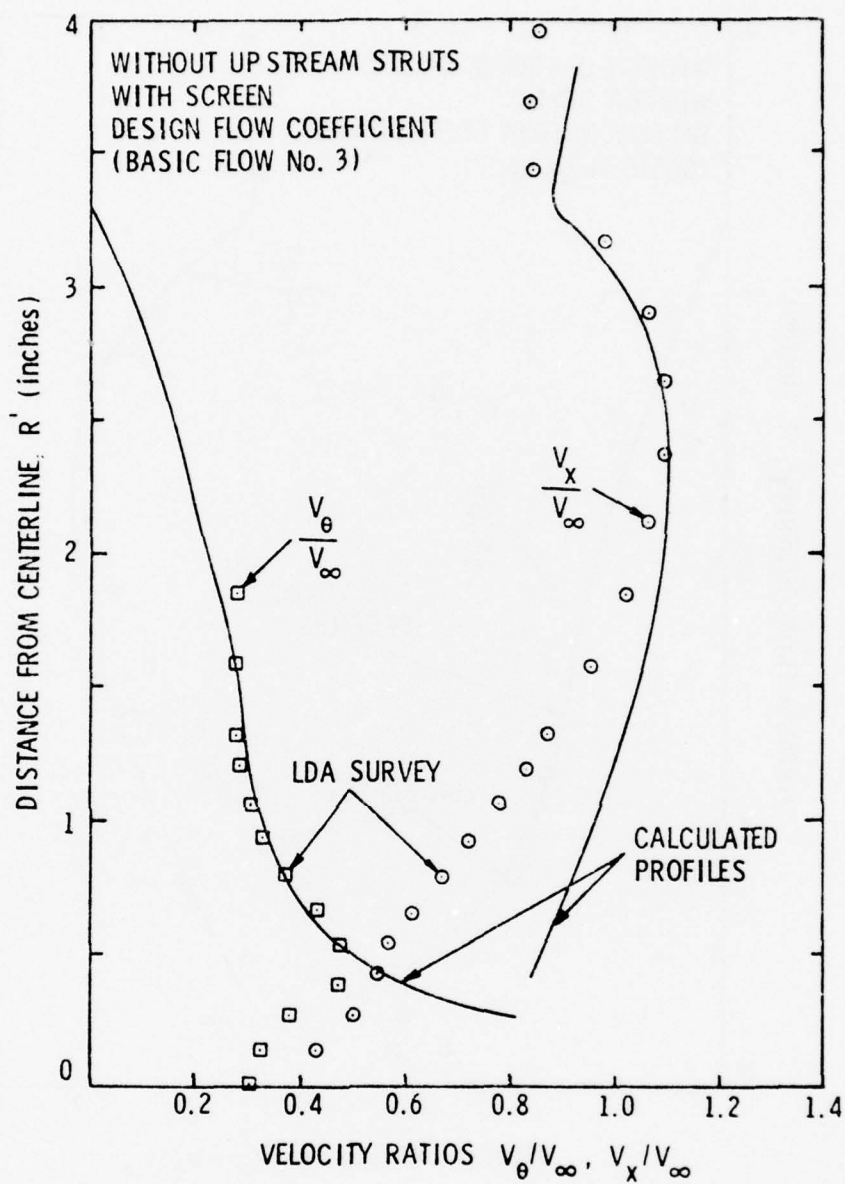


Figure 71. Rotor Cap Velocity Comparison for Basic Flow No. 3

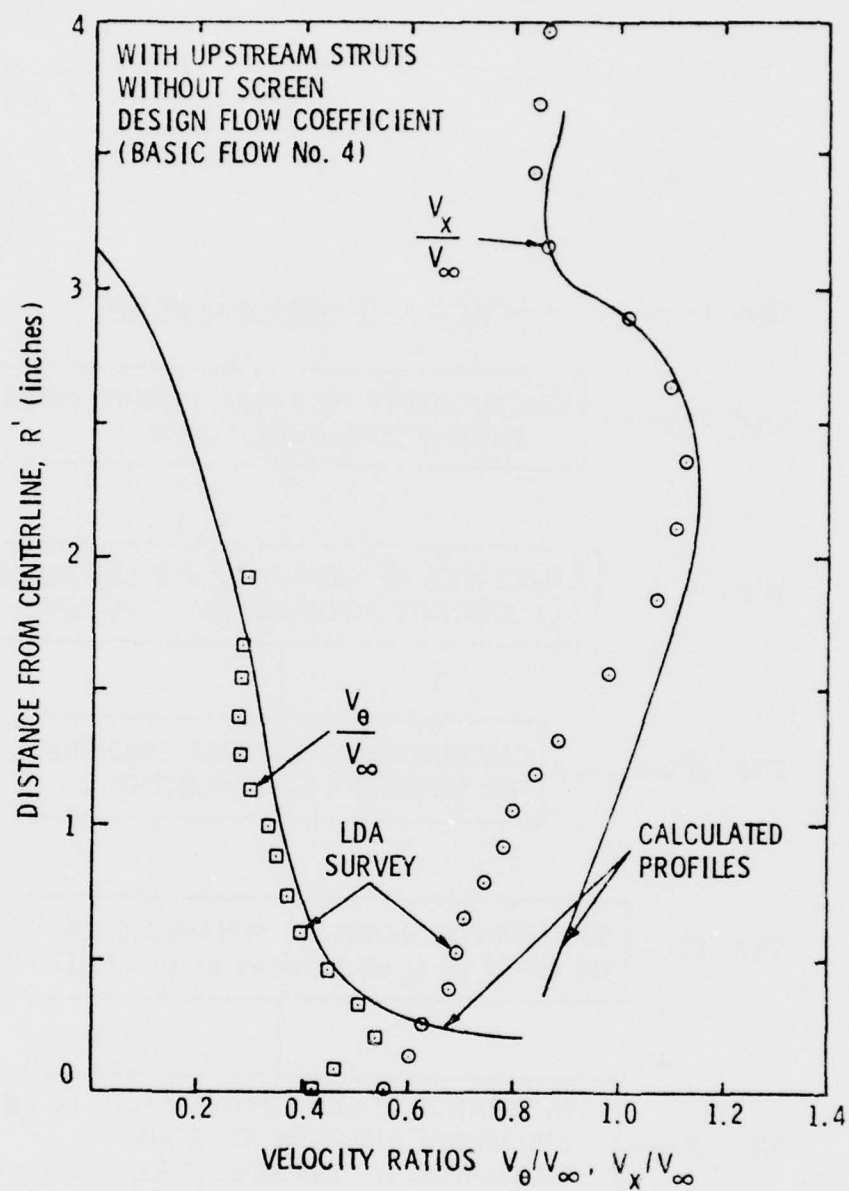


Figure 72. Rotor Cap Velocity Comparison for Basic Flow No. 4

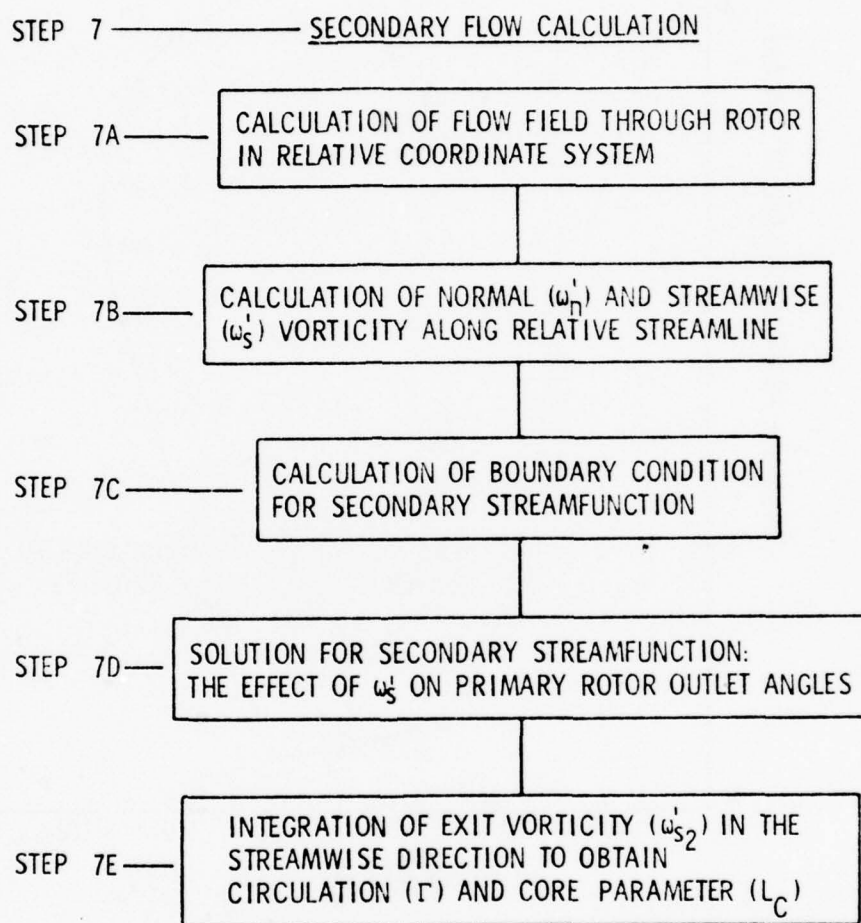


Figure 73. Outline of Secondary Flow Calculations

the inlet velocity gradient to the rotor as shown in Figure 54. The rotor inlet flow was axisymmetric and the velocity was nearly axial. Therefore, the normal component of absolute vorticity (ω_n) is the gradient of the meridional velocity profile. The normalized normal component of vorticity ($\bar{\omega}_n$) is shown in Figure 6 for Basic Flow No. 1.

As shown in Equation (34), the relative component of the normal vorticity depends on the variation of relative velocity (W) along a relative streamline, on the relative component of the absolute inlet normal vorticity (ω_{n1}), and on the flow convergence-divergence in the bi-normal direction (a_b). The results for Basic Flow No. 1 are given in Figure 74. The exit normal vorticity (ω_{n2}) is not very different from the inlet normal vorticity (ω_{n1}).

The normal vorticity calculations were used in Equation (41) for the calculation of the relative streamwise vorticity. The results for Basic Flow No. 1 are given in Figure 75. The exit relative streamwise vorticity (ω_{s2}) is very different from the inlet relative streamwise vorticity (ω_{s1}).

The terms of Equation (41) are shown in Figure 76. The first term is simply the turning of a normal component of vorticity and is small when compared to the other terms. The second term is also small and is the curvature induced vorticity. The third term is large and is due to rotation-induced vorticity. This result can be anticipated because the rotor operates at a low flow coefficient and hence Ω_n is large. The last term is simply the stretching of the vorticity by the flow and is large because of the high stagger angles at which the rotor operates.

The secondary passage vorticity is the difference between the inlet and outlet vorticities and is used in Step 7C and 7D for the calculation

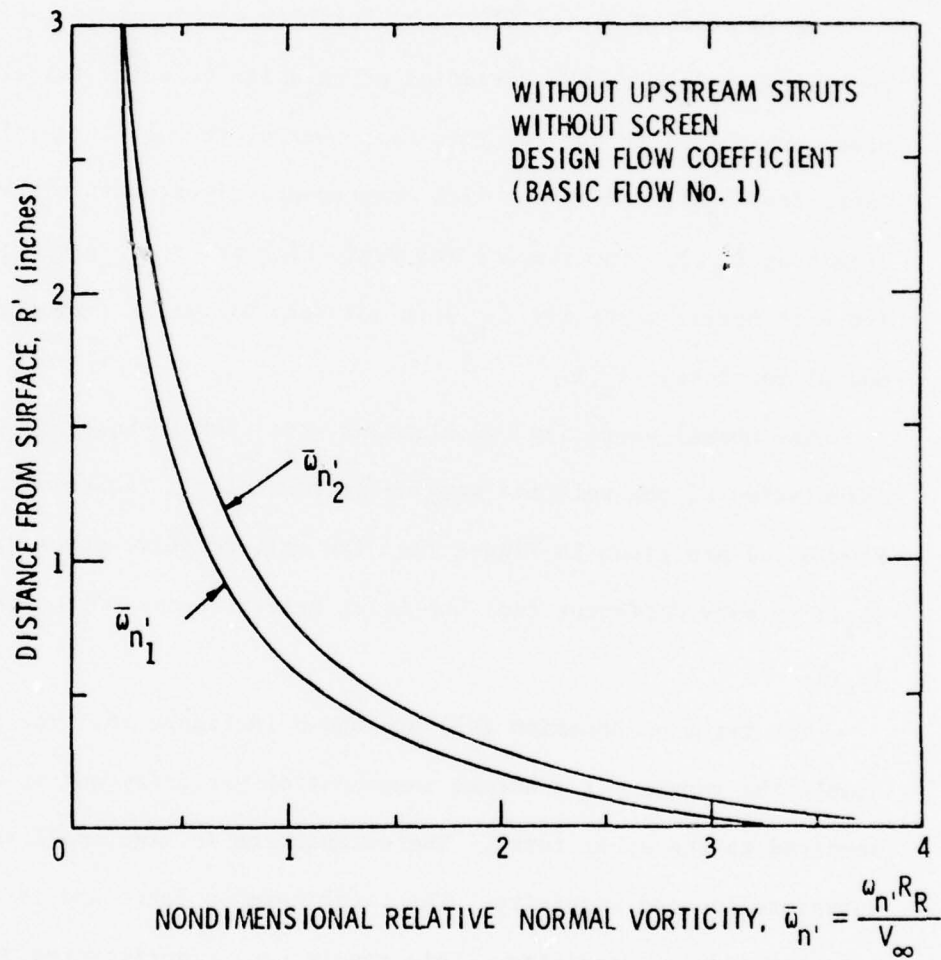


Figure 74. Relative Normal Component of Vorticity for Basic Flow No. 1

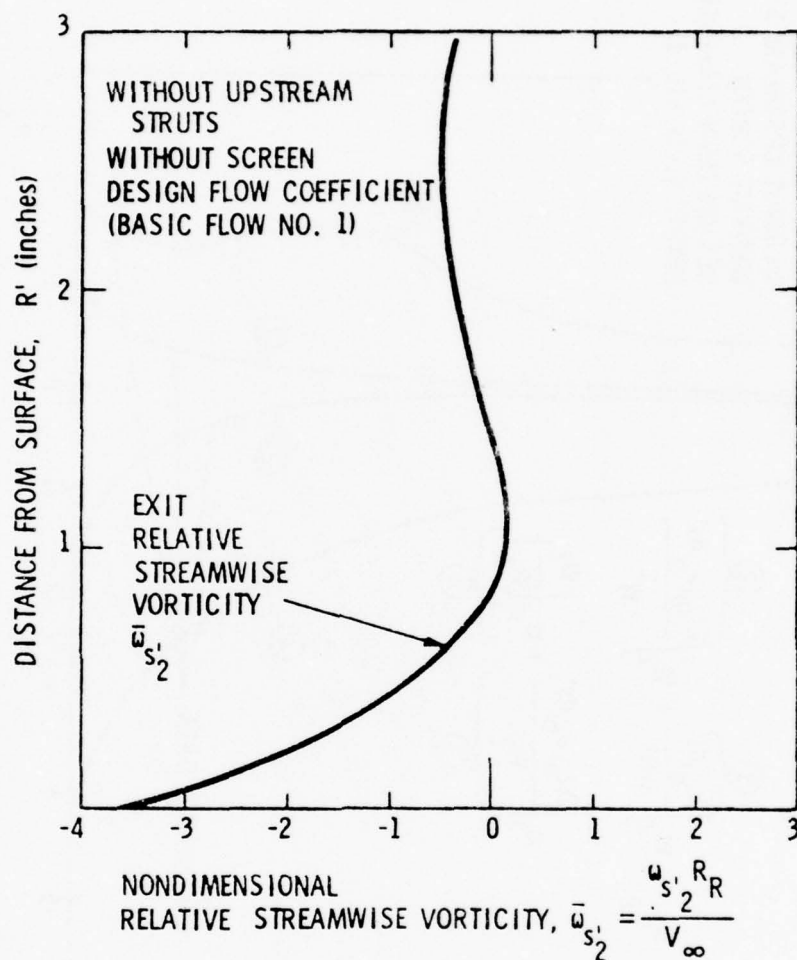


Figure 75. Relative Streamwise Component of Vorticity for Basic Flow No. 1

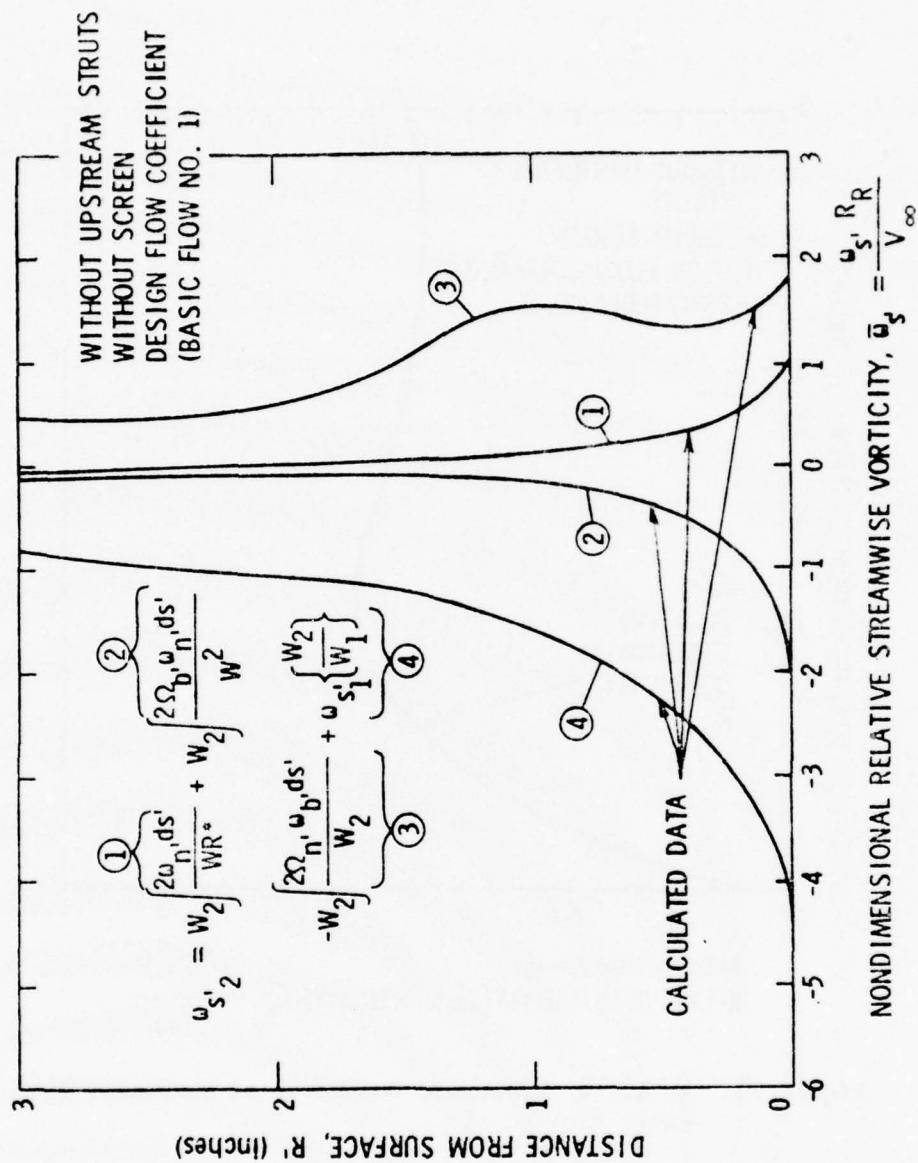


Figure 76. Components of the Relative Streamwise Vorticity for Basic Flow No. 1

of the deviation angle ($\Delta\delta_s$) due to secondary flows. The vorticity results are shown in Figure 77 for Basic Flow No. 1. The normal secondary vorticity ($\omega_{n,2}, -\omega_{n,1}$) is very small and is neglected. This result has been shown by many secondary flow investigations. The streamwise secondary vorticity is large and positive. This positive vorticity causes an overturning of the flow near the inner wall for this rotor. The vorticity is concentrated near the inner wall which correlates with the large deviation angles calculated near the inner wall and the very small deviation angles calculated over the remainder of the blade span.

The most interesting result from the calculation of the streamwise vorticity is the shape of the exit vorticity curve ($\omega_{s,2}$) shown in Figure 75. There is a large amount of negative vorticity near the inner wall and very little vorticity in the mid-radius region of the rotor.

5.2.2 Calculation of Vortex Parameters. The passage streamwise vorticity (Step 7B) was calculated from Basic Flow Nos. 1, 2, 3, and 4. The shapes of the curves ($\omega_{s,2}$) were all similar except that the region of negative vorticity near the inner wall was different in size and magnitude.

This vorticity near the inner wall can coalesce in the blade passage to form a vortex-type flow as shown by Reference [57]. In this case, the vorticity downstream of the rotor will be nonaxisymmetric. However, the vorticity can also remain distributed in the passage to form downstream a vortex with axisymmetric vorticity. In either case, there will be a characteristic length (L_c) and circulation (Γ) associated with the passage vorticity which controls the minimum pressure of the resulting vortex system. The vorticity will still induce a tangential velocity distribution similar to that measured on the rotor cap. However, large

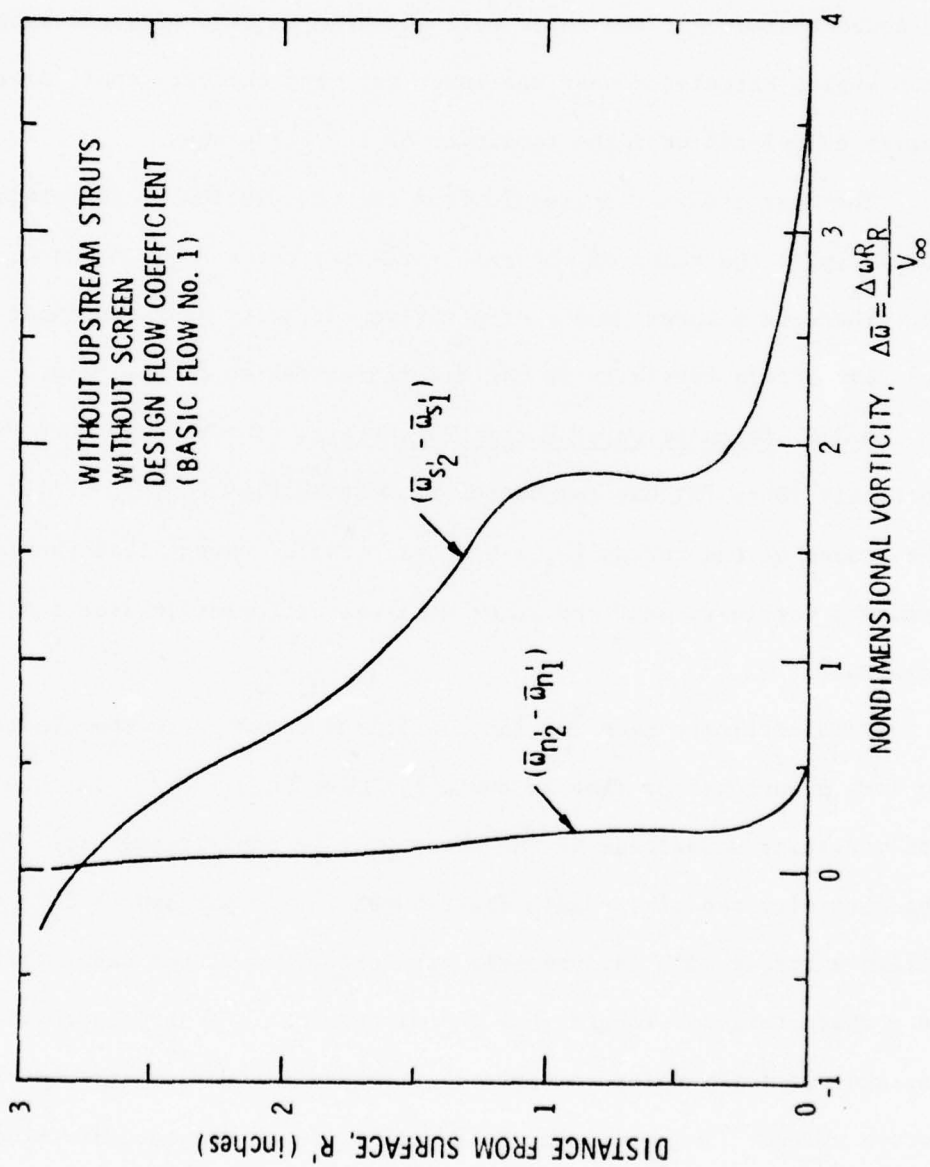


Figure 77. Secondary Passage Vorticity for Basic Flow No. 1

fluctuations in the tangential velocity would be expected if the vorticity remains nonaxisymmetric.

As can be seen in Figure 75, the streamwise vorticity ($\omega_{s,2}$) near the inner wall has a characteristic length (L_c) associated with it. This length is defined as the difference between the radius where the vorticity changes sign and the inner wall radius.

A measure of the circulation associated with this vorticity was found by integrating the vorticity (Step 7E) from the inner wall to the radius where the vorticity changes sign. The equation is

$$\Gamma = 2\pi \int_{R_i}^{R_i+L_c} \omega_{s,2} \cos\beta_2^* r dr, \quad (70)$$

where $r \cos\beta_2^*$ is normal to the vorticity. The calculated circulation is per blade passage.

The vortex parameters (Step 7E) for the four basic flow configurations are given in Table 11. Also, the nondimensional ratio ($\Gamma/L_c V_{c\omega}$) which is a measure of the minimum pressure coefficient of a Rankine vortex is given. In addition, the planar momentum thickness of the mean velocity profile entering the rotor is given as an indication of the velocity deficit.

5.3 Correlation of Vortex Parameters with Cavitation Data

Because of the uncertainty of the final vortex structure at the end of the rotor cap, an absolute calculation of $C_{p_{min}}$ in this region would be very difficult. However, the vorticity calculated in the blade passage eventually organizes the low momentum fluid near the inner wall into the final vortex structure. In addition, the vortex exists near the inner

TABLE 11
VORTEX CIRCULATION AND CORE SIZE CALCULATED FLOW VORTICITY DATA

Basic Flows	Circulation Γ (in ² /sec)	Characteristic Length L_c (inch)	Nondimensional Ratio ($\Gamma/L_c V_\infty$)	Planar Momentum Thickness θ (inch)
Basic Flow No. 1				
without upstream struts	-11.64	0.81	-0.080	0.85
without screen				
design flow coefficient				
Basic Flow No. 2				
without upstream struts	- 8.23	0.57	-0.091	0.71
without screen				
0.9 design flow coefficient				
Basic Flow No. 3				
without upstream struts	-10.99	0.83	-0.076	0.94
with screen				
design flow coefficient				
Basic Flow No. 4				
with upstream struts	- 8.29	0.45	-0.102	1.01
without screen				
design flow coefficient				

wall where the pressure in this region is not only controlled by the local vortex but also by the rotor velocity field outside of the vortex.

The vorticity does, however, dominate the flow field near the inner wall when a rotor is designed to be unloaded in this region. In this case, changes in this vorticity will directly influence the resulting minimum pressure of the vortex. Therefore, Equation (10) can be written as

$$\frac{C_{p_{\min A}}}{C_{p_{\min B}}} = \left\{ \frac{\left(\frac{\Gamma}{L_c V_\infty} \right)_A}{\left(\frac{\Gamma}{L_c V_\infty} \right)_B} \right\}^2, \quad (71)$$

where Γ and L_c are the characteristic vortex parameters of the passage streamwise vorticity. The letters A and B refer to flow states. Also, it is assumed that

$$R_c \propto L_c \quad (72)$$

In order to relate the $C_{p_{\min}}$ of the vortex to the cavitation number, several criteria must apply. First of all, the cavitation data must be free of gas effects as discussed in Section 3.4.3. This is to insure that

$$\sigma_d \approx -C_{p_{\min}} \quad (20)$$

Secondly, the minimum pressure in the final vortex structure must be controlled by the streamwise vorticity associated with the vortex and not by the pressure drop in the radial plane created by the primary flow

outside of the vortex. Also, variations in inlet velocity gradient must be small enough not to significantly affect the mean rotor loading. All of these criteria seem very restrictive; however, performance of most rotors operating within a velocity gradient meets these requirements.

A correlation between calculated minimum pressure coefficients and cavitation data can be made using Equation (71) given a reference point and knowing the effect of Reynolds number on the passage vorticity. A reference point for Basic Flow No. 1 of $\sigma = 2.8$ at a velocity of 15 ft/sec was chosen. The influence of Reynolds number on the passage vorticity ($\omega_{s,2}$) had to be solved.

As noted in Table 1, Basic Flow Nos. 14, 15, 16, and 17 are special theoretical cases which were used in the calculation of Reynolds number effects on the passage vorticity ($\omega_{s,2}$). For Basic Flow No. 14, the calculation procedure given in Figure 50 was followed. A measured velocity profile in the rotor plane without the rotor obtained at a Reynolds number of 3×10^5 was used in Step 2 of the calculation. For Basic Flow No. 15, the calculation procedure was again followed, but using a measured velocity profile in the rotor plane without the rotor obtained at a Reynolds number of 8.8×10^5 in Step 2. The two velocity profiles are shown in Figure 78.

One point should be made of these additional calculations. The normal component of absolute vorticity (ω_n) used in the vorticity calculations for Basic Flow Nos. 14 and 15 was obtained by taking the derivative of the theoretical inlet velocity profile from Step 6. As can be noted in Figure 59, the measured inlet velocity profile does not always agree with the theoretical calculations. Therefore, Basic Flow No. 1 is different from Basic Flow No. 14 because the normal vorticity for Basic Flow No. 1

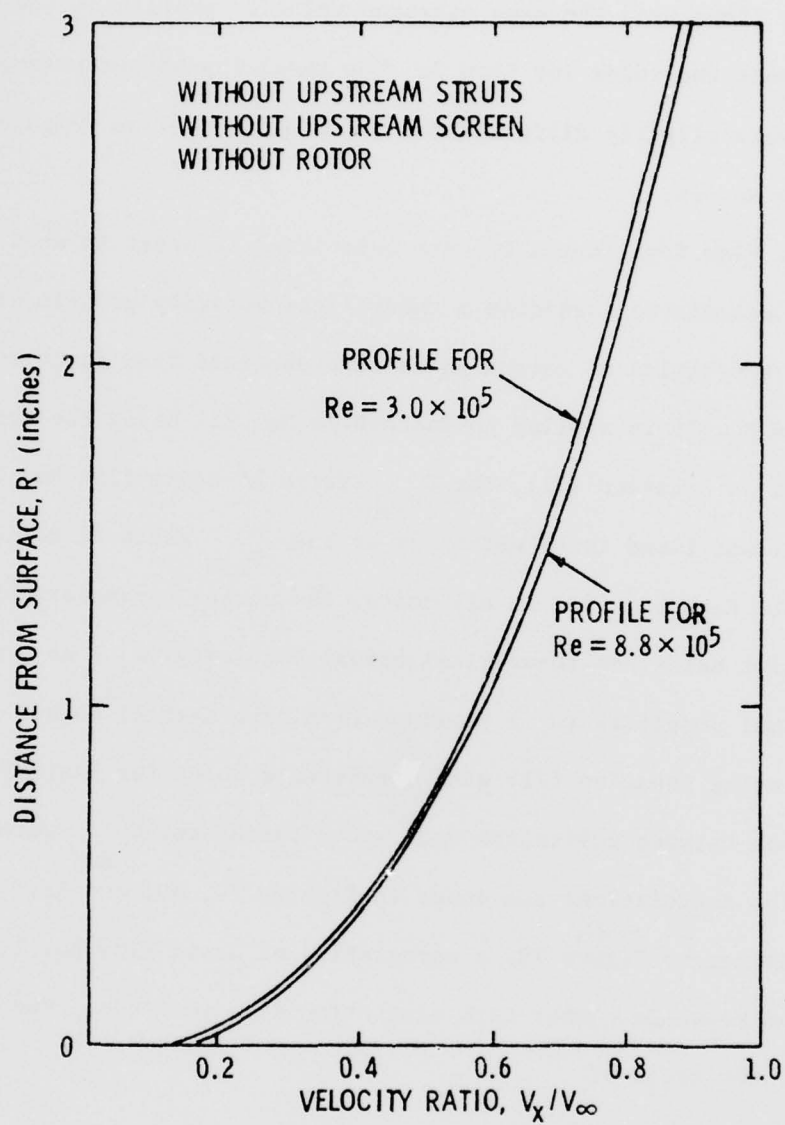


Figure 78. Axial Velocity Profiles for Different Reynolds Numbers

was obtained from a measured velocity profile in front of the rotor. Both basic flows used the same measured velocity profile in the rotor plane without the rotor for Step 2. The resulting vortex parameters of Γ and L_c were slightly different for Basic Flow No. 1 as compared to Basic Flow No. 14.

Basic Flow Nos. 16 and 17 were calculated in order to show that the vorticity calculation based on a theoretical velocity profile will not influence the ratios of vortex parameters obtained from Equation (71). Basic Flow No. 16 is similar to Basic Flow No. 2. Using the vortex parameters in Equation (71), the $C_{p_{min}}$ ratio of Basic Flow No. 2 to Basic Flow No. 1 was found to be within 2% of the $C_{p_{min}}$ ratio of Basic Flow No. 16 to Basic Flow No. 14. In all cases, the vortex parameters of Γ and L_c were smaller using the theoretical normal vorticity (ω_{n1}) as compared to using normal vorticity (ω_{n1}) obtained from experimental data.

Now using Equation (71) with a reference point for Basic Flow No. 1, comparisons between cavitation data and a calculated $C_{p_{min}}$ were made. Some of the correlations are shown in Figures 79, 80, and 81.

Referring to Figure 79, a correlation of Basic Flow No. 1, Basic Flow No. 4, and Reynolds number with cavitation data is given. For this correlation, the ratio of

$$\frac{C_{p_{min\#15}}}{C_{p_{min\#14}}} = 1.30 \quad (73)$$

was used to calculate a point of $\sigma = 3.64$ for a velocity of 45 ft/sec. A line was drawn between these two points for the correlation of data obtained for Basic Flow No. 1. The ratio of

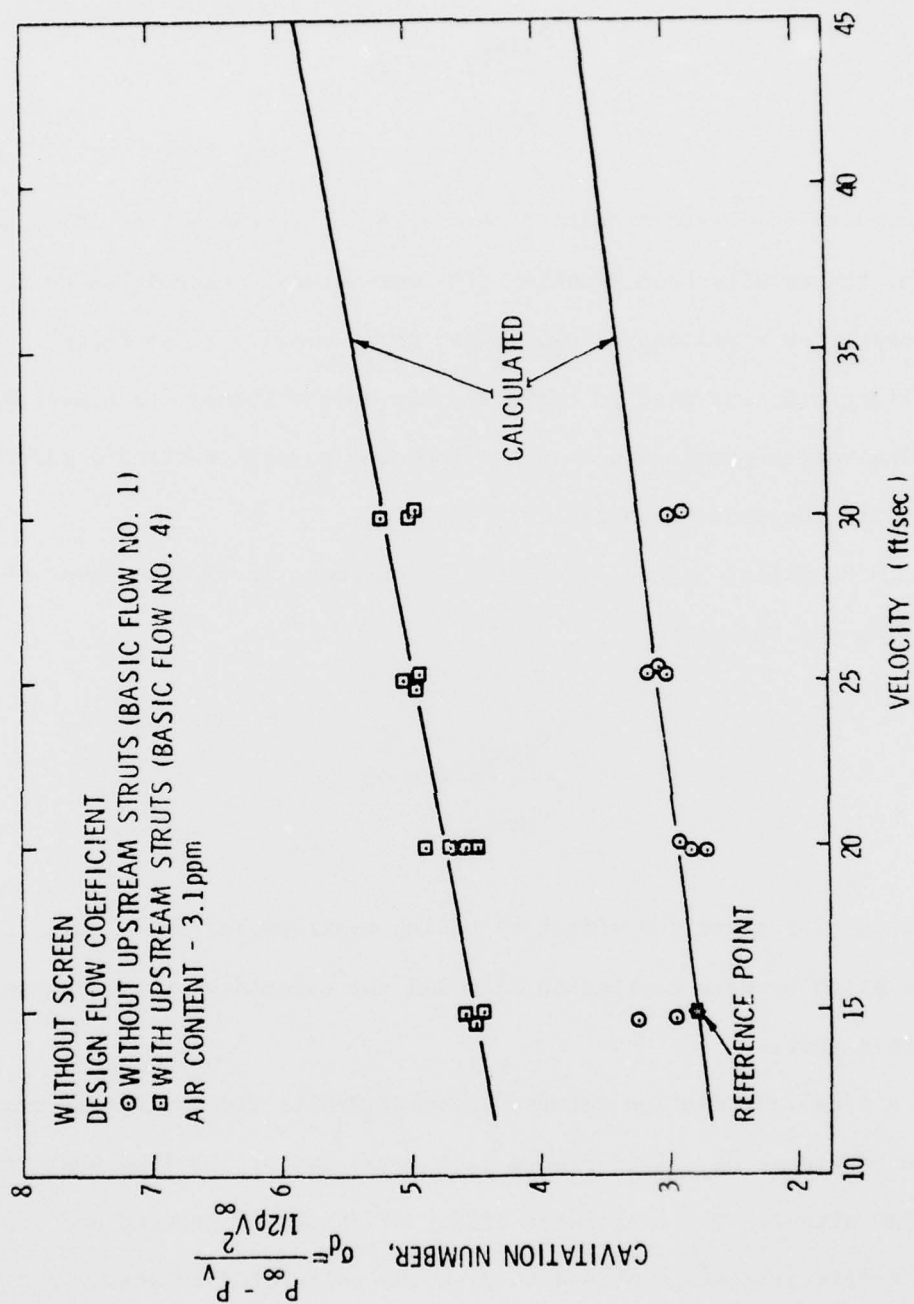


Figure 79. Correlation with Cavitation Data for Basic Flow Nos. 1 and 4

$$\frac{C_{P_{\min\#4}}}{C_{P_{\min\#1}}} = 1.62 \quad (74)$$

was used to calculate a point of $\sigma = 4.54$ for a velocity of 15 ft/sec. Again, the results from Equation (73) were used to extend the point calculated at a velocity of 15 ft/sec to a velocity of 45 ft/sec. The resulting line was used to correlate the data obtained for Basic Flow No. 4. The vortex parameters obtained from the passage vorticity correlate well with the cavitation data.

In a similar manner, the correlation shown in Figure 80 was obtained by using the ratio of

$$\frac{C_{P_{\min\#1}}}{C_{P_{\min\#3}}} = 0.90 \quad (75)$$

Equation (75) gives the effect of adding upstream screen. Again, the correlation between cavitation data and the calculated vortex parameters is quite good.

A final correlation between calculated data and cavitation data is shown in Figure 81. This figure is a composite of the four basic flow configurations. The calculated effect of struts, a screen, and off-design flow coefficient was combined to give the calculated curves. Good agreement was found except for the effect of off-design flow coefficient.

As can be seen in Figures 42, 45, and 46, the cavitation data shows a rapid change in cavitation number with velocity for off-design flow

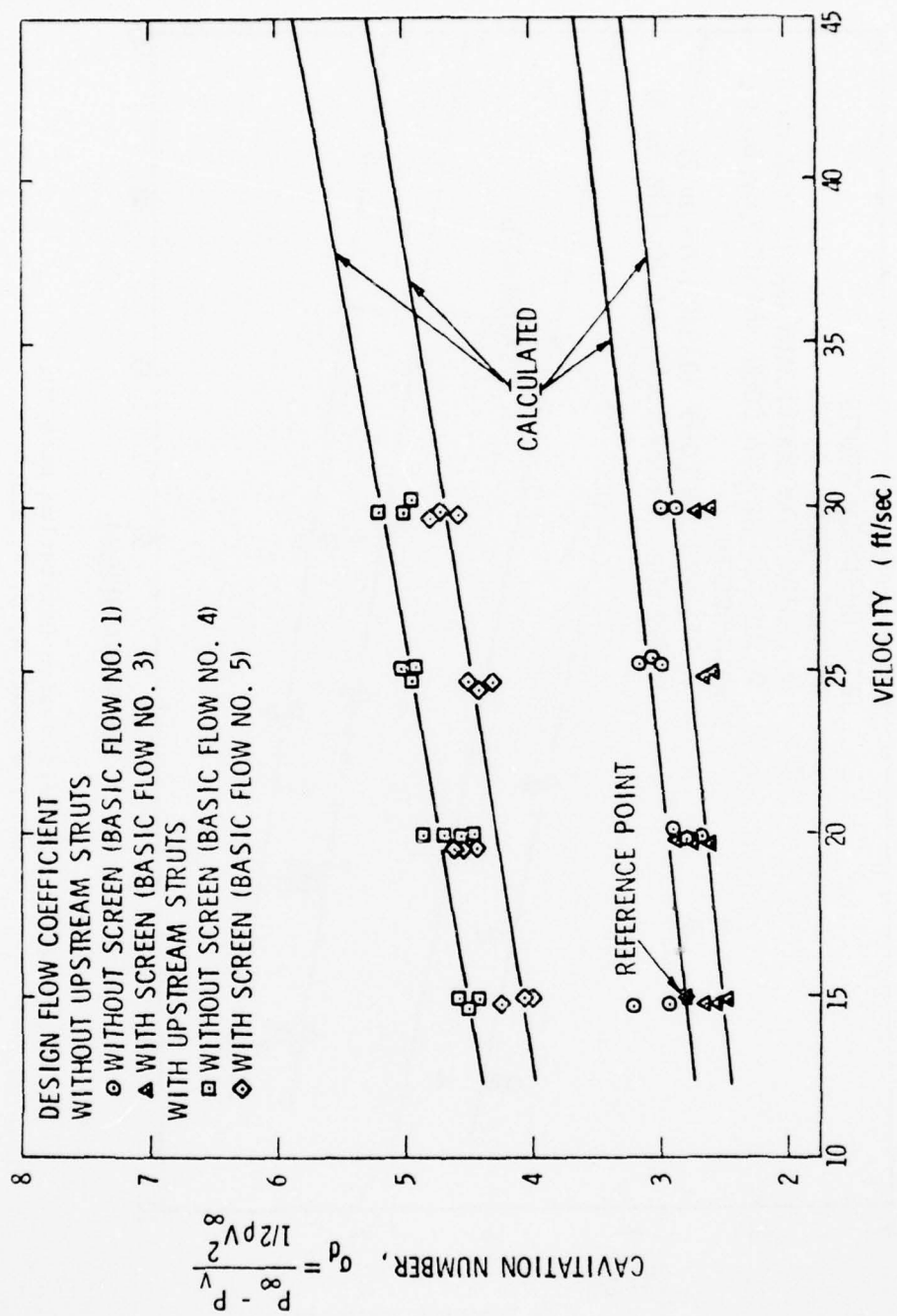


Figure 80. Correlation with Cavitation Data for Basic Flow Nos. 1, 3, 4, and 5

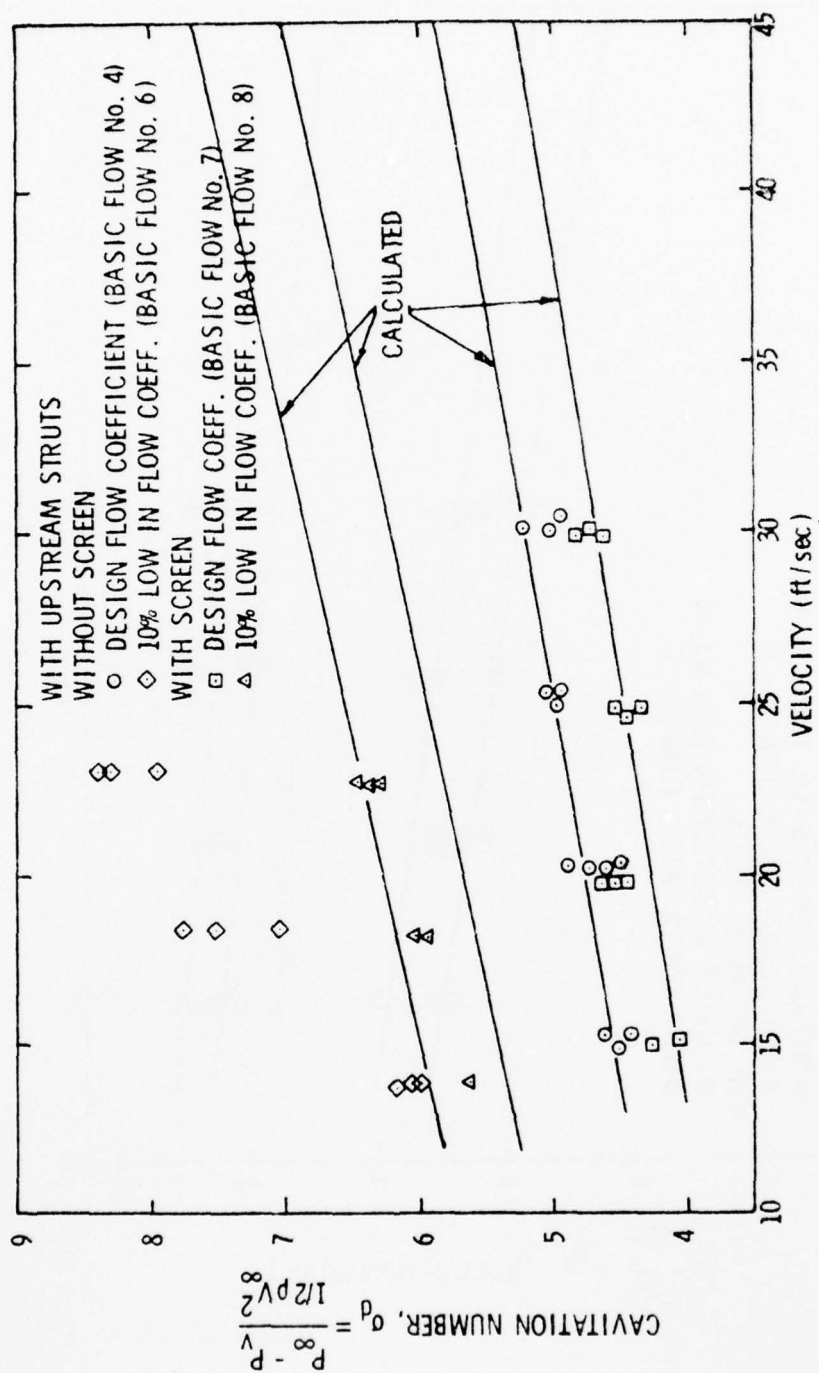


Figure 81. Correlation with Cavitation Data for Basic Flow Nos. 4, 6, 7, and 8

coefficient. Secondary flow theory alone cannot account for this trend. Therefore, these trends must include some additional primary flow effects.

A comparison can be now made between the vortex parameters (Γ , R_c) obtained from flow measurements at the end of the rotor cap and the vortex parameters calculated from the passage exit vorticity. As shown in Figure 30, solid curves can be drawn through the tangential velocity distribution (V_θ/V_ω) outside of the viscous region and inside the viscous region. The intercept of these two solid curves is the approximate radius of the vortex cone. The circulation associated with this core region is

$$\Gamma = \pi R_c V_c \quad , \quad (76)$$

where V_c is the tangential velocity at the intercept of the two curves. The resulting vortex parameters (Γ , R_c) are given in Table 12.

Also shown in Table 12 are two sets of vortex parameters (Γ , L_c) calculated from the exit passage vorticity. The first set given in Column 2 is the parameters obtained from the ω_{s2} calculations which were used in the correlation of cavitation data. The second set given in Column 3 was obtained by integrating the axial passage vorticity given as

$$\omega_x = \omega_{s2} \cos \beta_2^* + \omega_{n2} \sin \beta_2^* \quad (77)$$

over the characteristic length (L_c) defined from the ω_{s2} calculations.

A comparison shows a good correlation between the parameters estimated from the data and the parameters calculated in Column 3. In particular, the axial circulation in the measured core region appears to be the circulation obtained within the characteristic length (L_c) defined at

the rotor exit plane. In addition, the core of the vortex measured at the end of the cap is approximately one-half of the characteristic length (L_c).

TABLE 12
COMPARISON OF VORTEX PARAMETERS AT END OF CONE

Basic Flow	Estimated Vortex Parameters From Figures 28 to 31		Passage Exit Vorticity (ω_s) ₂		Absolute Vorticity (ω_s) ₂ Parameters	
	Γ_x (in ² /sec)	R_c (inch)	Γ (in ² /sec)	L_c (inch)	Γ_x (in ² /sec)	L_c (inch)
Basic Flow No. 1	19.8	0.43	-11.6	0.81	19.6	0.81
Basic Flow No. 2	17.3	0.31	- 8.2	0.57	18.3	0.57
Basic Flow No. 3	19.3	0.45	-11.0	0.80	19.3	0.80
Basic Flow No. 4	10.3	0.25	- 8.3	0.45	8.5	0.45

6. SUMMARY AND CONCLUSIONS

The critical cavitation number of a vortex formed along the inner wall of a rotor operating within a boundary layer has been correlated with the streamwise vorticity calculated in the blade passage. A method has been outlined which can be used to calculate the passage streamwise vorticity for a lightly loaded rotor having a low hub-to-tip ratio. The method involves a solution to the secondary flow equations along a mean streamline in the rotor passage. The streamlines were estimated using streamline curvature method to solve the equations of motion in the direct turbomachinery problem.

An outline of the method used to calculate the flow field including the secondary flow calculations is given in Figure 50. The flow field calculation (Step 6) using the streamline curvature method gives the data necessary for the calculation of the secondary flows. In particular, these data include the inlet velocity profile, the outlet velocity profile, and the streamline positions. The normal component of absolute vorticity (ω_n) is calculated from the inlet velocity profile using Equation (16). These data are in an absolute coordinate system.

The secondary flow calculations are outlined in more detail in Figure 73. A summary of the equations used in the secondary flow calculations is as follows:

- (1) The initial flow field data are changed into a rotating coordinate system. Now, the relative velocity (W) and

the streamline angle relative to the axial direction (β) are known at any position along the relative streamline.

- (2) As shown in Figure 54, the initial relative components of absolute vorticity (ω_{s1}, ω_{n1}) are calculated. In addition, the relative components of the absolute rotation ($\Omega_{s1}, \Omega_{n1}, \Omega_{b1}$) are calculated along the relative streamlines, the radius of curvature of the relative streamline (R^*) is calculated along the relative streamlines using Equation (43), and the relative bi-normal component of absolute vorticity (ω_{b1}) is calculated along a relative streamline using Equation (44).
- (3) The relative normal component of absolute vorticity (ω_{n1}) is calculated along each relative streamline using Equation (37).
- (4) The relative streamwise component of absolute vorticity (ω_{s1}) is calculated along each relative streamline using Equation (41). The secondary vorticity at the rotor exit plane for each streamline is $\omega_{s2} - \omega_{s1}$.
- (5) The boundary conditions for the secondary stream function defined by Equation (55) are calculated. First, the secondary velocity perturbation in the axial direction (w) is calculated using Equations (47) and (48). Secondly, the right-hand side of Equation (55) is calculated.

- (6) A series solution for the secondary stream function is obtained for Equation (59) after the calculation of $\psi_n(z)$ given by Equation (60).
- (7) The secondary velocity perturbation in the tangential direction (v) is calculated using Equation (49) and Equation (63).
- (8) The deviation angle due to the secondary vorticity ($\Delta\delta_s$) is calculated using Equation (65).

The results of the secondary flow calculations showed that the exit streamwise component of vorticity (ω_{s2}) for the rotor depended upon rotation induced secondary vorticity. In addition, the direction of the passage secondary vorticity ($\omega_{s2}, -\omega_{s1}$) was opposite to that of the exit streamwise vorticity (ω_{s2}). The passage secondary vorticity for the rotor caused an overturning of the flow near the inner wall.

Extensive experimental data were obtained not only to verify the calculation procedure but also to help in the analysis of the flow field. Some conclusions can be made from the experimental data about the flow field near the rotor and the vortex structure.

For the flow field, these are:

- (1) As the inlet velocity profile near the inner wall was increased, the cavitation number also increased.
- (2) The momentum thickness of the inlet velocity profile does not directly correlate with the core size of the vortex.
- (3) Changes of less than 12% in inlet velocity profile near the inner wall caused changes as much as 61% in cavitation number of the vortex.

- (4) Tangential velocity measurements at the rotor cap show a vortex within a constant tangential velocity field due to the rotor.

The conclusions related to the vortex structure are:

- (1) The maximum tangential velocity measured at the vortex core radius does not correlate with critical cavitation data of the vortex assuming that all of the vorticity is concentrated in the vortex core.
- (2) The minimum pressure of the vortex system does not occur on the surface of the rotor cap above a critical Reynolds number.
- (3) Changes of inlet velocity profile of less than 12% cause the vortex core radius to change by as much as 42%.
- (4) The vortex core size was found to be inversely proportional to the cavitation number of the vortex.

Additional conclusions can be made about secondary flow generated vortex cavitation from comparisons of flow field calculations with flow field measurements. These are:

- (1) The vortex parameters obtained from the calculated exit streamwise vorticity profile do correlate well with critical cavitation data.
- (2) Even though the theory was inviscid, the correlations between the calculated final flow field and measurements are quite good, including those obtained at the rotor cap.
- (3) The critical cavitation number of the vortex increased with the addition of upstream struts, with increasing

Reynolds number, and with a 10% reduction in coefficient below the design value.

- (4) The critical cavitation number of the vortex decreased with the addition of a screen and with a 10% increase in flow coefficient above the design value.
- (5) The effects of Reynolds number, struts, screens, and off-design flow coefficients can be combined to successfully correlate cavitation data for any basic flow considered.
- (6) The secondary flow theory with its many assumptions gives a good prediction of the tangential velocity profile near the inner wall.

No single calculation or single piece of experimental data can explain the vortex structure. However, collectively, a model of the vortex system becomes apparent above a critical Reynolds number. The fact that the calculated passage vorticity and its characteristic length scale correlates the cavitation data and that the measured vortex core radius and maximum tangential velocity do not correlate the cavitation data indicates that the net circulation of the vortex is not within the vortex core. Thus, the complicated flow around the rotor cap appears to be like that of several small vortices inside of larger single vortex where viscous effects do not dominate the flow near the inner wall of the rotor. Each one of the smaller vortices is formed within each blade passage. This flow picture explains the vortex shown in Figure 1.

This investigation of secondary flow generated cavitation is only a beginning. More experimental data are needed of the secondary flow field in the rotor passage to establish the motion predicted by the theoretical

AD-A064 708

PENNSYLVANIA STATE UNIV UNIVERSITY PARK APPLIED RESE--ETC F/G 20/4
SECONDARY-FLOW-RELATED VORTEX CAVITATION.(U)

JUL 78 M L BILLET

ARL/PSU/TM-78-189

N00024-79-C-6043

NL

UNCLASSIFIED

30F 3
AD
A064708



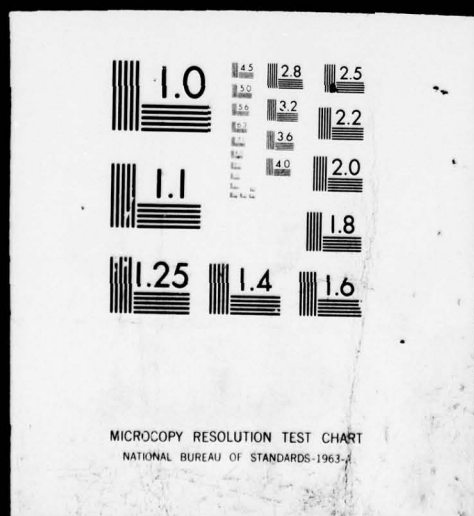
END
DATE
FILMED

4 --79
DDC

IFIED

30F 3

AD
A064708



development. In addition, the vorticity roll-up phenomenon must be investigated in order to predict the true vortex core size before an absolute calculation of $C_{p_{min}}$ can be made. Future plans are to incorporate the secondary flow theory into the design of a rotor in order to obtain a vortex of specified critical cavitation index.

REFERENCES

1. Consultations with W. S. Gearhart at the Applied Research Laboratory, The Pennsylvania State University, May 1970.
2. McCormick, B. W., "A Study of the Minimum Pressure in a Trailing Vortex System," Ph.D. Thesis, Dept. of Aerospace Engineering, The Pennsylvania State University, June 1954.
3. Hashimoto, H., "Progressive Waves on Swirling Cavity Flow in a Circular Pipe," J. of Basic Engineering, Trans. ASME, December 1969, pp. 714-721.
4. Hall, M. G., "A Numerical Method for Solving the Equations for a Vortex Core," Aero. Res. Council, R&M 3467, 1965.
5. Gartshore, I. S., "Recent Work in Swirling Incompressible Flow," NRC Can. Aero., Report LR-343, 1962.
6. Bossel, H. H., "Inviscid and Viscous Models of the Vortex Breakdown Phenomenon," Report No. AS-67-14, University of California, Berkeley, 1967.
7. Sarpkaya, T., "On Stationary and Traveling Vortex Breakdowns," J. Fluid Mechanics, Vol. 43, 543, 1971.
8. Harvey, J. K., "Some Observations of the Vortex Breakdown Phenomenon," J. Fluid Mechanics, Vol. 14, 585, 1962.
9. Kirkpatrick, D. L. I., "Experimental Investigation of the Breakdown of a Vortex in a Tube," R. E. A. Tech. Note No. 2963, 1964.
10. Peckham, D. H., and S. R. Atkinson, "Preliminary Results of Low Speed Wind Tunnel Tests on a Gothic Wing of Aspect Ratio 1.0," T.N. Aero. No. 2504, 1957.
11. McCormick, B. W., "On Cavitation Produced by a Vortex Trailing from a Lifting Surface," J. Basic Engineering, Trans. ASME, September 1962, pp. 369-379.
12. Hall, M. G., "Vortex Breakdown," Annual Review of Fluid Mechanics, Vol. 4, 1972, pp. 195-218.
13. Hawthorne, W. R., "Secondary Circulation in Fluid Flow," Proceedings of the Royal Society, London, England, Series A, Vol. 206, May 1951, p. 374.
14. Staff of Lewis Research Center, "Aerodynamic Design of Axial-Flow Compressors," NASA SP-36, 1965.

15. Smith, L. H., "Secondary Flow in Axial-Flow Turbomachinery," Trans. ASME, Vol. 77, 1955.
16. Lakshminarayana, B., and J. H. Horlock, "Generalized Expressions for Secondary Vorticity Using Intrinsic Coordinates," J. Fluid Mechanics, Vol. 59, 1973, pp. 97-115.
17. Horlock, J. H., Discussion of "Secondary Vorticity in Axial Compressor Blade Rows," by S. L. Dixon, NASA SP-304, 1970.
18. Lakshminarayana, B., and J. H. Horlock, "Review: Secondary Flows and Losses in Cascades and Axial Turbomachines," Int. J. Mech. Sci., Vol. 5, 1963, p. 287.
19. Hawthorne, W. R., and R. A. Novak, "The Aerodynamics of Turbomachinery," Ann. Rev. Fluid Mechanics, Vol. 1, 1969.
20. Salvage, J. W., "A Review of the Current Concept of Cascade Secondary Flow Effects," Von Karman Institute, TM 95, 1974.
21. Holl, J. W., "Limited Cavitation," Proceedings of the Symposium on Cavitation State of Knowledge, ASME, June 1969, pp. 26-63.
22. Holl, J. W., R. E. A. Arndt, and M. L. Billet, "Limited Cavitation and the Related Scale Effects Problem," Proc. Second Int. JSME Symposium on Fluid Machinery and Fluidics, Tokyo, September 1972, pp. 303-314.
23. Holl, J. W., "An Effect of Air Content on the Occurrence of Cavitation," J. of Basic Engineering, Trans. ASME, Series D, Vol. 82, 1960, pp. 941-946.
24. Holl, J. W., and A. L. Treaster, "Cavitation Hysteresis," J. of Basic Engineering, Trans. ASME, Series D, March 1966, pp. 199-212.
25. Hammitt, F. G., J. F. Lafferty, D. M. Ericson, and M. J. Robinson, "Gas Content, Size, Temperature and Velocity Effects on Cavitation Inception in a Venturi," ASME Paper 67 WA/FE22, 1967.
26. Lindgren, H., and C. A. Johnson, "Cavitation Inception on Head Forms -- ITTC Comparative Experiments," Report No. 58, Swedish State Shipbuilding Experimental Tank, 1966.
27. Ripken, J. F., and J. M. Killen, "Gas Bubbles: Their Occurrence, Measurements and Influence in Cavitation Testing," Proceedings of IAHR Symposium, Sendai, Japan, 1962, pp. 37-57.
28. Lehman, A. F., "The Garfield Thomas Water Tunnel," ORL Report, Serial No. NORD 16597-56, September 30, 1959.
29. Billet, M. L., "Rotor Incoming Velocity Profile Measurements," Applied Research Laboratory, Technical Memorandum No. 76-254, 11 October 1976.

30. Patel, V. C., "A Simple Integral Method for the Calculation of Thick Axisymmetric Turbulent Boundary Layers," Aeronautical Quarterly, Vol. 25, February 1974.
31. Treaster, A. L., "The Calibration of Six Probes for Sensing Three-Dimensional Fluid Flow Properties," Applied Research Laboratory, Technical Memorandum No. 74-282, October 8, 1974.
32. Billet, M. L., "Flow Measurements Behind a Rotor Operating in a Boundary Layer, Applied Research Laboratory, Technical Memorandum No. 76-260, 12 October 1976.
33. Billet, M. L., "Cavitation Results for a Secondary Flow Generated Trailing Vortex," Applied Research Laboratory, Technical Memorandum No. 76-234, 24 August 1976.
34. Novak, R. A., "Streamline Curvature Computing Procedures," J. of Engineering for Power, Trans. ASME, Series A, Vol. 89, No. 4, October 1967, pp. 478-490.
35. Frost, D. H., "A Streamline Curvature Through-Flow Computer Program for Analyzing the Flow Through Axial Flow Turbomachines," ARC R&M No. 3687, August 1970.
36. Davis, W. R., "A Computer Program for the Analysis and Design of Turbomachinery -- Revision," Carleton University, Report No. ME/A 71-5.
37. McBride, M. W., "A Streamline Curvature Method of Analyzing Axisymmetric Axial, Mixed and Radial Flow Turbomachinery," Applied Research Laboratory, Technical Memorandum No. 77-219, July 21, 1977.
38. Horlock, J. H., Axial Flow Compressors, R. E. Krieger Company, New York, 1973, pp. 55-60.
39. Lakshminarayana, B., Discussion of Wilson, Mani, and Acosta's, "A Note on the Influence of Axial Velocity Ratios on Cascade Performance," NASA SP-304, Part 1, 1974, pp. 127-133.
40. Lieblein, S., "Experimental Flow in Two-Dimensional Cascades," NASA SP-36, 1965, pp. 209-222.
41. Horlock, J. H., Cambridge University Report, CUED/A-Turbo/TR28, 1971.
42. Hawthorne, W. R., "Rotational Flow Through Cascades: Part 1, The Components of Vorticity," Quart. J. Mech. Appl. Math., Vol. 8, Part 3, 1955.
43. Came, P. M., and H. March, "Secondary Flow in Cascades: Two Simple Derivations for the Component of Vorticity," Int. J. Mech. Sci., Vol. 16, No. 6, December 1970.
44. Greenspan, H. P., The Theory of Rotating Fluids, Cambridge University Press, 1968.

45. Billet, M. L., "Secondary Flow Vorticity in the Passage of a Rotor," Applied Research Laboratory, Technical Memorandum File No. 77-243, August 17, 1977.
46. Lakshminarayana, B., and J. H. Horlock, "Effect of Shear Flows on the Outlet Angle in Axial Compressor Cascades -- Methods of Prediction and Correlation with Experiments," J. Basic Engineering, Vol. 89, 1967, p. 191.
47. Squire, H. B., and K. G. Winter, "The Secondary Flow in a Cascade of Airfoils in a Nonuniform Stream," J. Aeronaut. Sci., Vol. 18, 1951, p. 271.
48. Hawthorne, W. R., and W. D. Armstrong, "Shear Flow Through a Cascade," Aeronautical Quarterly, Vol. 7, 1956, p. 247.
49. Hawthorne, W. R., "Some Formulae for the Calculation of Secondary Flow in Cascades," British Aeron. Res. Council, Report 17519, 1955.
50. Dixon, S. L., "Secondary Vorticity in Axial Compressor Blade Rows," NASA SP-304, Part 1, 1974, pp. 173-204.
51. Hawthorne, W. R., "Flow in Bent Pipes," Proc. Seminar Aero. Sci., Bangalore, India, 1961, pp. 305-333.
52. Eichenberger, H., "Secondary Flow Within a Bend," J. Math. and Phys., Vol. 32, 1953, p. 34.
53. Detra, R. W., "The Secondary Flow in Curved Pipes," ETH Inst. Aerodyn. (Zurich), Report No. 20, 1953.
54. Hawthorne, W. R., Discussion of Dixon, "Secondary Vorticity in Axial Compressor Blade Rows," NASA SP-304, Part 1, 1974, p. 192.
55. Billet, M. L., "An Approximate Method for the Solution of the Direct Problem of an Open Rotor," Applied Research Laboratory, Technical Memorandum File No. 78-161, May 1978.
56. Smith, L. H., Jr., Discussion of Horlock, "Annulus Wall Boundary Layers in Axial Compressor Stages," Trans. ASME, J. Basic Engineering, Vol. 85, 1963.
57. Herzig, H. Z., A. G. Hansen, and G. R. Costello, "A Visualization Study of Secondary Flows in Cascades," NACA Report 1163, 1954.
58. Treaster, A. L., and A. M. Yocum, "The Calibration and Application of Five-Hole Probes," Applied Research Laboratory, Technical Memorandum File No. 78-10, January 18, 1978.

APPENDIX A: ANALYSIS OF EXPERIMENTAL ERROR

In the experimental part of this vortex study, many different instruments were used. The following is a summary of the measurements that were made and the instruments that were used:

48-Inch Wind Tunnel

- (1) Rotor inlet velocity profiles were calculated from pressure data obtained from separate total and static pressure probes.
- (2) Static pressure taps on the surface were used to calculate the pressure distribution on the stationary surface upstream of the rotor plane.

48-Inch Water Tunnel

- (1) Rotor outlet velocity profiles were calculated from data obtained with a 5-hole prism probe.
- (2) Static pressure taps on both the stationary surface and rotating core were used to calculate the surface pressure distribution.
- (3) Desinent cavitation numbers for the vortex were calculated from pressures obtained from a pitot-static probe located in the free-stream.
- (4) Velocity profiles were calculated at the end of the rotor cap from frequency data of a LDA.
- (5) Several rotor inlet and outlet velocity profiles were calculated from LDA data.

The determination of accuracy is difficult when, as in most cases, only one instrument was used with a limited number of samples. However,

the rotor outlet tangential velocity profiles for several cases were measured with a 5-hole prism probe and the LDA. These two instruments were used during different water tunnel test programs. The results show an experimental accuracy of 3% of the reading.

The 5-hole prism probe used in this study was calibrated in an open jet wind tunnel in an effort to reduce errors. Details of the calibration procedure are given in Reference [32]. Treaster and Yocum [58] conducted a detailed statistical analysis of their data based on a typical probability curve which indicated that the 50% error of the mean was less than 1% of the maximum value of each probe coefficient.

The inlet velocity profiles were important in the calculation procedure of the secondary flows and therefore a large number of data points were obtained. The profiles were calculated from total pressure tubes and static pressure probes positioned in front of the rotor. In all, three total pressure rakes and one static pressure rake were used. As the rakes were rotated, pressures were recorded at 2° increments for a total of 360° . The static pressure distribution through the boundary layer was established by matching the static pressure probe data to the static pressure measurements on the surface. Each inlet velocity data point was an average of 180 points. The accuracy of the measurements is determined by the accuracy of the United Sensor static pressure probe which is 1% of the reading.

Desinent cavitation numbers for the vortex were calculated from pressures obtained from a pitot-static probe. The probe was manufactured by United Sensor and the accuracy was 1% of the reading. However, there is always data scatter for cavitation data because a desinent cavitation

point is visually determined and is influenced by fluid property variations. The maximum scatter of the cavitation data is 10% of mean value.

DISTRIBUTION LIST FOR UNCLASSIFIED TM 78-189 by M. L. Billet

Commander
Naval Sea Systems Command
Department of the Navy
Washington, DC 20362
Attn: Library
Code NSEA-09G32
(Copy Nos. 1 and 2)

Naval Sea Systems Command
Attn: Code NSEA-0342
(Copy Nos. 3 and 4)

Naval Sea Systems Command
Attn: T. E. Peirce
Code NSEA-0351
(Copy No. 5)

Naval Sea Systems Command
Attn: J. G. Juergens
Code NSEA-037
(Copy No. 6)

Naval Sea Systems Command
Attn: A. R. Paladino
Code NSEA-0372
(Copy No. 7)

Commander
Naval Ship Engineering Center
Attn: F. Welling
Code NSEC-6144

Naval Ship Engineering Center
Attn: D. Burke
Code NSEC-6113C1
(Copy No. 9)

Commanding Officer
Naval Underwater Systems Center
Newport, RI 02840
Attn: Library
Code LA15
(Copy No. 10)

Commanding Officer
Naval Ocean Systems Center
San Diego, CA 92152
Attn: Library
(Copy No. 11)

Naval Ocean Systems Center
Attn: J. W. Hoyt
Code 2501
(Copy No. 12)

Commander
Naval Surface Weapon Center
Silver Spring, MD 20910
Attn: Library
(Copy No. 13)

Commanding Officer & Director
David W. Taylor Naval Ship R&D Center
Department of the Navy
Bethesda, MD 20084
Attn: W. E. Cummins
Code 15
(Copy No. 14)

David W. Taylor Naval Ship R&D Center
Attn: Tech. Info. Lib.
Code 522.1
(Copy No. 15)

David W. Taylor Naval Ship R&D Center
Attn: M. Sevik
Code 19
(Copy No. 16)

David W. Taylor Naval Ship R&D Center
Attn: W. Morgan
Code 154
(Copy No. 17)

David W. Taylor Naval Ship R&D Center
Attn: S. Crump
Code 1505
(Copy Nos. 18-32)

Dr. Ralph Cooper
Office of Naval Research
Department of the Navy
800 N. Quincy Street
Arlington, VA 22217
(Copy No. 33)

Defense Documentation Center
5010 Duke Street
Cameron Street
Alexandria, VA 22314
(Copy Nos. 34-45)

Dr. Allan J. Acosta
Prof. of Mechanical Engineering
Div. of Engineering and Applied Science
California Institute of Technology
Pasadena, CA 91125
(Copy No. 46)

DISTRIBUTION LIST FOR UNCLASSIFIED TM 78-189 by M. L. Billet

Mr. Robert Waid
Lockheed Missile & Space Company
Orgn. 57-24, Bldg. 150
Post Office Box 504
Sunnyvale, CA 94088
(Copy No. 47)

Dr. Albert T. Ellis
University of California
Department of Applied Mechanics
La Jolla, CA 92038
(Copy No. 48)

Dr. F. G. Hammitt
Professor of Mechanical Engineering
The University of Michigan
Ann Arbor, Michigan 48105
(Copy No. 49)

Iowa Institute of Hydraulic Research
State University of Iowa
Iowa City, Iowa 52240
Attn: Director
(Copy No. 50)

Prof. Edward Silberman
St. Anthony Falls Hydraulic Laboratory
Institute of Technology
University of Minnesota
Mississippi River at 3rd Avenue, S.E.
Minneapolis, Minnesota 55414
(Copy No. 51)

Dr. Roger E. A. Arndt
St. Anthony Falls Hydraulic Laboratory
University of Minnesota
Mississippi River at 3rd Avenue, S.E.
Minneapolis, Minnesota 55414
(Copy No. 52)

Dr. J. M. Robertson
125 Talbot Laboratory
University of Illinois
Urbana, Illinois 61801
(Copy No. 53)

Dr. P. Leehey
Department of Naval Architecture
Massachusetts Institute of Technology
Cambridge, Massachusetts 02139
(Copy No. 54)

Dr. B. Lakshminarayana
153-J Hammond
Department of Aerospace Engineering
The Pennsylvania State University
University Park, PA 16802
(Copy No. 55)

Department of Aerospace Engineering
Attn: Dr. W. Phillips
(Copy No. 56)

Department of Aerospace Engineering
Attn: Dr. B. W. McCormick
(Copy No. 57)

Dr. G. F. Wislicenus
351 Golf Court (Oakmont)
Santa Rosa, California 95405
(Copy No. 58)

Applied Research Laboratory
Attn: Dr. J. W. Holl
(Copy Nos. 59-60)

Applied Research Laboratory
Attn: Dr. R. E. Henderson
(Copy No. 61)

Applied Research Laboratory
Attn: Dr. E. J. Skudrzyk
(Copy No. 62)

Applied Research Laboratory
Attn: Dr. M. L. Billet
(Copy Nos. 63-64)

Applied Research Laboratory
Attn: W. S. Gearhart
(Copy No. 65)

Applied Research Laboratory
Attn: GTWT Library
(Copy No. 66)